

12 LEVEL III

AD-E000436

NRL Memorandum Report 4217

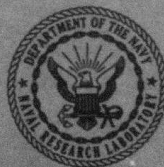
ADA086159

**DARPA-NRL Laser Program
Annual Technical Report to
Defense Advanced Research Projects Agency
1 October 1978 - 30 September 1979**

L. CHAMPAGNE, COORDINATOR

*Laser Physics Branch
Optical Sciences Division*

April 30, 1980



**NAVAL RESEARCH LABORATORY
Washington, D.C.**

Approved for public release; distribution unlimited.

DTIC
ELECTE
JUL 2 1980
S D
B

DDC FILE COPY

NRL Memorandum Report 4217

80 5 7 042

SECURITY CLASSIFICATION OF THIS PAGE (When Data Entered)

REPORT DOCUMENTATION PAGE		READ INSTRUCTIONS BEFORE COMPLETING FORM
1. REPORT NUMBER NRL Memorandum Report 4217	2. GOVT ACCESSION NO. AD-A086159	3. RECIPIENT'S CATALOG NUMBER
4. TITLE (and Subtitle) DARPA-NRL LASER PROGRAM - ANNUAL TECHNICAL REPORT TO DEFENSE ADVANCED RESEARCH PROJECTS AGENCY - 1 OCTOBER 1978 - 30 SEPTEMBER 1979		5. TYPE OF REPORT & PERIOD COVERED Annual report - 1 October 1978 - 30 September 1979
7. AUTHOR(s) L. Champagne, Coordinator		6. PERFORMING ORG. REPORT NUMBER
9. PERFORMING ORGANIZATION NAME AND ADDRESS Naval Research Laboratory Washington, D.C. 20375		8. CONTRACT OR GRANT NUMBER(s)
11. CONTROLLING OFFICE NAME AND ADDRESS Defense Advanced Research Projects Agency Arlington, VA 22209		10. PROGRAM ELEMENT, PROJECT, TASK AREA & WORK UNIT NUMBERS NRL Problem 55-1164-0-0 DARPA Order 2062; Project 9E20
14. MONITORING AGENCY NAME & ADDRESS (if different from Controlling Office)		12. REPORT DATE April 30, 1980
		13. NUMBER OF PAGES 155
		15. SECURITY CLASS. (of this report) UNCLASSIFIED
		15a. DECLASSIFICATION/DOWNGRADING SCHEDULE
16. DISTRIBUTION STATEMENT (of this Report) Approved for public release; distribution unlimited.		
17. DISTRIBUTION STATEMENT (of the abstract entered in Block 20, if different from Report)		
18. SUPPLEMENTARY NOTES		
19. KEY WORDS (Continue on reverse side if necessary and identify by block number) Lasers Electrical laser Laser diagnostics Electronic state lasers Chemical kinetics Electronic state lifetimes Energy transfer		
20. ABSTRACT (Continue on reverse side if necessary and identify by block number) The DARPA-NRL program is concerned with the development of laser technology. The basic physics of the XeCl laser have been examined theoretically and experimentally. The basic physics behind the improved performance of the XeF laser at elevated temperature is reported. The limitations of the Kr ₂ F* laser have been studied. Preliminary experiments involving two other promising visible lasers (H _g Br, XeF (C→A)) are reported.		

DD FORM 1 JAN 73 1473

EDITION OF 1 NOV 65 IS OBSOLETE
S/N 0102-014-6601

1
SECURITY CLASSIFICATION OF THIS PAGE (When Data Entered)

CONTENTS

FOREWORD	iv
SHORT PULSE KINETICS	1
Formation and Quenching Kinetics of XeCl	1
Fluorescence Parameter Study	6
XeF C State Quenching	6
LONG PULSE KINETICS	33
Kinetics of the XeCl (B→X) Laser	33
COMPUTER MODELING	48
RGH Computer Code Development for the XeCl Laser —	
Secondary Electron Kinetics	48
Kinetics Simulation of High-Power Gas Lasers	58
Depletion of the Halogen Donor in the XeF Laser	72
Appendix I	80
ELECTRON BEAM PUMPED LASERS	82
Electron Beam Pumped XeCl Laser	82
Absorption Processes in XeCl Laser	87
Transient Absorption in Electron-Beam Excited Rare	
Gases at XeF Laser Wavelengths	99
Temperature Dependent Absorption Processes in the XeF Laser	110
VISIBLE LASER STUDIES	124
Absorption by Kr ₂ F* at 358 nm	137
A Discharge Pumped Laser on the C→A Transition of XeF	149

DTIC
ELECTE
S JUL 2 1980 D
B

ACCESSION for	
NTIS	White Section <input checked="" type="checkbox"/>
DDC	Buff Section <input type="checkbox"/>
UNANNOUNCED	<input type="checkbox"/>
JUSTIFICATION	
BY	
DISTRIBUTION/AVAILABILITY CODES	
Dist.	AVAIL. and/or SPECIAL
A	

FOREWORD

The Laser Physics Branch of the Optical Sciences Division, Naval Research Laboratory, Washington, D. C., prepared this annual report on work sponsored by the Defense Advanced Research Projects Agency, DARPA Order 2062. The projects described are also funded by NRL-ONR research funds. Co-authors of the report were R. Burnham, L. F. Champagne, R. S. F. Chang, J. G. Eden, R. W. Waynant, S. K. Searles, L. J. Palumbo, T. Finn and N. Djeu.

FY 79 ANNUAL TECHNICAL REPORT

1. DARPA Order	2062
2. Program Code Number	9E20
3. Name of Contractor	Naval Research Laboratory
4. Effective Date of Contract	1 October 1978
5. Contract Expiration Date	30 September 1979
6. Amount of Contract	\$300,000
7. Contract Number	62301E
8. Principal Investigator	N. Djeu
9. Telephone Number	(202) 767-3217
10. Project Scientist	L. F. Champagne
11. Telephone Number	(202) 767-2512
12. Title of Work	DARPA/NRL Laser Technology Program

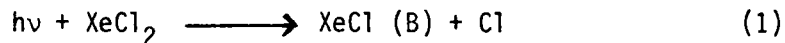
SPONSORED BY
DEFENSE ADVANCED RESEARCH PROJECTS AGENCY
DARPA Order 2062

DARPA-NRL LASER PROGRAM
Annual Technical Report to
Defense Advanced Research Projects Agency
1 October 1978 — 30 September 1979
SHORT PULSE KINETICS

Formation and Quenching Kinetics of XeCl

I. Synthesis of XeCl₂

The kinetics governing the formation of XeCl remain elusive. Even those properties such as the radiative lifetime and the quenching rate constants of the excited state, easily obtained by photolysis methods for XeF¹ and with minor difficulty with KrF,² have been unyielding for XeCl. The major reason for this difficulty with XeCl is that the dihalide, XeCl₂, is difficult to synthesize in sufficient quantity and appears to have poor stability at temperatures much above 77°K. The importance of XeCl₂ rests on the desire to photolyze it rapidly producing XeCl (B).



This method is a very straightforward approach for studying radiative lifetime and quenching. It has been used with great success with XeF,¹ KrF² and the mercury halides,³ but cannot be used for XeCl unless XeCl₂ can be synthesized. Consequently, work continues on the synthesis.

The first reports of XeCl₂ were made by Nelson and Pimentel⁴ who passed Xe:Cl₂ mixtures through a microwave discharge and condensed the gases on a cold (16°K) CsI window. Absorption bands were seen in the 313 cm⁻¹ region which corresponded with calculated absorptions for XeCl₂.

Manuscript submitted March 6, 1980.

Several additional workers⁵ obtained substantiating results. Howard and Andrews⁶ took another approach. They used an argon ion laser to photolyze matrix-isolated Cl_2 in a xenon matrix producing XeCl_2 which they studied by observation of the Raman spectra. While synthesis was possible with all of the argon-ion laser lines (501.7, 488.0, 476.5 and 457.9 nm) the best results occurred with 476.5 nm. Using this wavelength the 254 cm^{-1} band assigned to ν_1 of XeCl_2 grew intense within two minutes after laser irradiation and remained constant in intensity. The longer wavelengths took longer to form XeCl_2 and the shorter wavelengths appear to destroy the molecule after a few minutes of irradiation. It is assumed that this is due to the fact that the photodissociation limit of Cl_2 is at 478.5 nm. Longer wavelengths (501.7 and 488.0) probably have more difficulty in dissociating Cl_2 while shorter wavelengths (457.9 nm) probably impart so much energy to the Cl fragments that the molecule does not form.

Based on this existing information and on our past experience in synthesizing KrF_2 , attempts were begun to synthesize XeCl_2 , vaporize it if possible, and photodissociate it to produce XeCl (B). Initial attempts to observe XeCl_2 in the vapor phase by looking at the far IR absorption spectrum could not be carried out because Cl_2 gas quickly destroyed the transmission of KRS-5 windows. Since there was no other infrared method at our disposal for observation of XeCl_2 it was decided to confirm the existence of XeCl_2 by photolyzing the gas immediately above the surface of a cold window.

Figure 1 shows the apparatus of the experiment. A cell with a cold window inside and two Suprasil windows for irradiation and observation

was mounted in a polystyrene dewar and placed next to a Febetron equipped with a coaxial diode. A very weak argon ion laser was passed through the coaxial diode and onto the cold window of the cell. In operation, the cold window was cooled to 77°K and xenon was allowed to condense on the window. A few torr of Cl_2 were then admitted to the cell and the argon-ion laser was turned on. After several minutes of irradiation the polystyrene dewar was filled with enough liquid nitrogen to condense the Cl_2 and the cold window was allowed to slowly warm up. While this was occurring the coaxial diode was filled with an Ar/F_2 mixture and irradiated to produce short ArF (193 nm) pulses to photolyze the XeCl_2 and produce the 308 nm XeCl (B-X) emission. On several runs a weak signal was observed, but these signals were obtainable for only a short period of time. This may be because of the rapid temperature rise which could quickly lead to XeCl_2 destruction; because of the small amount of XeCl_2 made due to the low power of the argon ion laser; or because of the rather low power ArF pulse.

Because of these difficulties it was decided to set aside these experiments until a higher power argon ion laser could be used and a better method of temperature control could be designed. It has become clear that synthesis of XeCl_2 is far more difficult than the synthesis of KrF_2 .

II. Measurement of Ground State Destruction

Of all the rare gas halide lasers only XeF and XeCl have bound ground states. In XeF the binding is of the order of 1065 cm^{-1} while in XeCl it is about 255 cm^{-1} , \sim KT at room temperature. The destruction rate constants for the lowest vibrational levels have been determined

by probing the absorption on several B \leftrightarrow X transitions with a frequency doubled tunable dye laser. The results of these measurements show that there are considerable differences in the destruction rate constants for the various gases used in the laser, but little or no differences between $v'' = 0, 1$ and 2 . This leads to the conclusion that rapid equilibration must be taking place among the various vibrational levels. In fact, this equilibration is necessary to account for the lack of bottlenecks in the XeCl laser. Further details of the measurements are contained in the preprint of the paper submitted to Applied Physics Letters which is included.

III. Fluorescence Measurements

Spectroscopic observations of the fluorescent emission from xenon chloride mixtures can assist in identifying the transient atomic, ionic and molecular species that take part in formation of the laser molecule. Temporally resolved, these observations can be compared with numerical model predictions and used to test the model. Both of these observations have been carried out with some success.

Vacuum ultraviolet observations on gas mixtures of interest for XeCl were carried out by attaching a 0.5 meter Seya-Namioka spectrograph to the coaxial diode which was mounted to the Febetron 706. The gas cell was separated from the spectrograph by a Bondelid valve with a LiF window inserted in its gate. This allowed the LiF window to be easily removed and the spectrograph to be filled with He to the same pressure as the gas cell for operation below the 105 nm LiF cutoff.

Since many key species in the kinetics scheme radiate in the vacuum ultraviolet (Ne $_2^*$ @ 80-100 nm, NeF @ 108 nm, NeCl @ < 100 nm, NeXe $^+$

120-160 nm, F_2 @ 155, etc.), it was thought that perhaps the entire kinetics chain could be studied by carefully monitoring the emission of the various species as a function of time and gas mixture. Since neon was the major gas component in the XeCl laser and the primary receiver of the electron beam energy, it was studied first. With a helium back-filled spectrograph it was relatively easy to resolve the Ne_2^* continuum at 85-100 nm and to see Ne^+ ion lines in the 120-180 nm region. Addition of a few torr of Xe, however, eliminated all emission from Ne_2^* probably because of photoionization of Xe. A small reduction in the Ne^+ lines was noted also. When pressures of Xe were increased from 10-100 torr the 147 nm resonance line from Xe grew very intense and at very high (500 torr) Xe pressures the Xe_2^* continuum at 172 nm appeared. No radiation was observed that could be attributed to $NeXe^+$ nor were any substantial changes observed when either a fluorine or chlorine donor was added to the mixture. No emission attributable to NeF^* or $NeCl^*$ could be observed.

Consequently, no evidence contrary to the predictions of the model was found, however, emission from the rare gas molecular ion ($NeXe^+$) or from the neon halide may have been absorbed by other species or not produced in sufficient quantity to be observable. It is now believed that stronger excitation would be produced using the commercially made axial Febetron e-beam tube rather than the coaxial diode. It may be advantageous to use this source to look for the existence of $NeXe^+$ and $NeCl^*$.

Fluorescence Parameter Study

Using the Febetron e-beam tube and a small gas cell equipped with Suprasil windows, the 308 nm fluorescence from XeCl was studied as a function of component gas mixture. These studies were expected to produce clear results of the formation kinetics without the additional complications of laser optics and to serve as a test of the numerical model.

Using a 308 nm band pass filter and a photomultiplier, time resolved fluorescence curves were recorded for numerous gas mixtures. Figure 2 shows the change in fluorescence pulse shape as a function of HCl pressure. The pulse appears to resolve two formation processes which the model suggests are an ionic channel predominant at high (1.0 torr) HCl pressures and a metastable formation channel which dominates at low HCl pressures. Figure 3 shows that the energy transfer from Ne^+ to Xe^+ is speeded up as xenon pressure is increased. Figure 4 shows the effect of Ne pressure on fluorescence. These curves are not as well explained, but real data such as this serves as a test of the numerical model. Further implications of this data and its relation to the model will be discussed later under the model performance.

XeF C State Quenching

The lifetime of the C state had been measured previously by a low-pressure electron impact dissociation technique. The C state quenching was not measured, but has become increasingly important both for XeF (B) state kinetics and for predicting the behavior of the XeF (C→A) blue-green laser. The measurements, using a photolysis of the dihalide

XeF₂, reconfirm the lifetime of XeF (C), 95 ± 7 ns, and the quenching rate constant of XeF₂. A summary of the data is given in the included preprint of the paper submitted to Applied Physics Letters.

References

1. J. G. Eden and R. W. Waynant, Opt. Lett. 2, 13 (1978); J. G. Eden and R. W. Waynant, J. Chem. Phys. 68, 2850 (1978); R. W. Waynant and J. G. Eden, IEEE J. Quant. Electron. 15, 61 (1979).
2. J. G. Eden, R. W. Waynant, S. K. Searles and R. Burnham, Appl. Phys. Lett. 32, 733 (1978); J. Appl. Phys. 49, 5368 (1978).
3. R. W. Waynant and J. G. Eden, Appl. Phys. Lett. 33, 708 (1978); J. G. Eden and R. W. Waynant, Appl. Phys. Lett. 34, 324 (1979).
4. L. Y. Nelson and G. C. Pimentel, Inorg. Chem. 6, 1758 (1967); L. Y. Nelson, Infrared Studies of Polyhalogen and Inert Gas Halogen Molecules, University Microfilms, Inc., Ann Arbor, MI, 1969.
5. D. Beal and G. A. S. Ozin, Spectroscopy Letters 4, 43 (1971); K. A. R. Mitchell, J. Chem. Soc. (A), 1637 (1969).
6. W. F. Howard, Jr. and L. Andrews, J. Am. Chem. Soc. 96, 7864 (1974).

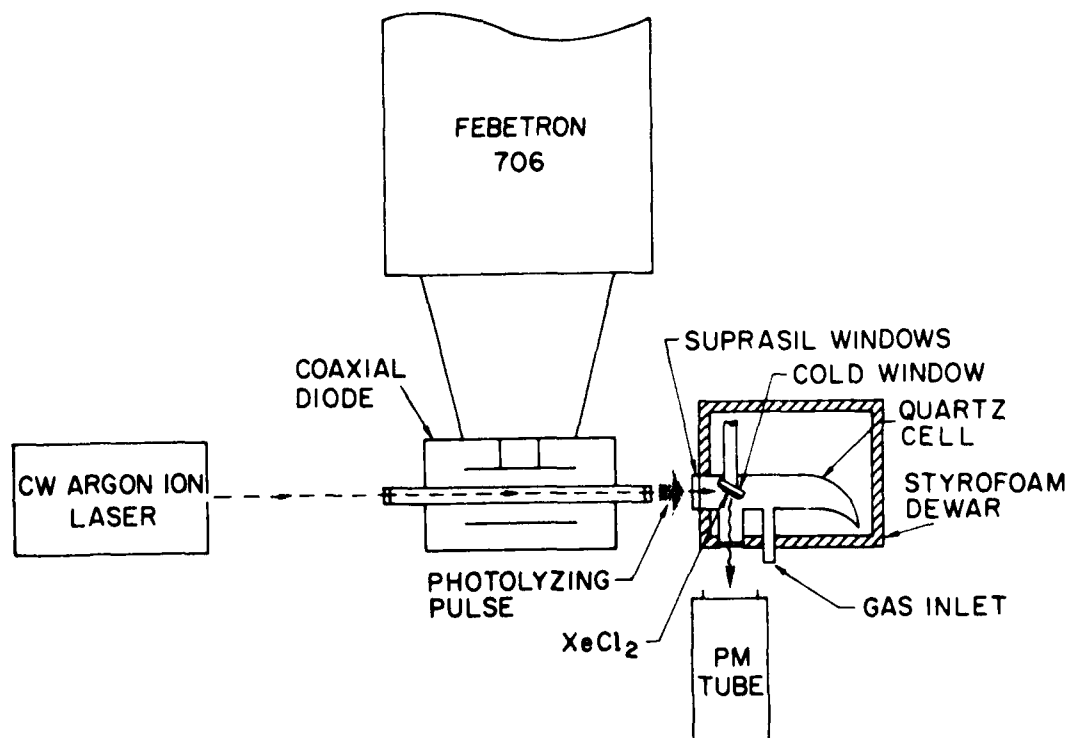


Figure 1. Schematic diagram of the experimental apparatus. The gas cell contained Ne/Xe/HCl gas mixtures typical of those used in e-beam pumped XeCl lasers.

XeCl FLUORESCENCE

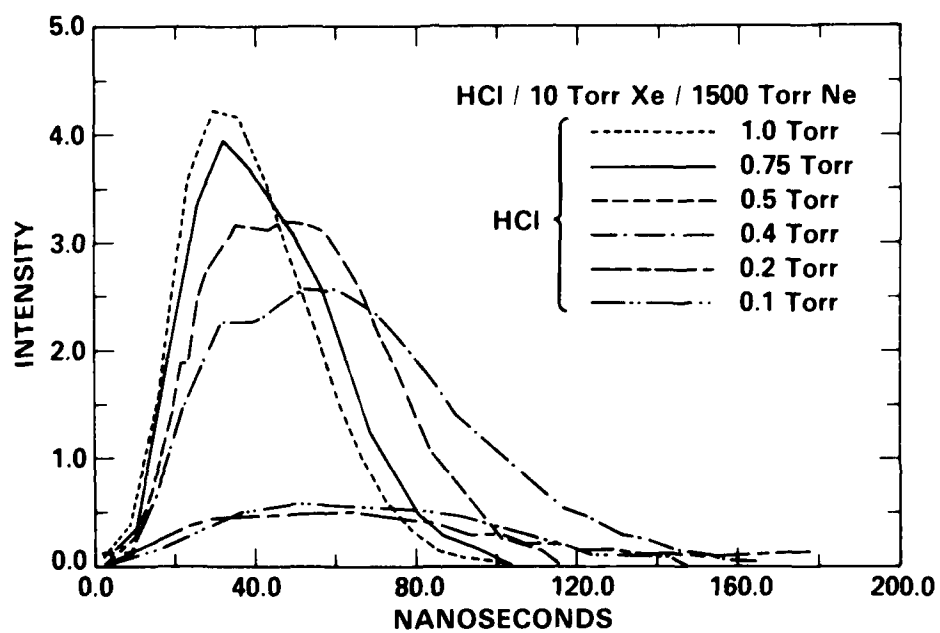


Figure 2. Time resolved fluorescence intensity from XeCl (B) as a function of HCl concentration.

XeCl FLUORESCENCE

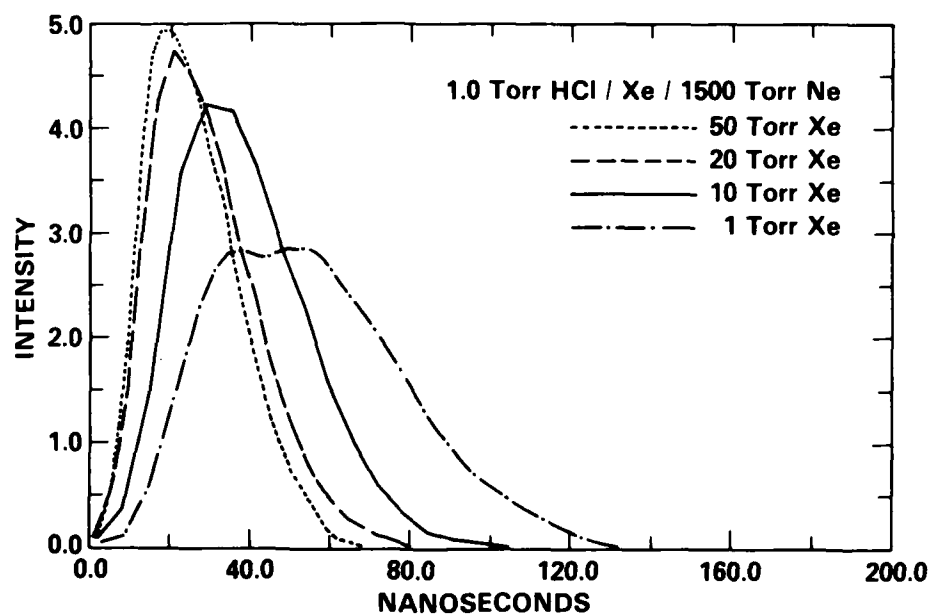


Figure 3. Time resolved fluorescence intensity from XeCl (B) as a function of xenon concentration.

XeCl FLUORESCENCE

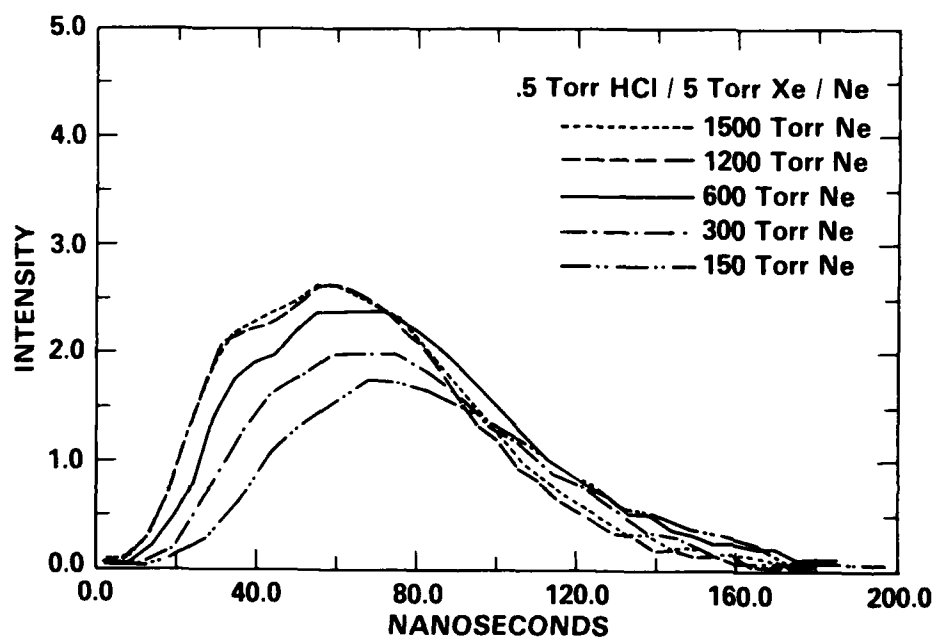


Figure 4. Time resolved fluorescence intensity from XeCl (B) as a function of neon concentration.

DESTRUCTION OF GROUND STATE XeCl
MOLECULES BY HCl AND RARE GAS COLLISIONS*

R. W. Waynant and J. G. Eden^a

Naval Research Laboratory
Washington, D. C. 20375

ABSTRACT

Rate constants for quenching of several XeCl (X) vibrational levels by the rare gases and HCl have been measured. The temporally resolved decay of the population densities of the XeCl (X, $v'' = 0-2$) levels was monitored using a frequency doubled, tunable dye laser. Within experimental error, the measured rate constants did not vary with vibrational number and the temperature dependence of the rates over the range $300^{\circ}\text{K} \leq T \leq 375^{\circ}\text{K}$ was found to be consistent with the previously measured XeCl (X) dissociation energy ($\sim 250 \text{ cm}^{-1}$). The rate constants for the destruction of XeCl (X, $v'' = 0$) state molecules by HCl, Xe, Ar and Ne at 300°K were determined to be $(2.2 \pm 0.5) \times 10^{-11}$, $(5.6 \pm 0.8) \times 10^{-12}$, $(0.6 \pm 0.06) \times 10^{-13}$ and $(1.0 \pm 0.15) \times 10^{-13} \text{ cm}^3\text{-sec}^{-1}$, respectively.

Several important rare gas halide molecules, XeF, XeCl and perhaps XeBr¹, have bound ground states. Consequently, the collisional destruction and dissociation rates for the ground state vibrational levels of these molecules are significant factors in determining laser performance. Fulghum and co-workers previously have studied^{2,3} the collisional decay rates for low-lying vibrational levels of the XeF (X) state and have concluded³ that VT processes rapidly equilibrate the X state vibrational manifold, and that the various vibrational levels decay at a common rate with dissociation primarily occurring from the highest v'' levels.

From an analysis of the XeCl emission spectrum, Tellinghuisen et. al. determined⁴ the XeCl (X) dissociation energy to be $\sim 255 \text{ cm}^{-1}$. Their studies indicated that twelve vibrational levels lie within the X state potential well. Further verification of the bound nature of the XeCl (X) state has been provided by Shostak and Strong¹ who, in recent photolysis experiments, observed transient UV absorption spectra corresponding to the XeCl $X \rightarrow B$ ($\lambda_{\text{max}} \sim 308 \text{ nm}$) and $X \rightarrow D$ (236 nm) bands.

Rate constants for collisional quenching of the XeCl (X, $v'' = 0-2$) levels by HCl and the rare gases have been measured and are reported here. These rates were determined by monitoring the exponential time decay of the population of the desired ground state vibrational level in the presence of a background gas mixture. In agreement with the results of Fulghum³, the rate constants measured in this work, within experimental error, were not found to depend on vibrational number. Also, the temperature dependence of the decay rates was examined and found to be consistent with $200 < D_0 [\text{XeCl (X)}] < 300 \text{ cm}^{-1}$.

Figure 1 is a simplified energy level diagram for XeCl indicating the vibrational transitions studied. Temporal resolution of the density of a

particular v'' level was obtained by observing the absorption of dye laser radiation on the (1-0), (0-2), and (2-1) transitions of the XeCl (B + X) band. The wavelengths for these transitions are 305.9, 308.2 and 304.4 nm, respectively.

The experimental apparatus used for these studies is shown schematically in Fig. 2. A frequency doubled dye laser, which could be tuned from 280 to \sim 320 nm, was used as the optical pump. The output of the laser had a pulse duration of \sim 1 μ s FWHM. The pulse contained approximately 1 mJ of energy and had a spectral linewidth of \sim 0.1 nm. After the beam was filtered to eliminate the fundamental frequency, it was split into two beams, one of which was passed through a stainless steel cell mounted on a Febetron 706 electron beam generator. From the vibrational level assignments of Tellinghuisen⁴, the dye laser wavelength was set to the desired vibronic transition of the X + B band using a 0.5 m Minuteman monochromator. Both the laser pulse transmitted through the gas cell and the reference signal were detected by photomultipliers and displayed on a dual-beam oscilloscope. To equalize their amplitude response and to suppress fluorescence from the e-beam cell, calibrated quartz neutral density filters were placed in front of the photomultipliers.

Data were taken with Ne/Xe/HCl (400:10:1) gas mixtures in the gas cell that are typical of those used in e-beam pumped XeCl lasers. The use of Cl₂ for these experiments was undesirable due to its broadband absorption in the 300 nm spectral region. Research grade purity rare gases were used for these experiments and the HCl purity was better than 99% (technical grade). All of the gases were used without further purification.

Roughly 100 ns after the start of the dye laser pulse, an intense (\sim 1 kA-cm⁻²) \sim 3 ns FWHM electron beam from the Febetron 706 entered the

gas cell, creating XeCl (B) state molecules. The subsequent radiative decay of the XeCl* molecules populated several vibrational levels of the ground state which, in turn, were eventually destroyed through collisions with the background gas.

An oscillogram illustrating absorption by the XeCl ($X, v'' = 0$) state in e-beam excited 98.6% Ne/1.2% Xe/0.2% HCl ($p_{\text{TOTAL}} \sim 800$ Torr) gas mixtures is shown in Fig. 3. Following the excitation of the gas mixture, spontaneous emission lasting ~ 100 ns was observed followed by strong absorption which persisted for ~ 300 ns. This absorption was observed only when both Xe and HCl were present in the Ne gas.

Oscillograms similar to Fig. 3 were recorded for various Ne/Xe/HCl gas mixtures (varying one constituent of the mixture while keeping the other two constant) and for the three $X \rightarrow B$ vibronic transitions mentioned earlier. For all of the gas mixtures studied, the time dependence of the ground state absorption ($\sim \ln I/I_0$ where I and I_0 are the transmitted and incident signal intensities, respectively) showed that the population of the X state vibrational level under study decayed exponentially over several time constants. Previous studies of the emission from Febetron excited Ne/Xe/HCl gas mixtures had shown that the XeCl ($B \rightarrow X$) fluorescence terminated 10-200 ns after the initiation of the e-beam pulse. Therefore, the extraction of exponential decay constants from the absorption data was performed 300-600 ns into the afterglow of the plasma.

Figure 4 shows the dependence of the exponential absorption decay constant (τ^{-1}) on the partial pressure of HCl. The 1-0 transition was probed by the dye laser and so the data reflect the decay of the XeCl ($X, v'' = 0$) state. The linear least-squares fit to the data is represented by the solid line. From the slope of this line, the rate constant for quenching of the $v'' = 0$ level by HCl was determined to be $(2.2 \pm 0.5) \times 10^{-11} \text{ cm}^3\text{-sec}^{-1}$.

The uncertainty given represents the standard deviation of the data about the least square linear fit. Table I summarizes the rate constants for quenching of several X state vibrational levels that were measured in these experiments. No dependence of the Ne quenching rate constants on the vibrational level (v'') probed was observed. This is in agreement with previous work on XeF.³

The rate constants presented here differ widely for the various quenching gases investigated. This represents a departure from the results of Fulghum and co-workers.³ In their studies of collisional equilibration in the XeF ground state, the decay rates for the $v'' = 1$ level using He and Ne buffers were found to be the same to within experimental error. This discrepancy could be due to the rather similar collisional cross sections for He and Ne which would have hidden the differences in the XeF experiment. The larger rate constants observed here are for Xe and HCl which would have larger collisional cross sections. An alternative explanation could be that dissociation from all v'' levels is more important for XeCl, which has a low binding energy ($\sim kT$ or 255 cm^{-1}), than it is for the low-lying levels of XeF (X).

The temperature dependence of the rate constants in Table I was also investigated by heating the e-beam gas cell. Heating tape was wrapped around the cell and a chromel-alumel thermocouple was positioned inside the cell immediately adjacent to the path of the probe laser. With this arrangement, temperatures in the range 300 to 375°K could be studied. As the cell temperature was elevated, the rate constants were found to obey the relationship $k_Q \sim e^{-\Delta E/kT}$ gas where $200 \text{ cm}^{-1} \leq \Delta E = D_0(X) < 300 \text{ cm}^{-1}$ which is consistent with the ground state dissociation energy reported by Tellinghuisen.⁴ Also, for temperatures in excess of

~ 350⁰K, the XeCl fluorescence and, hence, the ground state absorption decreased dramatically which could be due to reaction of HCl with the cell walls.

In summary, the rate constants for quenching of the $v'' = 0-2$ levels of the XeCl ground state by HCl and the rare gases have been measured. Within the experimental error, the rate constants did not depend on v'' and the temperature dependence of the rates over the range $T = 300-375^0\text{K}$ was found to be consistent with the X state dissociation energy measured previously. Knowledge of the XeCl (X) quenching rate constants reported here are useful for modeling of quasi-steady state ($> 0.5 \mu\text{s}$ pulse length) XeCl lasers.

The authors gratefully acknowledge the partial financial support of DARPA, discussions with N. Djeu and C. H. Fisher and the technical assistance of D. Epp and K. Tayman.

REFERENCES

^aPresent address: Department of Electrical Engineering, University
of Illinois, Urbana, IL 61801

1. S. L. Shostak and R. L. Strong, Chem. Phys. Lett. 63, 370 (1979).
2. S. F. Fulghum, I. P. Herman, M. S. Feld and A. Javan, Appl. Phys. Lett. 33, 926 (1978).
3. S. F. Fulghum, M. S. Feld and A. Javan, Appl. Phys. Lett. 35, 247 (1979).
4. J. Tellinghuisen, J. M. Hoffman, G. C. Tisone and A. K. Hays, J. Chem. Phys. 64, 2484 (1976).

TABLE I. Summary of the rate constants for quenching of the X state $v'' = 0-2$ vibrational levels at $T = 300$ K by HCl and the rare gases.

Transition Probed $v' - v'' (\lambda, \text{nm})^4$	Quencher	$k_Q (\text{cm}^3 - \text{sec}^{-1})$
1-0 (305.9)	HCl	$(2.2 \pm 0.5) \times 10^{-11}$
	Ne	$(1.0 \pm 0.15) \times 10^{-13}$
	Ar	$(0.6 \pm 0.06) \times 10^{-13}$
	Xe	$(5.6 \pm 0.8) \times 10^{-12}$
2-1 (304.3)	Ne	$(1.0 \pm 0.13) \times 10^{-13}$
0-2 (308.2)	Ne	$(1.0 \pm 0.07) \times 10^{-13}$

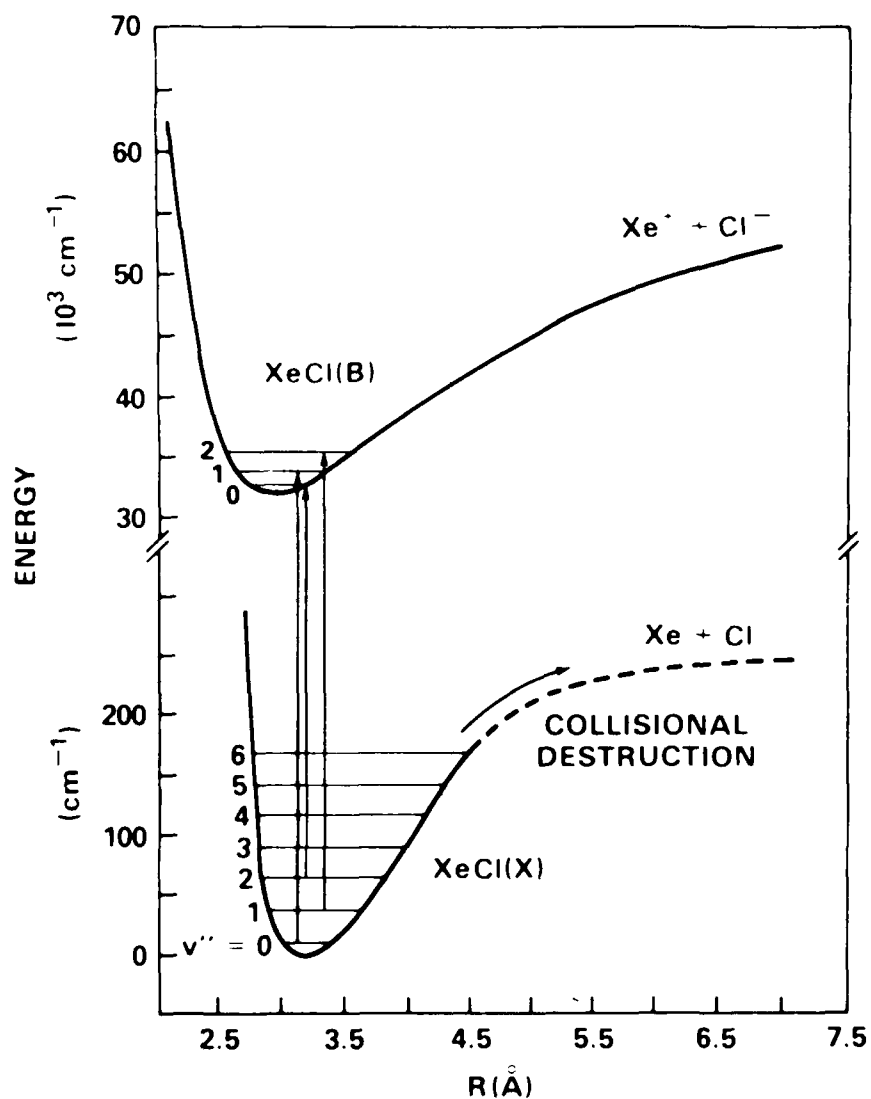


Figure 1. Partial energy level diagram for the XeCl molecule showing the absorption transitions probed by the dye laser to study the populations in $v'' = 0, 1$ and 2 levels of the X state.

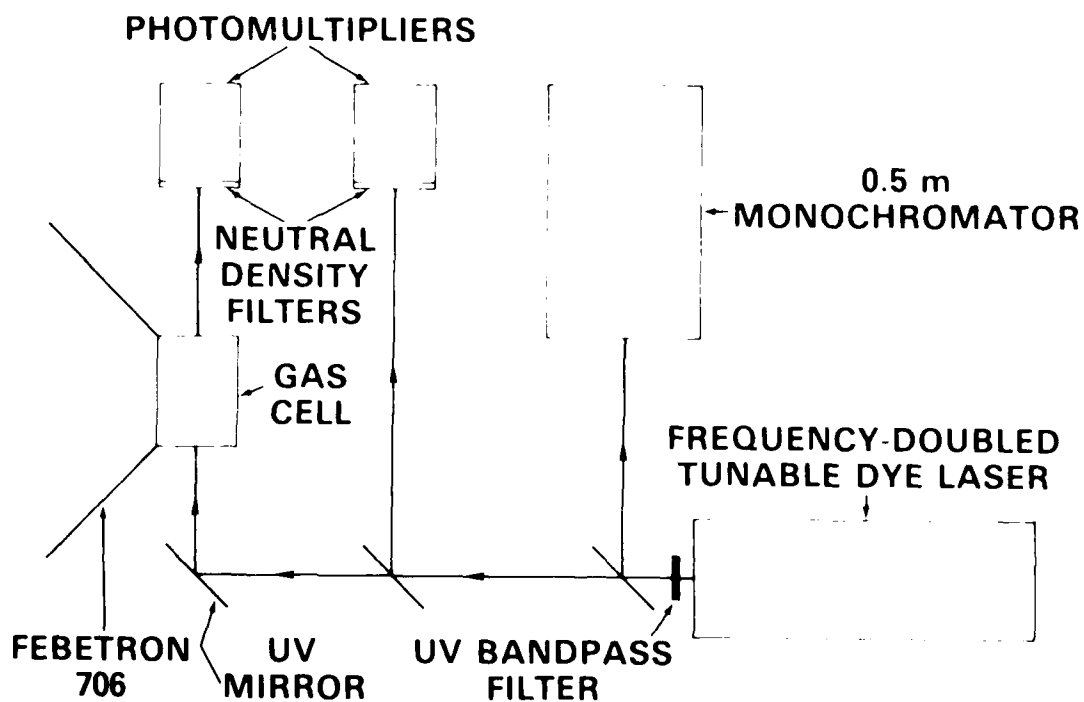


Figure 2. Schematic diagram of the experimental apparatus. The gas cell contained Ne/Xe/HCl gas mixtures typical of those used in e-beam pumped XeCl lasers.

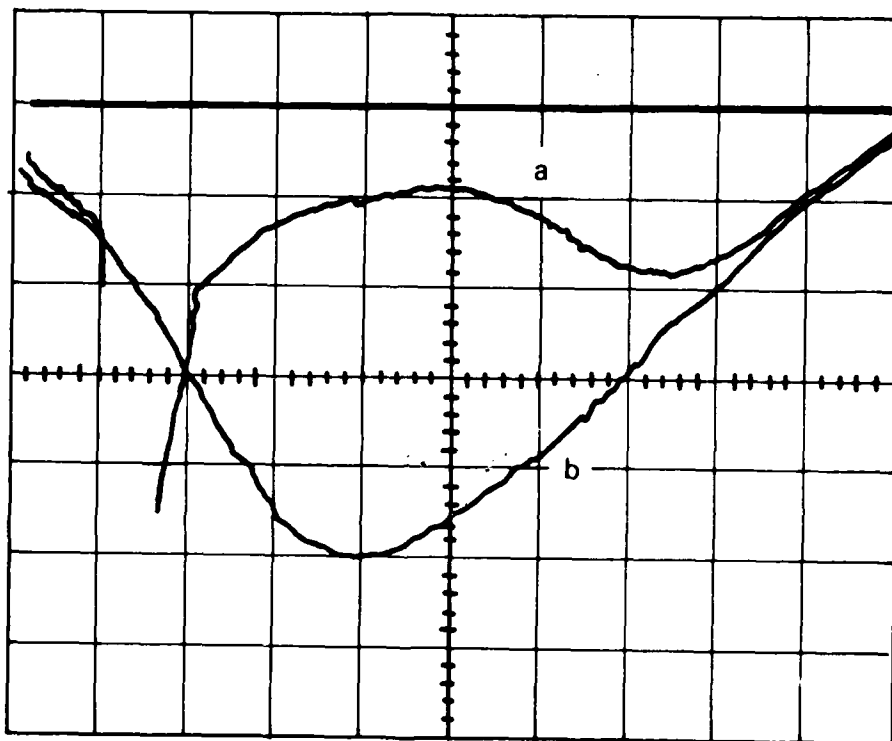


Figure 3. Oscillogram of XeCl (X) absorption in an e-beam excited 98.6% Ne/1.2% Xe/0.2% HCl ($p_{\text{TOTAL}} \sim 800$ torr) gas mixture. The transitions probed is the 1-0 line (305.9 nm) and both the transmitted (a) and incident (b) laser signals are shown. The initial surge in the signal transmitted by the gas cell is due to XeCl (B \rightarrow X) fluorescence. Scales are 100 ns/div; 10 mv/div.

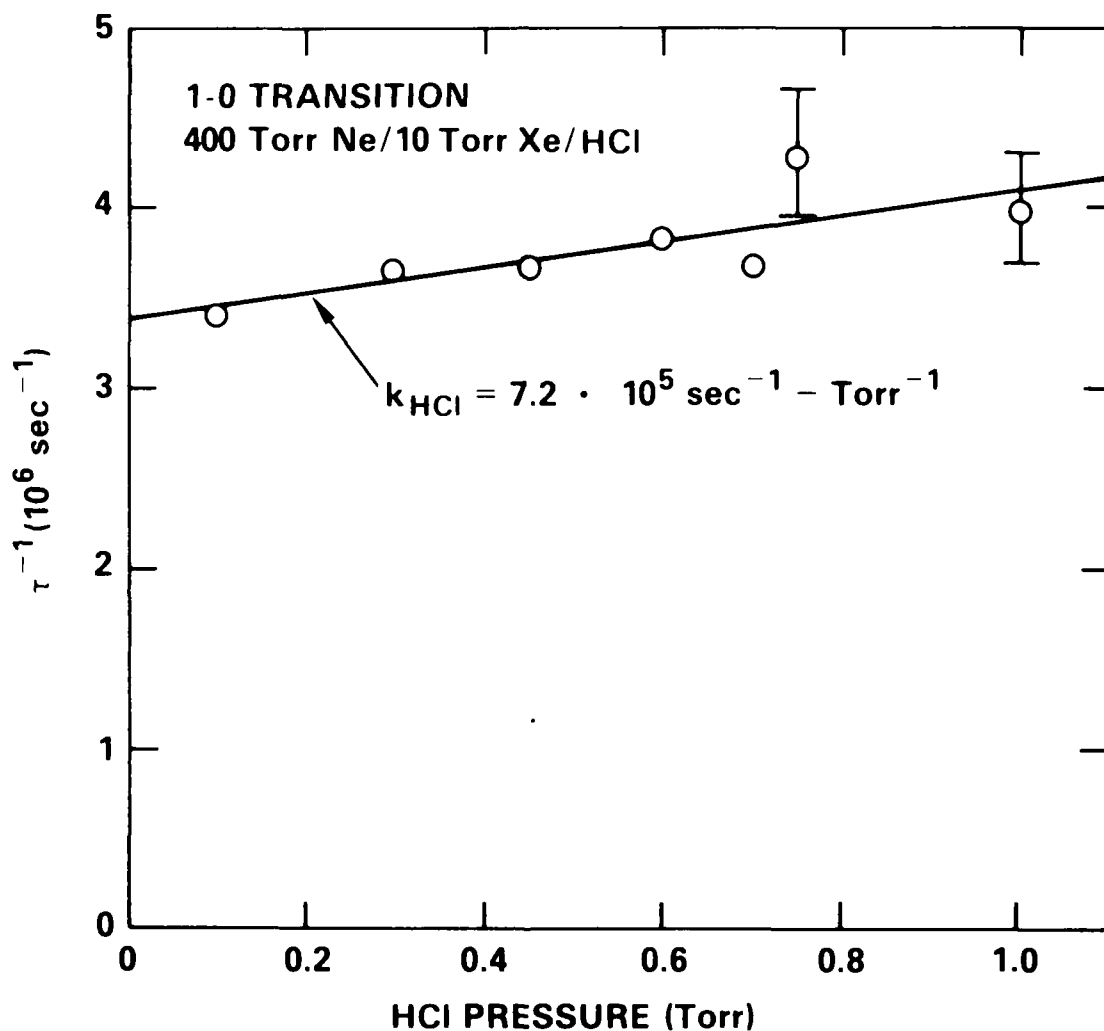


Figure 4. Dependence of the exponential absorption decay constant (τ^{-1}) on the partial pressure of HCl in Ne/Xe/HCl gas mixtures. The graph reflects the decay of the $v'' = 0$ level of the X ground state and the two error bars shown are representative of the uncertainty (standard deviation = $\pm 1.7 \times 10^5 \text{ sec}^{-1} \text{ torr}^{-1}$) in the data.

XeF (C) STATE LIFETIME AND QUENCHING
BY RARE GASES AND FLUORINE DONORS

R. W. Waynant
Naval Research Laboratory
Washington, D. C. 20375

ABSTRACT

The lifetime and quenching rate constants for the XeF (C) state have been measured when that state is produced by flash photolysis of XeF₂ in the presence of such quenching gases as He, Ne, N₂, Xe, Ar, XeF₂, NF₃ and F₂. The lifetime measured in this manner is 95 ± 7 ns and the quenching rate constants are 1.2×10^{-13} , 3×10^{-13} , 4×10^{-13} , 1×10^{-12} , 9×10^{-14} , 1.7×10^{-10} , 1.6×10^{-11} , 8×10^{-11} cm³ · sec⁻¹, respectively.

The kinetics of the C state of the XeF molecule are of interest both because of its close proximity to the B state previously made to lase¹ and because of recent observations²⁻⁵ of laser action on the C-A transition in the 480-490 nm region. Previous measurements⁶ of the XeF (C) state radiative lifetime and the quenching by XeF₂ were made by electron impact dissociation of XeF₂. This work re-examines the lifetime of XeF (C) and measures the quenching of the C state by numerous gases by the method of photodissociating XeF₂ in the presence of itself and quenching gases. The results reconfirm previous measurements of the XeF (C) state lifetime and quenching rate constant indicating little effect from electrons in the previous measurements.

These measurements of lifetime and quenching of XeF (C) were made using the photolysis system shown in Fig. 1. This apparatus was very similar to the previous system used to measure lifetimes and quenching rate constants for XeF (B)^{7,8} and KrF (B)^{9,10}. By increasing the x-ray shielding which isolates the electron beam and gas cell from the detector, it was possible to operate on a sufficiently sensitive scale that the 450-550 nm photons from XeF (C) state decay could be recorded reliably.

In operation the Febetron 706 produced a ~ 3 ns FWHM pulse of 600 keV electrons which passed through the foil of the Hewlett Packard type 5515 e-beam tube. When these electrons passed into the gas cell containing 2000 Torr Ar and 20 Torr Cl₂, short ArCl pulses (175 nm) were produced which, as previously seen,^{7,8} dissociated XeF₂ very rapidly into XeF (B), XeF (C), etc. The 450-550 nm photons from the XeF (C→A) decay were allowed to pass through a bandpass filter onto the photocathode of an F 4018 photodiode while the stronger XeF (B→X) ultraviolet emission was rejected. The photodiode signal was recorded by photographing the display of the fast Tektronix 7904 oscilloscope.

To measure the XeF (C) state radiative lifetime and quenching rate constant, the XeF₂ pressure was varied from ~ 0.1 Torr to 2 Torr. The oscillograms were manually digitized, plotted on a semi-log scale to determine the decay time, τ , and the decay rates (τ^{-1}) were plotted versus pressure. Since the measured decay rate τ^{-1} is given by

$$\tau^{-1} = \tau_r^{-1} + K_Q [\text{XeF}_2] \quad (1)$$

where τ_r^{-1} is the radiative lifetime, K_Q is the quenching rate constant and $[]$ denote particle densities (cm^{-3}), the graph slope is K_Q and the zero pressure intercept is the radiative lifetime. From Fig. 2 the quenching rate constant, K_Q , is $(1.7 \pm 0.1) \times 10^{-10} \text{ cm}^3 \cdot \text{sec}^{-1}$ and the XeF (C) state lifetime is $95 \pm 7 \text{ ns}$. Within experimental error these numbers agree very well with the $93 \pm 5 \text{ ns}$ lifetime and $(1.8 \pm 0.5) \times 10^{-10} \text{ cm}^3 \cdot \text{sec}^{-1}$ quenching rate constant determined previously by electron impact dissociation of XeF₂. This would confirm the assumption that electron quenching of the XeF (C) state was very small in the previous experiment⁶ and that electron mixing of the B and C states also was not important in that experiment since it did not result in a significantly faster decay from XeF (C). These numbers are in reasonable agreement with those of Black et. al.¹¹ ($100 \pm 10 \text{ ns}$, $5 \times 10^{-10} \text{ cm}^3 \cdot \text{sec}^{-1}$) who studied XeF (C) by photodissociation of XeF₂ with synchrotron radiation.

In the above analysis, it is necessary that the dissociation of XeF₂ into XeF* and F be a small percentage of the total gas such that quenching, etc. by dissociation products is small. Further, when other quenching gases are added, such that

$$\tau^{-1} = \tau_r^{-1} + K_{\text{XeF}_2} [\text{XeF}_2] + K_Q [Q] \quad (2)$$

then $[\text{XeF}_2]$ must be kept small enough that $K_{\text{XeF}_2} [\text{XeF}_2]$ is small compared to $K_Q [Q]$.

Measurement of the quenching of gases likely to be used in XeF (C-A) lasers was carried out using a fixed pressure of XeF_2 of 0.1-0.5 Torr. Data was recorded and analyzed in a manner similar to the quenching analysis of XeF_2 above. A summary of the rate constants determined for the XeF C state as well as those previously determined for the B state^{7,8} are given in Table I.

Studies of XeF C state quenching have been carried out both by Black et. al.^{11,12} and by Brashears and Setser.¹³ Black et. al. give rate constants only for N_2 ($2.5 \times 10^{-14} \text{ cm}^3 \cdot \text{sec}^{-1}$) and Ar ($7 \times 10^{-15} \text{ cm}^3 \cdot \text{sec}^{-1}$), but these values are significantly lower than determined here. While full details of that experiment are not yet available, a possible explanation is that additional quenching may take place due to photolysis products at low quenching gas pressures. This would lead to a more flat rate versus pressure curve and a lower rate constant. Brashears and Setser¹³ have studied B and C state quenching and B-C energy transfer using a steady state technique. Comparison with their results is difficult because they used a C state lifetime of 150 ns in their calculations and give results in terms of the transfer rate constant. However, their results for B state quenching agree well with those of Table I and their implied C state quenching rate constant for He ($\leq 2 \times 10^{-13} \text{ cm}^3 \cdot \text{sec}^{-1}$) agrees with the value determined here.

The uncertainty expressed in the C state quenching rate constants is the standard deviation of the data about the linear least squares fit. In the case of xenon the data appeared to show a slight quadratic dependence, but a quadratic least squares fit over the pressures used

(700 Torr max) resulted in greater uncertainty about the fitted line than the linear fit.

In summary, the radiative lifetime of XeF (C) was determined by a photolysis experiment and found to agree very well with a previous measurement using electron impact dissociation. Quenching rate constants for XeF (C) have been presented for gases likely to be used in the XeF C state laser.

The author appreciates discussions of this problem with L. J. Palumbo.

REFERENCES

1. See C. K. Rhodes ed., Excimer Lasers, Springer-Verlag, New York, 1979 and references therein.
2. W. K. Bischel, H. H. Nakano, D. J. Eckstrom, R. M. Hill, D. L. Huestis and D. C. Lorents, Appl. Phys. Lett. 34, 567 (1979).
3. W. E. Ernst and F. K. Tittel, Appl. Phys. Lett. 35, 36 (1979).
4. R. Burnham, Appl. Phys. Lett. 35, 48 (1979).
5. C. H. Fisher, R. E. Center, G. J. Mullaney and J. P. McDaniel, Appl. Phys. Lett. 35, 26 (1979).
6. R. W. Waynant and J. G. Eden, IEEE J. Quantum Electron. 15, 61 (1979).
7. J. G. Eden and R. W. Waynant, Opt. Lett. 2, 13 (1978).
8. J. G. Eden and R. W. Waynant, J. Chem. Phys. 68, 2850 (1978).
9. J. G. Eden, R. W. Waynant, S. K. Searles and R. Burnham, Appl. Phys. Lett. 32, 733 (1978).
10. J. G. Eden, R. W. Waynant, S. K. Searles and R. Burnham, J. Appl. Phys. 49, 5368 (1978).
11. G. Black, R. Sharpless, D. C. Lorents, R. Gutcheck, T. Bonifield, D. Helms and G. K. Walters, Abstract TuA6, Technical Digest Excimer Lasers, Optical Society of America, Washington, D. C., 1979.
12. D. C. Lorents, (private communication).
13. H. C. Brashears, Jr. and D. W. Setser, Appl. Phys. Lett. 33, 821 (1978).

TABLE I^a

	XeF (B) ^{7,8}	XeF (C)
He	$(4.07 \pm 1.46) \times 10^{-13}$	$(1.2 \pm 0.2) \times 10^{-13}$
Ne	$(7.68 \pm 1.6) \times 10^{-13}$	$(3 \pm 0.1) \times 10^{-13}$
Ar	$(4.92 \pm 1.56) \times 10^{-12}$	$(9 \pm 0.1) \times 10^{-14}$
Xe	$(3.27 \pm 0.74) \times 10^{-11}$	$(1 \pm 0.5) \times 10^{-12}$
F ₂	$(3.80 \pm 0.13) \times 10^{-10}$	$(8 \pm 0.2) \times 10^{-11}$
NF ₃	$(2.8 \pm 0.15) \times 10^{-11}$	$(1.6 \pm 0.2) \times 10^{-11}$
XeF ₂	$(2.56 \pm 0.32) \times 10^{-10}$	$(1.7 \pm 0.1) \times 10^{-10}$
N ₂		$(4 \pm 0.4) \times 10^{-13}$

^aAll units: cm³ · sec⁻¹

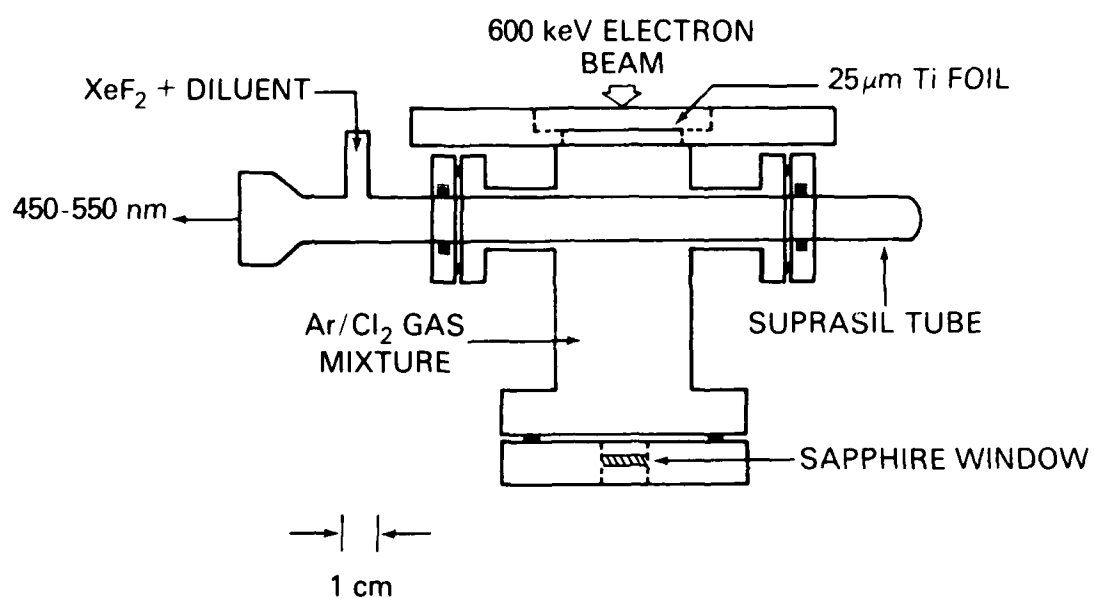


Figure 1. Diagram of photolysis apparatus used to study XeF (C).

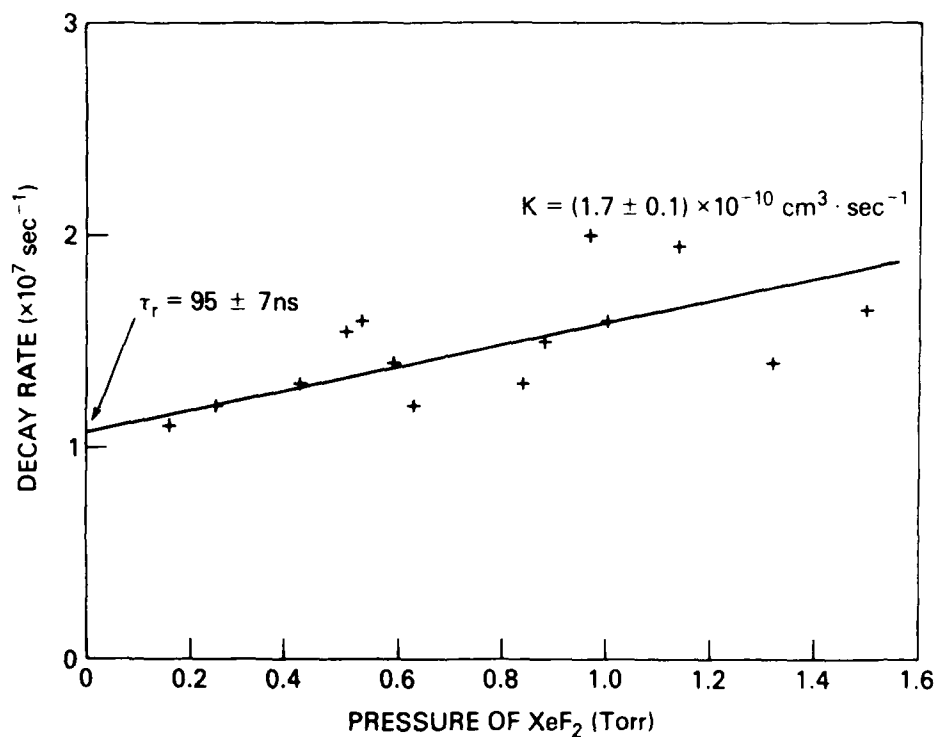


Figure 2. Plot of XeF (C) fluorescent decay rate as a function of XeF_2 pressure. The zero pressure intercept gives the radiative lifetime and the slope gives the rate constant.

LONG PULSE KINETICS

Formation and quenching processes for the XeCl (B \rightarrow X) state and the XeF (B \rightarrow X) state were investigated. The long-pulse kinetics cell used in these experiments permits observation of fluorescence intensities and information about formation efficiency to be obtained under conditions which closely approximate actual laser pumping conditions. The role of the (C \rightarrow A) state in both the XeCl and XeF laser system is also discussed. Of significance we find that if the B and C states of the XeCl laser are closely coupled then the ultimate efficiency of the XeCl laser could approach $17 \pm 4\%$.

Kinetics of the XeCl (B \rightarrow X) Laser

Formation and quenching processes of the XeCl (B) state have been investigated. Mixtures of Ne/Xe/HCl have been irradiated by an electron beam of 0.6 μ sec duration. The results indicate that the formation efficiency of the XeCl (B) and (C) states are $14 \pm 3\%$ and $3 \pm 1\%$, respectively. If these states are closely coupled, the ultimate efficiency of the XeCl (B \rightarrow X) laser is $17 \pm 4\%$. Two-body quenching by neon is the major loss process. At a pumping current of 7 A/cm^2 , electron mixing of the B and C states is negligible; however, electron quenching may be present, and at most a 20% effect.

The XeCl laser has only recently been developed to high efficiency and output power. Initially the laser was operated with argon as the diluent and chlorine as the halogen donor¹ but absorption in the medium prevented efficient operation just as in the case of the XeF laser.² The use of neon as the diluent and HCl as the donor has significantly reduced the absorption at the laser wavelength, 308 nm, such that the power efficiency of the laser has climbed to 6.5%.³ To determine the ultimate efficiency and performance of the laser, one requires a detailed knowledge of the laser kinetics. In this paper we report the results of our investigations of the formation and quenching kinetics of the XeCl laser.

The apparatus has been described previously⁴ as has our experimental method;⁵ therefore, we will not discuss them. We have added a focusing electrode which increases the peak current density into the gas to 7 A/cm² and shortens the pulse length to 0.6 μ sec.

The experiments consist of measuring the emission intensity of XeCl (B \rightarrow X) and (C \rightarrow A) transitions, at 308 and 340 nm respectively, from the electron beam excited Ne/Xe/HCl mixtures.⁶ The intensities were studied as a function of pumping current density (2 to 7 A/cm²), neon pressure (0.5 to 5 atm), xenon pressure (1 to 180 torr) and HCl pressure (1 to 40 torr). In each case, except for the parameter being varied, the data were taken under conditions which gave optimized laser performance, namely, 4 atm Ne/30 torr Xe/2 torr HCl at 7 A/cm².

The purpose of these experiments is threefold. First, to obtain the apparent rate constants for quenching of the XeCl (B) state by species in the laser mixture. Second, to measure the formation efficiency of the XeCl (B) and (C) states. Third, to estimate the apparent rate constants for quenching and mixing by electrons. All of these quantities

are important in characterizing the laser. Furthermore, these quantities can vary under different pumping conditions or mixtures. In other words, they are more like bulk properties of the mixture than specific properties of atoms or molecules. Therefore, to obtain an accurate assessment of the XeCl laser kinetics we must reproduce as closely as possible the optimum operating conditions of the laser which are stated above.

The apparent quenching rate constants were obtained by varying the species concentration and measuring the fluorescence intensity of the B state. For Xe and HCl, the rate constants were determined by plotting the data as a Stern-Volmer plot, that is, with I_0/I versus quencher concentration. The slope of the plot is equal to the product $k \tau_{\text{eff}}$ where τ_{eff} is the effective lifetime.⁷ For the neon constant the procedure is more complicated because the energy deposited varies with neon pressure. To account for this we must divide the data by the neon pressure. In Fig. 1 the XeCl (B \rightarrow X) and (C \rightarrow A) fluorescence data is given as a function of neon pressure. By dividing the data by the neon pressure and plotting its inverse, we obtain a Stern-Volmer plot as shown in Fig. 2. The slope of the (B \rightarrow X) data in Fig. 2 is the product $k \tau_{\text{eff}}$. As we shall see later the neon data in Fig. 2 can be used to determine the formation efficiency.

The apparent quenching rate constants are important because they give insight into the kinetics of the plasma. If an apparent rate constant differs substantially from the true rate constant, it means that the species has an important additional effect in the laser plasma which must be understood. For example, if the apparent rate constant is higher it implies that interception is present. In Table I, the

apparent rate constants for quenching the XeCl (B) state are given based on a radiative lifetime of 11 nsec calculated by Dunning and Hay.⁶ Our data indicate that there is little or no interception due to Ne and Xe but interception by HCl may be present. The neon rate constant is in good agreement with the B-C mixing rate constant of $8 \times 10^{-13} \text{ cm}^3/\text{sec}$ as reported by Brashears et. al.⁸ The xenon rate constant is larger than the value reported by Fisher et. al.⁹ of $1 \times 10^{-11} \text{ cm}^3/\text{sec}$, however the apparent quenching due to xenon is small. On the other hand, quenching by HCl is significant so that the disagreement with Fisher's value⁹ of $8 \times 10^{-10} \text{ cm}^3/\text{sec}$ may be due to interception. However, our Stern-Volmer plot of the HCl data is not linear (possibly due to depletion of HCl) so that it is difficult to estimate the amount of interception in the optimum laser mixture.

The formation efficiency is obtained by measuring the fluorescence efficiency over a wide neon pressure range and extrapolating to zero pressure. The best way to analyze the data is in terms of the fluorescence yield which is defined here as the number of photons emitted from a state divided by the number of neon excitations (Ne^+ and Ne^*) produced by the electron beam.¹⁰ The fluorescence yield is obtained by dividing the emission intensity by the neon pressure.

To obtain absolute fluorescence yields, we have calibrated the XeCl* emission against the N_2 second positive (C-B) band emission from Ar + 5% N_2 mixtures excited in the same apparatus. The fluorescence yield for the Ar- N_2 system has been determined in previous studies¹¹ to be $0.176/P$ per argon excitation formed, where P is the argon pressure in atm. At 4 atm Ne/30 torr Xe/2 torr HCl and 7 A/cm^2 , the fluorescence yield is 0.71 for the (B-X) system and 0.23 for the (C-A) system; or expressed in terms of fluorescence energy efficiency, 10% and 3% respectively.

The formation efficiency is obtained by plotting the inverse of the fluorescence yields and extrapolating to zero pressure as shown in Fig. 2. In the limit of zero neon pressure, the fluorescence yield approaches 1.0 ± 0.2 for B \rightarrow X and 0.25 ± 0.08 for C \rightarrow A, which corresponds to formation efficiencies of $14 \pm 3\%$ and $3 \pm 1\%$, respectively. If the B and C states are coupled so that all the excitation in the C state can be extracted, the ultimate laser efficiency is $17\% \pm 4\%$. Although the B to C formation ratio is four to one, the B to C steady state population ratio is much less because the C state does not decay rapidly and its population builds up.

The extent of electron mixing in the optimum laser mixtures was estimated by measuring the B and C state emission ratio as a function of the steady state electron density. The electron density was changed by varying the pumping current from 2 to 7 A/cm² which increases steady state electron density by a factor of about three according to our XeCl model calculations. Over this pumping regime, the observed (B \rightarrow X) to (C \rightarrow A) fluorescence ratio increased only slightly, from 4.3 to 4.9. The small change in the ratio implies either that the B and C states are already well mixed by electron collisions or that electron collisions are not the dominant mixing process even at 7 A/cm². The states are not well mixed by electrons for two reasons. First, the B to C emission ratio of 4.9 is too low. Based on 0.025 eV as the B-C energy separation,⁸ $\tau = 11$ nsec for the B state, $\tau = 120$ nsec for the C state⁶ and an electron temperature of > 0.25 eV, the emission ratio should be 11, not 4.9 as we have observed. Second, the mixing rate constant is too high. According to our model calculations, a rate constant of 8×10^{-6} cm³ sec⁻¹ is required to mix the states well at the low pumping current of 2 A/cm². On the other hand,

the states appear to be mixed by heavy particles. Our observed B to C state emission ratio is close to the high pressure limit of 3.6 observed by Brashears et. al.⁸ in an essentially electron free environment. Therefore, we conclude there is little electron mixing in the 2-7 A/cm² range.

Since electron mixing of the B and C states is negligible, a less than linear increase in B state emission with pumping current would indicate electron quenching. We observed slightly less than linear relationship between fluorescence and current. At 7 A/cm² the magnitude of this effect is about 20%, compared to the 20% uncertainty of our measurements.

From our results we draw the following conclusions about the XeCl (B) laser:

1. The ultimate efficiency can be as high as 17%.
2. Under optimum laser conditions, two-body quenching by Ne is the major loss process for XeCl* (B).
3. Electron quenching and mixing are not significant up to a pumping current of 7 A/cm².

As a final point, the results for XeCl are similar to our XeF results⁵ especially in terms of formation efficiency of the B and C states.

We thank D. W. Setser of Kansas State University for a preprint of reference 8 and C. H. Fisher of Mathematical Sciences Northwest for use of his unpublished data and acknowledge the useful discussion with W. T. Whitney on the design of the focusing electrode. We are also grateful to D. M. Shores and K. Tayman for their technical assistance.

References

1. J. J. Ewing and C. A. Brau, Appl. Phys. Lett. 27, 350 (1975).
2. L. F. Champagne and N. W. Harris, Appl. Phys. Lett. 31, 513 (1977).
3. L. F. Champagne, Appl. Phys. Lett. 33, 523 (1978).
4. N. W. Harris, F. O'Neill and W. T. Whitney, Appl. Phys. Lett. 25, 148 (1974).
5. T. G. Finn, L. J. Palumbo and L. F. Champagne, Appl. Phys. Lett. 34, 52 (1979).
6. Contributions to 340 nm emission from B+A have been taken into account.
c.f. P. S. Julianne and M. Krauss, Appl. Phys. Lett. 35, 55 (1979);
and P. J. Hay and T. H. Dunning, Jr., J. Chem. Phys. 69, 2209 (1978).
7. The effective lifetime is defined here as:

$$\frac{1}{\tau_{\text{eff}}} = \frac{1}{\tau_{\text{rad}}} + k_1 [Q_1] + k_2 [Q_2]$$

where τ_{rad} is the radiative lifetime, Q_1 and Q_2 are the other neutral species in the mixture and k_1 and k_2 are their respective quenching rate constants.

8. H. C. Brashears, Jr. and D. W. Setser, J. Phys. Chem. (in press).
9. C. H. Fisher, R. E. Center and J. P. McDaniel, 32nd Annual Gaseous Electronics Conference, Pittsburgh, PA, paper AB-3 (1979).
10. The fluorescence yield can be higher than unity because the electron beam and secondary electrons also excite Xe^+ and Xe^* which can lead to the upper laser level. We normalize to Ne excitation, because the Ne^+ formation can be calculated from energy deposition measurements and the W value of 36.4 eV, which is the energy required to produce a Ne^+-e^- pair. We assume the Ne^* and Ne^+ species are

formed in the ratio of 0.3 to 1.0 c.f. L. R. Peterson and J. E. Allen, Jr., J. Chem. Phys. 56, 6068 (1972).

11. D. H. Heustis, R. M. Hill, D. J. Eckstrom, M. V. McCusker, D. C. Lorents, H. H. Nakano, B. E. Perry, J. A. Margevicius and N. E. Schlotter, Stanford Research Institute International Report N. MP 78-07, 1978 (unpublished); recent results reduce the uncertainty to $< \pm 10\%$. D. J. Eckstrom (private communication).

TABLE I
Collisional Quenching of XeCl (B) State

Species	Apparent Quenching Rate Constant
Ne	$1.0 \times 10^{-12} \text{ cm}^3/\text{sec} (\pm 30\%)$
Ne + Ne	$< 1 \times 10^{-33} \text{ cm}^6/\text{sec}$
Xe	$3.2 \times 10^{-11} \text{ cm}^3/\text{sec} (\pm 35\%)$
HCl	$1.4 \times 10^{-9} \text{ cm}^3/\text{sec} (\pm 40\%)$

The rate constants have been evaluated with $\tau_{\text{rad}} = 11 \text{ nsec}$ as calculated by Hay and Dunning.⁶

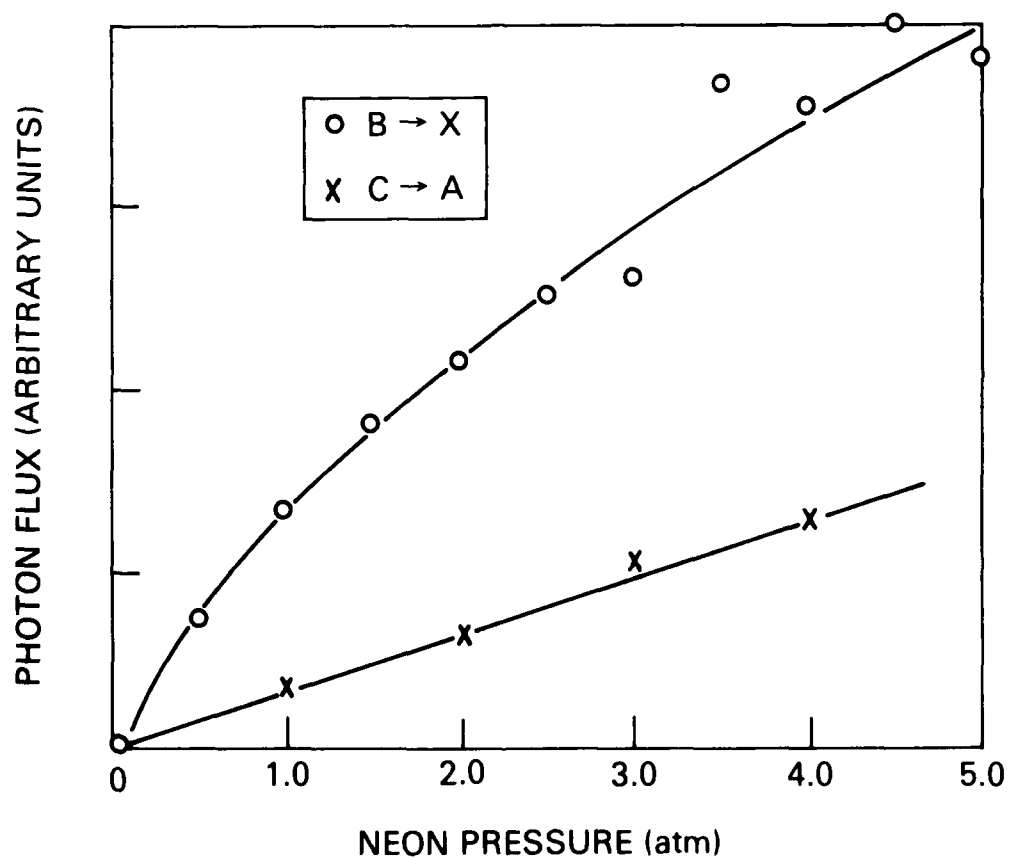


Figure 1. Observed fluorescence of XeCl ($B \rightarrow X$) and ($C \rightarrow A$) transitions as a function of neon pressure at 7 A/cm². Xenon and HCl pressures were held at 30 torr and 2 torr, respectively.

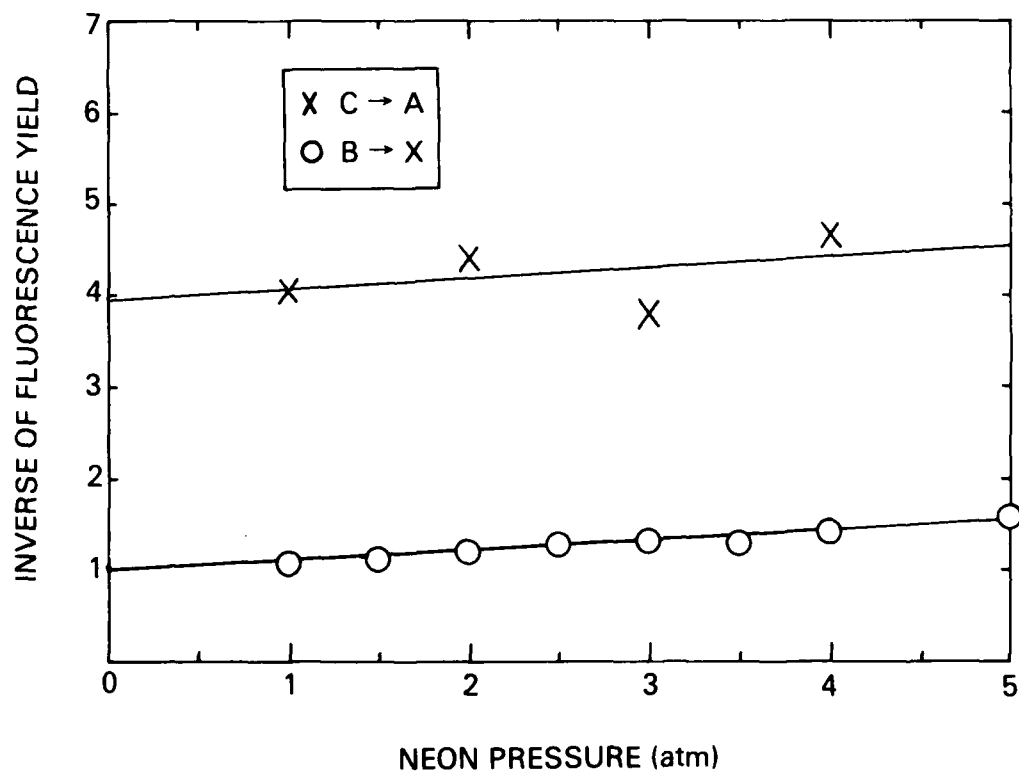


Figure 2. Inverse of fluorescence yields of the XeCl (B→X) and (C→A) transitions as a function of neon pressure. The data have been corrected for energy deposited in xenon. For the B state the zero-pressure intercept of unity indicates that its formation efficiency is approximately one XeCl (B) molecule for each neon excited species formed.

The role of the C state in the XeF laser

T. G. Finn,^{a)} L. J. Palumbo, and L. F. Champagne

Laser Physics Branch, Optical Sciences Division, Naval Research Laboratory, Washington, D.C. 20375

(Received 12 October 1978; accepted for publication 31 October 1978)

Ne/Xe/NF₃ mixtures were irradiated by a cold-cathode e-beam, and the fluorescence yields of the *B* and *C* states of XeF were measured as a function of neon pressure from 200 to 5300 Torr. At low neon pressures, the fluorescence yield of the *B* state corresponds to one photon emitted for each neon ion formed. As the neon pressure is increased the fluorescence yield of the *B* state decreases, but the ratio of the *C* emission to *B* emission approaches unity. If the *C* is formed through a channel which is independent of the *B* state, then the ultimate efficiency of the XeF laser is severely limited. However, analysis of the data with a XeF kinetics model indicates that the enhanced *C* emission results from two-body quenching of the *B* state by neon. We conclude that the XeF laser performance has been limited by other processes, namely, incomplete vibrational relaxation and ground-state bottlenecking.

PACS numbers: 42.55.Hq, 82.20.Wt, 33.50.Dq

XeF is the second rare-gas monohalide laser system (after KrF) to demonstrate high efficiency and output power. Initially, the XeF laser was operated in an argon diluent, but its efficiency was well below 1% because of transient

absorption in the medium. Champagne and Harris found a significant improvement in the output power and efficiency with neon as the diluent.¹ This work showed that the transient absorption present in pure neon, although comparable to that in pure argon, was markedly reduced by the addition of a small amount of xenon. Previously, we developed a com-

^{a)}Science Applications, Inc., Arlington, Va. 22202.

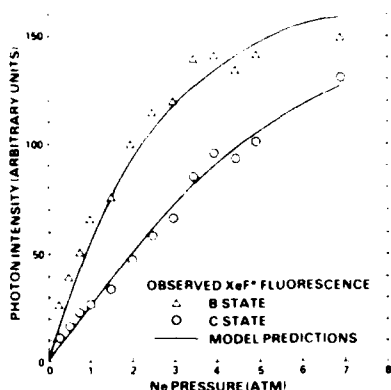


FIG. 1. Observed fluorescence of XeF $B \rightarrow X$ and $C \rightarrow A$ states with 6 Torr Xe and 2 Torr NF₃ as a function of neon pressure. The solid lines are the model calculations based on the formation efficiency and quenching rates given in the text.

puter model which simulates the kinetics in an electron beam-pumped XeF laser. Analysis with the model has shown that the addition of a small amount of xenon to pure neon significantly reduces the concentration of neutral species such as Ne* and Ne₂⁺ through the mechanisms of Penning and associative ionization, but only slightly diminishes the concentration of charged species.² Consequently, we have attributed the transient absorption in pure neon to the neutral species.

XeF has two intense emission features, the $B \rightarrow X$ system around 351 nm and the broad $C \rightarrow A$ system centered around 460 nm. Our kinetic model predicts that the formation efficiency of XeF* is high, but it cannot determine which states (B or C) are populated. Recently, Kligler *et al.*³ have shown that the C state of XeF lies 700 cm⁻¹ below the B state, and that the emission intensity of both states are equal under pumping conditions similar to those in the laser. The importance of the latter result is the following: if the C state is formed in such a way that its excitation energy is not channeled through the B state, then almost one-half the total excitation is lost. Thus, the maximum efficiency of the XeF laser would be approximately 5%, which is the value recently obtained by heating the mixture.⁴ If, on the other hand, the C state is formed through the B state, then all the excitation present in the C state is potentially extractable as laser radiation. To resolve this question and to characterize further the XeF laser, we have investigated the fluorescence from the B and C states and analyzed the results with a computer model.

The apparatus used in these experiments has been described previously and will be reviewed briefly.⁵ The kinetics chamber is made from aluminum and has an active volume of 1.5 × 1 × 20 cm³. The chamber is mounted directly to the electron-gun vacuum chamber with a thin titanium foil separating the two. The cold-cathode electron gun produces a beam of 280-keV electrons with a pulse duration of ~ 1 μsec. The peak current density into the laser gas is 2 A/cm². Fluorescence is observed perpendicular or parallel to the elec-

tron-beam direction with calibrated photodiodes and filters. All the kinetics experiments used concentrations of 6 Torr Xe and 2 Torr NF₃, which are the values corresponding to the optimum laser mixture. The dominant kinetic processes have characteristic times which are much shorter than the pulse duration, thus the excited and ionic species are in quasiequilibrium.

In Fig. 1, the XeF ($B \rightarrow X$) and ($C \rightarrow A$) fluorescence from a mixture of Ne/Xe/NF₃ is given as a function of neon pressure. At low neon pressure the ratio of $B \rightarrow X$ to $C \rightarrow A$ emission intensity is approximately 4 : 1. As the neon pressure increases, the fluorescence from both states increases, but at high pressures the $B \rightarrow X$ fluorescence begins to level off while the C fluorescence continues to rise. At the optimum laser mixture (5 atm) the $C \rightarrow A$ emission is over 70% of the $B \rightarrow X$ emission.

More information about the B and C states can be obtained by calculating their corresponding fluorescence yields. The fluorescence yield is defined here as the ratio of the number of photons emitted from a state divided by the number of ion-electron pairs produced by the electron beam. A fluorescence yield of unity corresponds to one photon emitted for each ion formed. It is possible for the total fluorescence yield to be greater than unity. For each 100 ions that are created, the electron beam also produces about 30 excited neutral atoms which can lead to the upper laser level.⁶

Relative fluorescence yields can be put on an absolute basis by normalizing to the absolute fluorescence yield of the N₂ second positive system produced in mixtures of argon with 5% nitrogen. At a total pressure of 2 atm, Huestis and Tang have determined the fluorescence yield of the second positive system to be approximately 9% over the e-beam current range 1–10 A/cm² incident to the active volume.⁶ Using the argon/nitrogen fluorescence as a secondary stan-

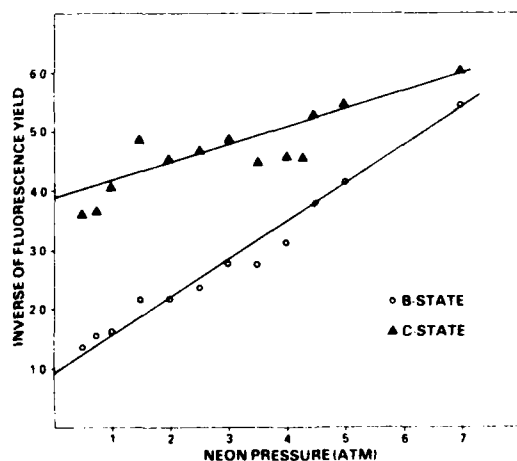


FIG. 2. Inverse of the fluorescence yields of the XeF ($B \rightarrow X$) and ($C \rightarrow A$) emissions as a function of neon pressure. For the B state the zero-pressure intercept of unity indicates that its formation efficiency is approximately one XeF (B) molecule for each neon ion formed.

TABLE I. Quenching rate constants used in model

Quenching reaction	Rate constant	Branching ratio to XeF(C)	Reference
XeF(B) + Ne	7.7×10^{-10} cm ³ /sec	0.95	11 and 12
+ 2Ne	2.7×10^{-10} cm ³ /sec	0.5 ^a	13
+ Ne + Xe	8.3×10^{-10} cm ³ /sec	0.5 ^a	13
+ Xe	1.1×10^{-10} cm ³ /sec	0.45	12
+ NF ₃	8.4×10^{-10} cm ³ /sec	0.64	11 and 12
XeF(C) + Ne + Xe	4.0×10^{-10} cm ³ /sec	Products	This work

^a Assumed for model calculations

dard, we obtained the absolute fluorescence yield of the XeF ($B \rightarrow X$) and ($C \rightarrow A$) transitions as a function of neon pressure. Since the thickness of the target gas is small compared to the penetration depth of the e-beam, the number of ions produced is linearly proportional to the gas pressure. Thus, the relative fluorescence yield is equal to the signal intensity divided by the neon pressure.

In Fig. 2 the inverse of the absolute fluorescence yield for the XeF transitions ($B \rightarrow X$) and ($C \rightarrow A$) is plotted versus neon pressure. This method of data analysis is similar to a Stern-Volmer plot and is useful in interpreting the data. Moreover, the fluorescence yields have been corrected to account for quenching by Xe and NF₃. This correction, which is largest in the low-pressure region, is about 10%. As can be seen in Fig. 2, at low neon pressure the fluorescence yield of the $B \rightarrow X$ transition approaches unity, which corresponds to a fluorescence energy efficiency of 10%. However, as the neon pressure is increased the fluorescence yield decreases, so that at the optimum laser mix of 5 atmospheres it is approximately 0.3. Meanwhile, the fluorescence yield of the $C \rightarrow A$ transition varies slowly and approaches 0.25 at zero pressure. There are two likely explanations for the pressure behavior of the fluorescence yields. First, at high pressure the formation efficiency of the B state is close to unity, but the state is quenched to the C state which lies 700 cm⁻¹ below it. Second, at high pressure, the excitation energy is intercepted before it reaches the B state and channeled directly into the C state. In the former case, almost all of the excitation can be considered as potential laser radiation because the energy can be extracted from the B state before it is quenched to the C state. However, in the latter case, the energy is directly pumped into the C state and is virtually inaccessible. Thus, the manner in which the C state is formed at high pressure determines the ultimate efficiency of the laser.

The C state can be formed in three ways: direct excitation, quenching from B to C by neutral species, and quenching from B to C by electrons. Our data indicates that electron mixing of the B and C states is not significant up to a pumping rate of 7 A/cm². This conclusion is based on the following results. First, as the NF₃ concentration in the kinetics chamber was varied from 2 to 100 Torr, we observed only a 10% decrease in the B/C emission ratio. Since the removal rate of the electrons, and thus their equilibrium concentration, is determined by the concentration of the attaching species, NF₃, the electron density varied greatly but the B -to- C

ratio remained approximately constant. Furthermore, other experiments were conducted in the laser mixture (5 atm) with 7-A/cm² e-beam pumping current, and the B -to- C ratio was found to be the same as in the kinetics experiments with 2-A/cm² pumping rate. Finally, if electron mixing were significant the B/C emission ratio should be much higher than is observed. The separation of the B and C states is 700 cm⁻¹, which is about 0.08 eV. If the electron temperature were 1 eV, the states would be approximately equally populated. Since the ratio of transition probabilities for the B and C states is approximately 7, the B -to- C emission ratio would be much greater than unity.¹⁴ Instead, the observed emission ratio extrapolates at high pressure to a value of 0.6, which corresponds to a temperature of 0.035 eV, close to the temperature of the background gas. Thus, electron mixing is not important in determining the ratio of the B and C states and a model based solely on neutral kinetics may be used.

The neutral kinetics model must include direct pumping to B and C , quenching from B to C and the reverse reactions, and quenching from B and C to products. For direct pumping the absolute fluorescence yields extrapolated to zero pressure were used. The quenching rate constants used in the model are given in Table I. The applicability of the rates will be discussed later. The predictions of the model based on absolute fluorescence yields and quenching by neutrals are given as the solid lines in Fig. 1. As can be seen from Fig. 1, the model is in good agreement with the data. Quenching of the B state, primarily through two-body collisions with neon, accounts for all the observed decrease in the fluorescence yield as the neon pressure is increased. If significant interception of the B state were present, the model values would be much higher than the observed B emission. Moreover, if at high pressure a larger fraction of the excitation were channeled directly into the C state, the model predictions for the C emission would be much less than the observed values. Initially, however, the predicted C emission was higher than the observed value, indicating that some quenching of the C state by the background gas occurs. The C -state quenching rate which fits the data is given in Table I.

Three important conclusions can immediately be drawn from the model analysis. First, almost 80% of the ions and electronically excited neutrals formed channel their excitation directly into the B state. Second, the back reaction, C to B , is small, such that once the energy is in the C state it is virtually lost. Third, the enhanced C emission at high pressure is due to quenching from B to C , primarily

through two-body collisions with neon. In fact, two-thirds of the *C* population results from the *B* state. The last conclusion has been verified experimentally. Since a large fraction of the *C*-state population results from the *B* state, the *C* emission rate will decrease if the steady-state *B* population is decreased as occurs in a saturating laser field. The depression of the *C* emission in a saturating laser field has been observed.¹⁰

The accuracy of the model predictions depends on the reliability of the rate constants used. Over 50% of the *B*-state quenching is due to two-body neon quenching, a process whose rate constant and branching are well characterized.^{11,12} However, 40% of the quenching is due to three-body neon and neon plus xenon reactions. The rate constants for these processes have been derived from electron-beam-pumped mixtures, and, strictly speaking, the rates could correspond to interception rather than quenching processes. That is, these reactions could channel excitation away from the *B* state rather than quench the *B* state. In order to characterize the XeF laser precisely the quenching rate constants and branching ratios for these processes have to be known.

Assuming the reliability of the quenching rate constants, we can summarize the results and conclusions:

(a) The formation efficiency of the *B* state is approximately one XeF (*B*) molecule formed for each ion pair created.

(b) The decrease in the *B*-state fluorescence yield observed at high pressure is due to quenching, primarily through two-body collisions with neon.

(c) The enhanced *C* emission observed at high pressure is due to quenching from *B* to *C* rather than interception of the *B* state.

(d) Since the formation efficiency of XeF (*B*) is high, other processes are limiting the laser performance. Most likely, these processes are incomplete vibrational relaxation and bottlenecking of the state due to finite relaxation rates.

The authors wish to thank W. T. Whitney for lending us his electron-beam apparatus, D. Shores for his technical assistance, and D. Huestis, SRI, and K. Tang, Maxwell Labs. Inc., for making available to us their unpublished data.

- L. F. Champagne and N. W. Harris, Appl. Phys. Lett. **31**, 513 (1977)
- T. G. Finn, L. J. Palumbo, and L. F. Champagne, Appl. Phys. Lett. **33**, 148 (1978)
- D. Kligler, H. H. Nakano, D. L. Huestis, W. K. Bischel, R. M. Hill, and C. K. Rhodes, Appl. Phys. Lett. **3**, 39 (1978)
- L. F. Champagne (unpublished)
- J. Hsia, J. A. Mangano, J. H. Jacob, and M. Rokni, Appl. Phys. Lett. (to be published)
- N. W. Harris, F. O'Neill, and W. T. Whitney, Appl. Phys. Lett. **25**, 148 (1974)
- L. R. Peterson and J. E. Allen, Jr., J. Chem. Phys. **56**, 6068 (1972)
- D. L. Huestis, R. M. Hill, D. J. Eckstrom, M. V. McCusker, D. C. Lorents, H. H. Nakano, B. E. Perry, J. A. Margevicius, and N. E. Schlotter, Stanford Research Institute International Report No. MP 78-07, 1978 (unpublished)
- R. W. Waynant and J. G. Eden, J. Quantum Electron. (to be published)
- L. F. Champagne (unpublished)
- J. G. Eden and R. W. Waynant, Opt. Lett. **2**, 13 (1978)
- H. C. Brashears, Jr. and D. W. Setser, Appl. Phys. Lett. **33**, 821 (1978)
- M. Rokni, J. H. Jacob, J. A. Mangano, and R. Brocher, Appl. Phys. Lett. **32**, 223 (1978)

COMPUTER MODELING

Introduction

The general purpose computer code for modeling e-beam pumped and e-beam sustained rare-gas halide lasers has undergone more evolution during this past fiscal year. A description of the code and examples of its applications to e-beam sustained KrF and XeF lasers have been published¹ in FY 79. The code, as described in that publication, kept track of electron kinetics in a spatially-uniform applied electric field by solving the Boltzmann transport equation. This version neglected the initial energy distribution of secondary electrons created by the high energy electron beam. Such an approximation is valid as long as the energy deposited into the laser medium by the e-beam is small compared to that deposited by the applied field. Detailed studies of electron kinetics in e-beam sustained discharge-pumped RGH lasers have been carried out and the results were presented² early in FY 79. The abstract pertaining to this presentation can be found in Appendix I.

RGH Computer Code Development for the XeCl Laser - Secondary Electron Kinetics

In laser media in which the energy distribution function of the secondary electrons created by the e-beam is an important controlling factor, and especially in those cases where the applied electric field is weak or zero, it is useful to have a way of computing the electron energy distribution function.

A need to know the distribution of electron energies arises when one attempts to model the e-beam pumped XeCl laser. In contrast to RGH lasers studied previously (KrF and XeF), there are several important processes in the XeCl system having rates which are sensitive functions of average electron energy and energy distribution. Some examples are: (a) dissociative electron attachment to HCl which has a threshold of 0.8 eV for $v = 0$ and 0.5 eV for $v = 1$; (b) dissociative electron-ion recombination which varies rapidly with electron temperature, T_e , especially at $T_e < 0.2$ eV; and (c) electron mixing of the vibrational levels of HCl. Also, it has been proposed to derive some reaction rates, or at least their relative importance in typical XeCl laser gas mixtures, by fitting a model to short pulse e-beam pumped kinetics experiments. In these experiments, the pump pulse current density is several hundred A/cm² and its duration is ~ 3 ns. The rise and fall of XeCl* fluorescence is observed out to ~ 100 -200 ns into the afterglow. Proper modeling of these data depends upon a knowledge of the time dependence of the electron energy distribution.

Thus, a capability for keeping track of electron energies was developed and incorporated into the RGH computer code. Essentially, this capability consists of a set of subroutines which divide the electrons into energy cells (typically ~ 40 cells, each of ~ 0.5 eV width) and compute the flow rates of electrons from one cell into another by solving appropriate first-order differential equations. Additional subroutines set up the energy grid and the system of differential equations and provide several forms of diagnostic output. The differential equations for the electrons are merged with those for the heavy particles

and all are solved as a single system of coupled linear ordinary differential equations using a Runge-Kutta-Treanor³ integrator. The electron velocity distribution is assumed to be isotropic since there is no applied electric field. The user supplies a table of cross sections, $\sigma(u)$, or a source function, $S(u)$, (where u is the electron energy) for each electron-impact reaction.

I. Electron Kinetics Algorithm

The procedure for computing the time evolution of the populations, N_i , of electrons in each energy cell, i ($1 \leq i \leq i_{\max}$, where i_{\max} is the total number of cells considered), consists of solving the differential equations for dN_i/dt . These equations are of the form

$$\frac{dN_i}{dt} = \sum_{p,n} \dot{N}_{in}^p,$$

where \dot{N}_{in}^p represents the contribution to dN_i/dt from the process of type p involving a heavy particle of species n . The types of electron-impact process allowed for in the present model are: (a) momentum transfer, (b) external sources of electrons, (c) Penning and associative ionization, (d) inelastic collisions, (e) superelastic collisions, (f) ionization, (g) recombination and attachment, and (h) electron-electron collisions.

For momentum transfer collisions, cell i gains electrons from cell $i + 1$ and loses electrons to cell $i - 1$; thus,

$$\dot{N}_{in}^{mt} = N_n N_{i+1} \left(\frac{2m_e}{M_n} \right) \left(\frac{u_{i+1}}{\Delta u} \right) \sigma_{i+1,n}^{mt} v_{i+1}$$

$$-N_n N_i \left(\frac{2m_e}{M_n} \right) \left(\frac{u_i}{\Delta u} \right) \sigma_{i,n}^{mt} v_i ,$$

where N_n and M_n are, respectively the number density and mass of heavy particles of species n , m_e is the electron mass, and u_i is the average energy of electrons in cell i [$u_i = (i - \frac{1}{2}) \Delta u$, where Δu is the energy grid mesh size]. The mean velocity, v_i , of electrons in cell i is given by

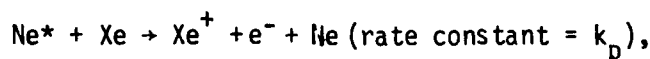
$$v_i = (2\varepsilon u_i/m_e)^{1/2},$$

where $\varepsilon = 1.602 \times 10^{-12}$ ergs eV^{-1} , and $\sigma_{i,n}^{mt}$ is the momentum transfer cross section at a relative collision energy of u_i . Physically speaking, the quantity $[(2m_e/M_n) (u_i/\Delta u)]^{-1}$ is the number of momentum transfer collisions the electron must undergo to lose an amount of energy equal to Δu .

In the cases of external pump sources and chemionization, electrons are created by processes not involving electrons as reactants. Hence, one must supply an external source function, $S^{\text{ext}}(u)$ and a rate constant, k_{ext} to describe the contributions of these reactions. The contributions to dN_i/dt by these processes are of the form,

$$\dot{N}_{in}^{\text{ext}} = R_n^{\text{ext}} S^{\text{ext}}(u_i)$$

where R_n^{ext} is the reaction rate of process n which, is given (e.g.) for the Penning ionization reaction,



by $R_n^{\text{ext}} = [\text{Ne}^*] [\text{Xe}] k_p$ and $S^{\text{ext}}(u_i)$ is normalized by the code such that $\sum_i S^{\text{ext}}(u_i) = 1$. For Penning and associative ionization, S^{ext} approximates a delta function which peaks at an energy equal to the exoergicity of the reaction while for an external pump source, S^{ext} may be broad and smooth.

An inelastic collision results in the jump of an electron from cell $i + j$ into cell i or in the loss of an electron from cell i by a jump into cell $i - j$ (where $j\Delta u$ is the transition energy). Hence,

$$\dot{N}_{in}^{\text{inel}} = N_n N_{i+j} \sigma_{i+j,n}^{\text{inel}} v_{i+j} - N_n N_i \sigma_{i,n}^{\text{inel}} v_i .$$

Similarly, the reverse (superelastic) process affects the population of cell i according to

$$\dot{N}_{in}^{\text{supr}} = N_n N_{i-j} \sigma_{i-j,n}^{\text{supr}} v_{i-j} - N_n N_i \sigma_{i,n}^{\text{supr}} v_i .$$

Ionizing collisions are similar to inelastic collisions as far as the incident electron is concerned; however, an additional electron is created. For simplicity, this electron is assumed to be created in the lowest energy cell. Thus, the contribution to dN_i/dt by electron-impact ionization is

$$\dot{N}_{in}^{\text{ion}} = N_n N_{i+j} \sigma_{i+j,n}^{\text{ion}} v_{i+j} - N_n N_i \sigma_{i,n}^{\text{ion}} v_i$$

and an additional term is included for the first cell viz.,

$$\dot{N}_{1n}^{\text{ion}} = \sum_i \dot{N}_{in}^{\text{ion}} .$$

For ionizing collisions, j is defined as $j = (\text{I.P.}/\Delta u) + 1$ (I.P. is the ionization potential). This definition allows energy conservation while

accounting for the energy of the electron created in cell 1.

Recombination and attachment involve the loss of electrons from cell i at a rate given by

$$\dot{N}_{in}^{rec} = -N_n N_i \sigma_{i,n}^{rec} v_i.$$

Finally, the electron-electron collision term is estimated by

$$\dot{N}_{in}^{ee} = (N_i^{Max} - N_i) \tau_{ee}^{-1},$$

where N_i^{Max} is the number of electrons in cell i for a Maxwellian distribution with the same average electron energy as the actual distribution and τ_{ee} is the electron-electron equipartition time.⁴ The average energy, \bar{u} , and τ_{ee} are given by

$$\bar{u} = N_e^{-1} \sum_i N_i u_i$$

and

$$\tau_{ee} = \frac{3.4 \times 10^5 (2\bar{u}/3)^{3/2}}{N_e \log_e \Lambda} \quad (\text{sec}),$$

where N_e is the total electron density in cm^{-3} , u and \bar{u} are in eV, and $\log_e \Lambda$ is the (slowly varying) Coulomb logarithm given by

$$\log_e \Lambda = 23 - \log_e [N_e^{1/2} (2\bar{u}/3)^{-3/2}].$$

The Maxwellian population is computed from

$$N_i^{Max} = C \int_{u_i - \Delta u/2}^{u_i + \Delta u/2} u^{1/2} \exp(-3u/2\bar{u}) du$$

where C is a normalizing constant which ensures that

$$\sum_i N_i^{\text{Max}} = \sum_i N_i = N_e.$$

This formulation for electron-electron collisions insures number density and energy conservation.

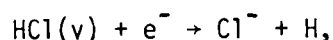
The cross sections, $\sigma_{i,n}^{\text{mt}}$, $\sigma_{i,n}^{\text{inel}}$, $\sigma_{i,n}^{\text{supr}}$, $\sigma_{i,n}^{\text{ion}}$, and $\sigma_{i,n}^{\text{rec}}$, and the source functions S^{ext} are supplied by the user for arbitrary energies and are interpolated onto the working computational grid by the code. Other data also required are M_n , energy losses for inelastic and ionizing collisions, and energy gains for superelastic collisions.

II. Results of Secondary Electron Kinetics Modeling

The algorithm described above has been used to expand the capabilities of the RGH laser code to include the effects of the secondary electron energy distribution on the reaction rates. Modeling has been done for long pulse e-beam pumping of Ne/Xe/HCl mixtures. Results for a mixture of 3000 Torr Ne, 30 Torr Xe, 2 Torr HCl pumped by a 300 keV, 600 ns, 7 A/cm^2 e-beam are shown in Fig. 1. The curve for \bar{u} shows that the average electron energy remains in the 2-3 eV range throughout the pulse. This value is determined by a balance between heating and cooling processes.

Under conditions of Fig. 1, the main electron heating process is the direct creation of hot secondary electrons from the ionization of neutral neon by the e-beam. These secondary electrons have an average energy of 8.3 eV because the source function for this process is assumed to be constant from zero to the excitation energy of Ne^* (16.6 eV) and

zero for the higher energies. An additional positive contribution to the electron temperature comes from rapid dissociative electron attachment to vibrationally excited HCl,



which accounts for the loss of more than 90% of all electrons. By selectively removing low energy electrons, this process raises the average energy of the remaining electrons. The electrons are cooled mainly by the momentum transfer collisions with the background gas (Ne) and by inelastic and ionizing collisions with ground state Xe. Throughout the pulse, the electron-electron equilibration time, τ_{ee} , is ≤ 1 ns so that the electron energy distribution function is approximately Maxwellian.

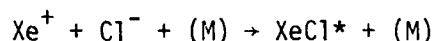
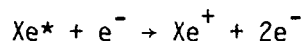
These calculations show that for typical long-pulse XeCl laser conditions, the average electron energy is high enough such that electron-ion dissociative recombination rate coefficients and dissociative attachment rate coefficients vary slowly,

Other interesting processes which have been shown to be significant by the secondary electron kinetics modeling described here are multi-step excitation and ionization of Xe by electron impact. For example:

- (a) $\text{Xe} + e^- \rightarrow \text{Xe}^* + e^-$,
- (b) $\text{Xe}^* + e^- \rightarrow \text{Xe}^{**} + e^-$,
- (c) $\text{Xe}^* \text{ (or } \text{Xe}^{**}) + e^- \rightarrow \text{Xe}^+ + 2e^-$.

For the conditions of Fig. 1, reaction (b) accounts for the loss of

~ 25% of Xe*. Reactions such as these and most other electron impact reactions involving thresholds greater than a fraction of an eV cannot be properly treated unless one keeps track of electron kinetics. Indeed, for most e-beam pumped RGH models done in the past, these reactions have been either crudely estimated or neglected altogether. Electron impact ionization of Xe* is important to consider because it provides an alternate route for forming XeCl* from Xe*, namely:



Further analysis on the role of secondary electron kinetics in the XeCl laser are underway.

References

1. T. H. Johnson, L. J. Palumbo and A. M. Hunter, "Kinetics Simulation of High-Power Gas Lasers," IEEE J. Quantum Electron., QE-15, 289-301 (May 1979).
2. L. J. Palumbo, "The Role of Electron Kinetics in Discharge-Pumped Rare-Gas Halide Lasers," Paper E-2, 31st Annual Gaseous Electronics Conference, Buffalo, NY (17 October 1978).
3. C. E. Treanor, "A Method for the Numerical Integration of Coupled First-Order Differential Equations with Greatly Different Time Constants," Math. Comput., 20, 39-45, 1966.
4. D. L. Book and A. W. Ali, "A Collection of Plasma Physics Formulas and Data," NRL Memorandum Report 2898 (January 1975).

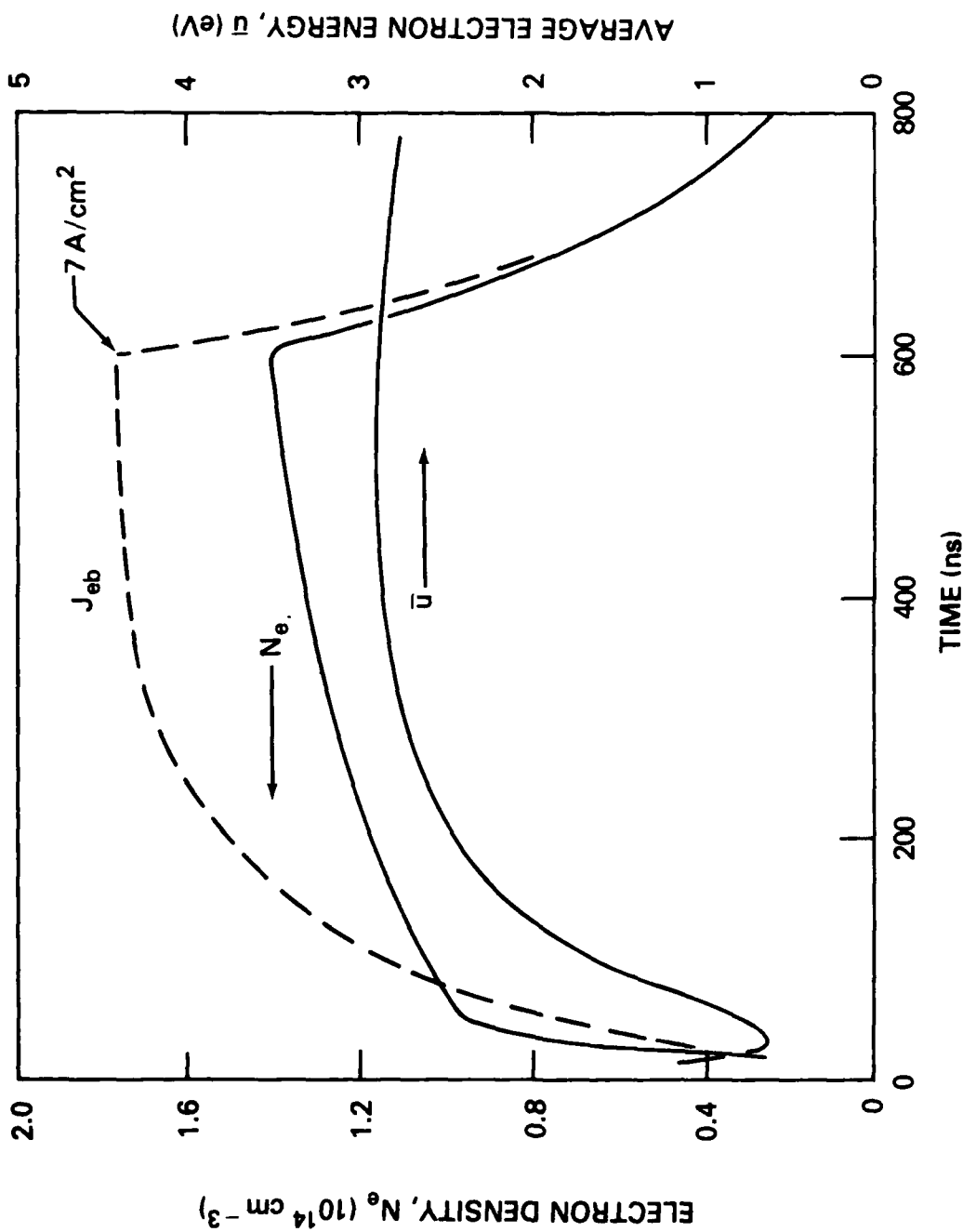


Fig. 1. Computed time histories of electron density, N_e , and average electron energy, \bar{u} , for a mixture of Ne/Xe/HCl = 3000/30/2 (Torr) pumped by a 300 keV e-beam. The pump pulse current density, J_{eb} , is shown by the dashed curve and has a peak value of 7 A/cm² incident to the gas. The results are for a uniformly pumped optically thin volume with no laser mirrors and hence no stimulated emission.

Kinetics Simulation of High-Power Gas Lasers

Numerical simulation of high-power gas lasers requires the integration of a variety of numerical techniques; simultaneous solutions must be obtained to a large set of ordinary differential equations, and several nonlinear partial differential equations. A family of codes employing similar methods has been devised and has demonstrated remarkable success in predicting laser performance over a broad range of parameters. We describe here the appropriate techniques for dealing with gas kinetic equations, the steady-state Boltzmann equation, and physical optics. Modeling of both e-beam pumped and e-beam sustained discharge-pumped lasers is described; complex electron kinetic processes are included. Results are shown for both krypton-fluoride and xenon-fluoride lasers.

Kinetics Simulation of High-Power Gas Lasers

THOMAS H. JOHNSON, LOUIS J. PALUMBO, AND ALLEN M. HUNTER, II

Abstract—Numerical simulation of high-power gas lasers requires the integration of a variety of numerical techniques; simultaneous solutions must be obtained to a large set of ordinary differential equations, and several nonlinear partial differential equations. A family of codes employing similar methods has been devised and has demonstrated remarkable success in predicting laser performance over a broad range of parameters. We describe here the appropriate techniques for dealing with gas kinetic equations, the steady-state Boltzmann equation, and physical optics. Modeling of both *e*-beam pumped and *e*-beam sustained discharge-pumped lasers is described; complex electron kinetic processes are included. Results are shown for both krypton-fluoride and xenon-fluoride lasers.

I. INTRODUCTION

DURING the past decade, numerical simulation models for gas lasers have been developed to predict, with good reliability, the gross performance of gas lasers operating at infrared wavelengths. In moderately complex kinetic systems such as those of the CO₂ electric discharge laser [1], the CO electric discharge laser [2], and the DF-CO₂ transfer laser [3], it has been possible to predict total power and efficiency with some confidence. More detailed quantities have often eluded accurate prediction, usually because of uncertainties in fundamental kinetic processes. The results from these kinetics codes have been coupled with other techniques—hydrodynamic models (especially for simulation of the gasdynamic laser) and both geometric and physical optics models—to produce successful simulations of laser systems.

With the advent, in the early 1970's, of gas lasers operating at much shorter wavelengths—in the visible and near ultraviolet—it became necessary to develop new computational models. The kinetic processes of such systems are vastly more complicated than those of CO₂ lasers, for example. This complication is both quantitative and qualitative. There are a great many more reactions, and *kinds* of reactions, which must be accounted for and balanced properly before one can simulate a real experiment. And, more significantly, the assumptions of (at least approximate) local thermodynamic equilibrium made by earlier simulations are clearly not valid in the new lasers. (In CO₂ modeling, for example, it is common practice to as-

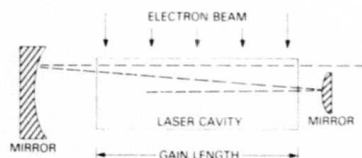


Fig. 1. Example of direct-pumped laser geometry: The typical apparatus modeled here is simpler in form. Discharge sustainer voltage may be applied, e.g., into the page.

sume the vibrational modes to be individually equilibrated.) It becomes necessary, then, to update certain elastic and inelastic collision parameters through solution of a Boltzmann equation in concert with the solution of the gas kinetics equations.

The techniques presented here were assembled for the simulation of a particular pair of rare-gas-halide molecular lasers, the excimers krypton-fluoride (KrF), operating at 2485 Å, and xenon-fluoride (XeF), operating at 3532 Å. Where it is useful to illustrate by example, these systems will be used; and the results presented will involve simulations of laboratory experiments with these lasers. The methods are, however, quite general, and may be used with equal success on a great variety of complex systems. In fact, the techniques have been specialized along quite different lines by two of the authors, using two quite different computers (CDC 7600 and Texas Instruments ASC); where different methods have been used to model specific aspects of the systems, both will be described here. Over rather a broad realm, one's choice of numerical methods represents, as much as anything else, one's aesthetic perceptions.

Physical Approximations

Energy is generally delivered most efficiently to the gases in these electronic-transition lasers through collisions with energetic electrons, either through direct pumping with electron beams or by application of an electric discharge (usually sustained by an *e*-beam). The essentials of the geometry for a direct-pumped laser are shown in Fig. 1. The arrangement shown is for an unstable confocal resonator as used in the KrF physical optics calculations (see Section II).

For an *e*-beam sustained discharge, the essentials of Fig. 1 remain correct. A discharge voltage is added in the third dimension (into the page), and the resulting current carried by secondary electrons (ionizations caused by the *e*-beam) pumps energy into the gas collisionally.

Manuscript received January 15, 1979. This work was supported in part by DARPA.

T. H. Johnson is with the United States Military Academy, West Point, NY 10996.

L. J. Palumbo is with the Laser Physics Branch, Optical Sciences Division, Naval Research Laboratory, Washington, DC 20375.

A. M. Hunter is with the Department of Physics, Air Force Institute of Technology, Wright-Patterson Air Force Base, OH 45433.

U.S. Government work not protected by U.S. copyright

Note that, as far as the energetics are concerned, the problem may be treated in levels of approximation varying from zero dimensional to three dimensional. One may, for example, attempt to model the spatial and temporal anisotropies of energy deposition by the electron beam, which depend almost entirely upon the characteristics of the particular electron gun being used, or one may presume that the beam energy is deposited uniformly throughout the cavity. Similarly, if the laser is discharge pumped, one may choose to model the spatial asymmetries of discharge current (which also depend on the e -beam deposition anisotropies); or, again, one may ignore these. All models presented here make the simplest assumptions in both these cases, reducing the dimensionality to zero. Since both deposition anisotropies and discharge current asymmetries tend to degrade laser performance, the simulations will present a best-case prediction of performance. If energy deposition in a particular experiment is particularly poor because of any combination of these problems, an accurate simulation can be produced by tailoring the code's modeling of e -beam energy deposition to that actually measured, rather than that of a nominal ideal beam at the rated input current.

Temporal variations in the discharge voltage are modeled in these simulations, as discussed in Section III.

Variations along the laser beam axis can arise for a number of reasons, including all the above sources, longitudinal variations in flux level (especially those caused by using an unstable resonator, as in Fig. 1), variations in absorption, or other media interactions. The simplest forms of these simulation models also ignore all these variations as well. The resonator is presumed to be a simple Fabry-Perot resonator, so that the optical field is approximated as uniform in amplitude. The chemical concentrations everywhere in the cavity are then identical, and a simple uniform-gain approximation can be made (Section II). This zero-dimensional calculation can produce highly accurate results for overall energy, intensity, and efficiency, as well as reliable performance parameters for various modes of operation. One- and two-dimensional calculations can be performed by dividing the cavity into an appropriate number of cells and applying the kinetics procedure to the updating of small-signal gain in each cell; intensity must then be calculated by a more detailed modeling of the radiation field. Techniques for doing this are discussed in Section II.

II. KINETICS AND RADIATION

Electronic transition gas lasers generally involve complex, branching chains of energy flow from initial pump excitation of background gas to eventual extraction of laser radiation. These energy chains include processes such as: energy deposition by electron ionization and excitation; energy transfer by various collisional mechanisms, including neutralization, displacement and "harpooning," leading to formation of the upper laser level; and collisional mechanisms which intercept excitation energy before it can reach the upper laser level, or which quench that level before stimulated emission occurs. Also, one must consider extraction of stimulated emission, including absorptions by various process in the gas and reso-

nant reabsorption by the lower laser level (if there is one), laser cavity oscillation, and coupling through output mirrors. A time-dependent model of the kinetics of such a system must define and update species densities for a large number—typically between twenty and sixty—gas components, including ground states, several excited states and ions of atoms and molecules, plus electrons and photons.

The time evolution of these components is followed by the solution of a set of coupled first-order ordinary differential equations—one for each gas component. To the set of equations defining species densities are added further differential equations describing the evolution of the photon field, the gas temperature, and (in some models) coupled electrical circuit parameters. The species equations can be generally described as equating the rate of change of species density to a sum of contributing formation terms less a sum of depletion terms, viz.,

$$\frac{dN_i}{dt} = \sum_j F_{ji} - \sum_k D_{ik}. \quad (1)$$

Here N_i is a particular species density, the F 's are the formation terms, and the D 's the depletion terms. For example, consider a simple chemical reaction of the form $A + B \rightarrow C + D$, whose forward rate is characterized by a rate constant k ; if the species densities are expressed in cm^{-3} , the units of k are cm^3/s (a unit of "particles" or molecules being understood in the numerator of the former and the denominator of the latter). For this reaction, the rate equations defining species C and D would contain the formation term

$$F = k[A][B];$$

at the same time, the equations defining species A and B would contain the depletion term

$$D = k[A][B].$$

It has been found to be highly useful to code the equations to the greatest extent possible in symbolic format. The equations themselves are specified in an input data list in chemical reaction format, with the appropriate reactants and products expressed as symbolic names. The rate constants are included in this list, along with flags specifying the conditions of their definition and sequence and source information. Some of the rate constants must be updated during the computation, being functions of gas temperature or electron energy distribution. The differential equations of the form of (1) are then generated internally by the computer code. This method not only makes it much easier to alter the set of equations (by addition or deletion of terms or reactions, or by change of reaction rates), it also greatly reduces errors attendant to such alterations, errors which arise with remarkable, almost spontaneous, ease in the complex tangle of reactions. Further, symbolic manipulation makes the definition and computation of a variety of output and diagnostic quantities much easier. Finally, it makes a single code the easily adaptable basis for simulation of a wide variety of laser systems and chemical kinetics experiments: the entire composition of the simulated gas may be changed without

altering the code itself. Experience has shown that an adequate symbolic system is one which employs names of up to six alphanumeric characters and defines reactions with up to four reactants and five products each.

Integration Schemes

Several different integration schemes for the chemical kinetics equations have been used successfully with these techniques in simulating KrF and XeF lasers. The reaction rates in these systems may vary by ten orders of magnitude or more, as may species concentrations. However, it has not been found to be necessary to employ any of the more sophisticated techniques developed to solve nonlinear sets of "stiff" equations. This is a result of the physical system itself. Most of the species densities rise extremely steeply in the first tenth of the simulation time, requiring that the fastest rates define timesteps; later in the pulse, species densities tend to flatten out together, permitting quite long timesteps for all species, regardless of rate constant.

Simulations on the ASC computer have used a fourth-order Runge-Kutta-Treanor [4] algorithm, which provides for stiff systems. Both upper and lower limits to timestep size are user-specified through maximum limits on changes in the N_i or dN_i/dt . Limits of 5 percent change per timestep have been found to be sufficient for accuracy. Integrations requiring a few thousand timesteps (for a 1–2 μ s laser pulse) for systems of 30 species and 100 reactions take about 10 s of CP time.

The CDC 7600 versions of these simulations have also been run with a fourth-order predictor-corrector Hamming's method. However, detailed comparisons of simulation of KrF experiments using both Hamming's method and a far simpler modified-Newton's method integrator have shown the latter to be fully as accurate when used with a restrictive flux limiter on N_i and dN_i/dt ; the few extra integrations required for accuracy are more than compensated by the increased speed per timestep. The flux limiter has two steps. Assuming that a standard timestep DT has been set (or calculated as the remaining time in a longer edit interval), first calculate

$$(\Delta T_i)_1 = \text{abs} \left(\frac{f_1 \cdot N_i + 100}{(dN_i/dt) + 10^{-100}} \right) \quad (2)$$

where f_1 is an arbitrarily chosen fraction (usually 0.05, as above). The extra numbers in numerator and denominator are obviously to prevent zeros from fouling the calculation. (Compared to all real N_i , 100 is a very small number.) Then compare DT to $(\Delta T_i)_1 \cdot f_2$ for all species, where f_2 is another user-specified fraction; if DT is smaller than each of these, it remains the timestep. For N_i for which DT is larger, calculate

$$(\Delta T_i)_2 = \text{abs} \left(\frac{\Delta N_i + 10^{-90}}{\Delta(dN_i/dt) + 10^{-100}} \right) \quad (3)$$

where ΔN_i is the change in N_i over the last timestep, and $\Delta(dN_i/dt)$ the change in formation/depletion rate over the last timestep. DT is then reset as the smaller of $(\Delta T_i)_1$ and $(\Delta T_i)_2$. Using this flux limiter, the modified-Newton's method integrator performs the benchmark integration just described in about 4 s of CDC 7600 time.

Electron-Beam Pumping

In electronic transition lasers, the first step in the kinetics chain leading to extraction of laser energy is the deposition of energy in the diluent gas by either photons or electrons; in high-power lasers, electron-beam pumping is usually chosen in preference to flashlamps. Relativistic electrons deposit energy as ionization and direct excitation; calculation of the rates of these reactions can be done a variety of ways. In one of the applications reported here, the stopping power calculations of Berger and Seltzer [5] were used. It is necessary to modify these calculations by a numerical factor (typically between 2 and 3) to account for the zigzag path the electrons follow through the gas. Calculations by Hunter [6] have correlated existing experimental data to provide this multiplicative factor as a function of beam energy. The other application used results of a detailed electron transport code [7], [8] which accounts for the beam's path deviations and allows for losses of incident electrons to backscattering.

Whichever method is used, the ionization and excitation rates are calculated initially (either by hand or in the initial executive portion of the code) to correlate to the specific e -beam energy desired. They are then supplied directly as loss and gain terms in the rate equations for the species gaining or losing in number density multiplied by an input-specified constant for the e -beam current density. This multiplier can also be defined as a function of time to allow for real variations in e -beam current. So, for example, the F terms [(1)] for ionic species would include contributions from the beam, as would the F terms for excited states. About three times more ions than metastables are created directly by the e -beam.

Obviously, this method is also appropriate for optically excited media, with appropriate redefinition of constants.

Lasing, Fluorescence, and Absorption

Production of radiation in the laser cavity is treated by a uniform gain approximation. This approximation is generally good when the laser is operating at or near saturation and when there are no major nonuniformities of lasing states in the medium. For situations in which the gain cannot be approximated as uniform throughout the cavity, one- or two-dimensional optics codes (discussed later in this section) must be coupled into the kinetics solution.

The differential equation defining the rate of change of intracavity laser intensity is

$$\frac{dI_L}{dt} = cI_L(\alpha - \alpha_{th}) \quad (4)$$

where I_L is the intensity in W/cm^2 , α is the net gain, and α_{th} is the threshold gain, the gain needed to overcome round-trip mirror losses. These are defined as

$$\alpha = \sigma_{se}(N_{ul} - N_{ll}) - \sum_n (\sigma_{ab})_n N_n \quad (5)$$

$$\alpha_{th} = -\frac{1}{2l_c} \ln(R_1 R_2) \quad (6)$$

The term $\sigma_{se}(N_{ul} - N_{ll})$ is the small-signal gain, in which N_{ul} and N_{ll} are the number densities of the upper and lower laser levels, respectively, and σ_{se} is the stimulated emission cross section, defined

$$\sigma_{se} = \left(\frac{\lambda^2}{8\pi\tau_s} \right) \left(\frac{2}{\pi\Delta\nu} \right), \quad (7)$$

in which λ and ν are the wavelength and frequency at line center, τ_s is the spontaneous lifetime of the upper laser level, and $\Delta\nu$ is the spontaneous linewidth at half maximum. The remaining terms are: $(\sigma_{ab})_n$ and N_n are the photoabsorption cross sections and number densities of species n ; l_c is the cavity length (distance between mirrors); and R_1 and R_2 are the mirror reflectivities.

The spontaneous emission term is calculated as

$$\frac{dI_s}{dt} = \frac{N_{ul}}{\tau_s} (h\nu), \quad (8)$$

where $h\nu$ is the laser photon energy. Most of the spontaneous emission is lost as sidelight fluorescence. The small fraction directed within the effective laser solid angle is added to the right-hand side of (4); this fraction is typically about 10^{-5} – 10^{-6} . The remainder is discarded in the calculation of the laser flux, but is accounted for in determining energy lost by side fluorescence.

After the intracavity intensity has been updated, the instantaneous output intensity is given by

$$I_o = I_L \left(\frac{1 - R_1 R_2}{1 + R_1 R_2} \right). \quad (9)$$

The denominator in this equation arises from considering both left and right traveling waves. The total laser energy radiated is simply calculated as

$$E_L = \int_0^{t_p} I_o dt \quad (10)$$

where t_p is the total pulse length.

Physical Optics Simulation

Optical resonator computations are performed using a Fourier optics propagation algorithm developed by Salvi [9]. The details of the optics theory are discussed in [10] and [11]. For computational purposes the laser cavity is represented by a series of discrete optical elements oriented transverse to the optical axis as shown in Fig. 2. Two of these, M_1 and M_2 , are the mirrors of a positive branch confocal unstable cylindrical strip resonator. The elements S_i between the mirrors are gain sheets. The amplification and phase transformation that the electric field experiences in propagating through a gain region of thickness Δz is accounted for in one operation at each gain sheet. The thickness Δz is kept sufficiently small that the average intensity within a gain region is approximated well by $(I_i^+ / g \Delta z) [e^{g \Delta z} - 1]$. The intensity entering gain region i from the left is I_i^+ . The corresponding intensity entering from the right is I_i^- .

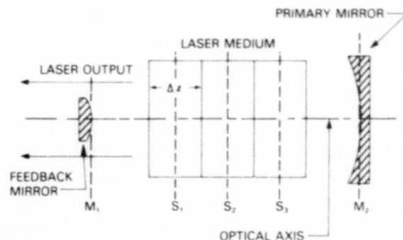


Fig. 2. Zoning for optical resonator computations.

The electric field is computed for N points at each optical element. These points are equally spaced so that a fast Fourier transform (FFT) can be used to perform the required discrete Fourier transforms. The optical coordinate system expands with the geometrical optical rays so that each element is resolved equally well with N points. The electric field is represented as a linear combination of plane waves

$$U_i(x) = \int_{-\infty}^{\infty} A_i(f_x) \exp [i2\pi f_x x] df_x. \quad (11)$$

The Fourier spectrum is propagated analytically from one optical element to the next by the transfer function $H_i(f_x, \Delta z_i)$

$$H_i(f_x) = e^{ikz} \exp -i\pi\lambda \Delta z_i f_x^2 \quad (12)$$

so that the electric field at the next optical element is given by

$$U_{i+1}(x) = \int_{-\infty}^{\infty} A_{i+1}(f_x) \exp [i2\pi f_x x] df_x \quad (13)$$

where $A_{i+1} = A_i H_i(f_x)$. Propagation is done in frequency space; amplification and phase transformation are done (discretely) in configuration space.

The transfer function has a strong oscillatory character compared with the relatively slowly varying Fourier spectrum. Since $H(f_x)$ depends on the resonator geometry only, H is carefully averaged using a fine mesh for each of the discrete spatial frequencies. This minimizes sampling errors and allows a relatively coarse mesh to be used in computing U .

The number of points used to compute the electric field is large compared with the number of points used to represent the intensities I_i^+ and I_i^- that are used in the kinetics calculations. The laser medium is typically divided into 30 cells, 10 of which are assigned to each of 3 gain sheets. This fluid resolution has been adequate to simulate 1- and 2-m long cavities in KrF lasers. The electric field is underresolved even with 512 points for each optical element. Values of N in excess of 30 000 are required to resolve each of the resonator Fresnel zones adequately. The larger number of points serves to resolve the small amplitude, high frequency oscillations in the electric field. Since these oscillations are unimportant in power extraction calculations and a relatively small N allows predictions of uniform optical phase in the resonator (as expected for

large Fresnel numbers), values of N ranging between 64 and 512 have been used in computations. Plots of intensity and phase distributions of the field for two typical calculations are presented in Section V.

The temporal advancement of kinetics and optics calculations is treated sequentially. The kinetics variables in each of the fluid cells are advanced over a period Δt while holding the cavity intensity constant. The kinetics variables are then held constant while the optical field is propagated. It is necessary that the laser gain does not change significantly during Δt . If Δt is not controlled carefully, the relaxation oscillations that result from coupling the laser medium to the radiation field can cause undamped numerical instabilities. We have used a Δt corresponding to half of a photon round trip in the resonator, although this approaches the limit of numerical stability for a 2 m cavity.

III. DISCHARGE MODELING

The remaining source of pump power to the laser medium, the electric discharge, must now be discussed in greater detail. The application of an electric discharge can be a very efficient means of supplying lasing energy, but it introduces a great many difficulties to both the experiment and the simulations.

The problems for simulations stem from the fact that, in the presence of an electric discharge, the electron distribution function is no longer Maxwellian. The rates for all those processes *directly involving the secondary electrons accelerated in the discharge*—ionization, excitation, attachment, and recombination—depend upon the precise shape of the electron distribution function. Hence, a solution must be obtained to a Boltzmann equation defining that distribution function, and the relevant processes' cross sections integrated over that distribution function.

For the lasers discussed here, and indeed for most electronic-transition lasers currently under investigation, it is fortunately adequate to assume that the electron distribution thermalizes on timescales short compared to other processes of interest. In discharge-pumped KrF mixtures, for example, this time is calculated to be a small fraction of a nanosecond, while typical chemical kinetics timesteps are several nanoseconds or more. Thus, it is adequate to solve a steady-state Boltzmann formulation at regular intervals in the kinetics calculation, rather than to attempt a complete time-dependent solution of the Boltzmann equation in parallel with the kinetics (which would prove to be a calculation too long to be of practical interest).

Hence, we present here a convenient and fast procedure for solving a steady-state Boltzmann equation to obtain quantities of interest for laser kinetics. Experience with particular gas/discharge systems will teach the user how often the Boltzmann routine need be called during each kinetics simulation. In general, it is adequate to prescribe that the routine be called whenever the electron density (calculated by the kinetics equations), average electron temperature (estimated) or gas temperature (calculated by the heat balance equation) changes by 10 percent.

Boltzmann Transport Equation

The steady-state Boltzmann equation for the electron energy distribution function (where u is the electron kinetic energy in eV) can be written [12]

$$\begin{aligned} \frac{1}{3} \left(\frac{E^2}{N} \frac{d}{du} \left(\frac{u}{Q_1} \frac{df}{du} \right) + \frac{2m}{M} \frac{d}{du} (u^2 Q_2 f) \right. \\ \left. + \frac{2mkT}{Mc} \frac{d}{du} \left(u^2 Q_2 \frac{df}{du} \right) + \sum_j (u + u_j) f(u + u_j) \right. \\ \left. - Q_1(u + u_j) - uf(u) \sum_j Q_j(u) + \sum_j (u - u_j) f(u - u_j) \right. \\ \left. - Q_{-j}(u - u_j) - uf(u) \sum_j Q_{-j}(u) \right) = 0, \end{aligned} \quad (14)$$

where E is the electric field strength, N is the total gas particle density, e and m are the electron charge and mass, respectively, k is Boltzmann's constant, and T is the molecular temperature.

The mean molecular weight M is calculated by summing over all the mixture components.

$$M = \sum_n M^n G^n, \quad (15)$$

where M^n is the molecular mass of component n and G^n is its mole fraction. The mole-weighted momentum transfer cross section Q_1 is calculated from

$$Q_1(u) = \sum_n Q_m^n(u) G^n \quad (16)$$

while the reciprocal-mass-weighted momentum transfer cross section Q_2 is given by

$$Q_2(u) = \sum_n \frac{M Q_m^n(u) G^n}{M^n} \quad (17)$$

In these expressions, $Q_m^n(u)$ is the total electron momentum transfer cross section for a collision between an electron of energy u and the n th gas component.

The j th inelastic process involves an electron energy loss of u_j and has a cross section of $Q_j(u)$, while the j th superelastic processes, involving an electron energy gain of u_j , has a cross section of $Q_{-j}(u)$. The superelastic cross section is derived from the inelastic cross section by the principle of detailed balance, viz.,

$$Q_{-j}(u) = \frac{u + u_j}{u} Q_j(u + u_j). \quad (18)$$

The electron energy distribution function f is normalized so that $\int_0^\infty u^{1/2} f(u) du = 1$. Thus $N_e u^{1/2} f(u) du$ (where N_e is the total electron density) is the number density of electrons with energies in the range from u to $u + du$.

Difference Version

Taking straightforward difference of the derivative terms in (14), the equation can be cast easily in one-dimensional tri-

diagonal form for the independent variable f

$$(B + A)f_{i-1} = (A + B)f_{i+1} + (C - 2A)f_i + S \quad (19)$$

where the quantities A , B , C , and S are defined

$$(\Delta u)^2 A = \frac{1}{3} \left(\frac{E}{N} \right)^2 \frac{u}{Q_1} + \frac{2mkT}{Me} u^2 Q_2, \quad (20)$$

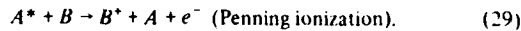
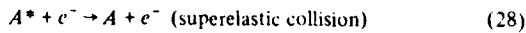
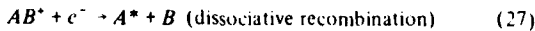
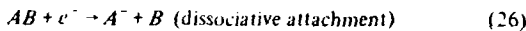
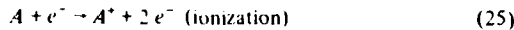
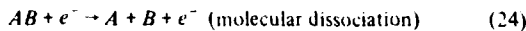
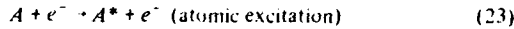
$$2\Delta u B = \frac{1}{3} \left(\frac{E}{N} \right)^2 \left[\frac{1}{Q_1} - \frac{u}{Q_1^2} \frac{dQ_1}{du} \right] + \frac{2m}{M} u^2 Q_2 + \frac{2mkT}{Me} \left[2uQ_2 + u^2 \frac{dQ_2}{du} \right], \quad (21)$$

$$C = \frac{2m}{M} \left[2uQ_2 + u^2 \frac{dQ_2}{du} \right], \quad (22)$$

and S represents the last four summations in (14).

Assumptions, Approximations, and Solution

Several types of electron collision processes are considered. Schematically, these are



Here A and B represent two atoms in the gas mixture and e^- is an electron. The asterisk refers to an electronically excited atom while the superscript plus sign designates an ion. One may also have multiply excited states, excited from both the ground state and lower-lying metastables; ionization of metastables; molecular ion processes; in short, all possible combinations of such reactions.

Processes (23), (24), and (28) involve no loss or gain of electrons but only a redistribution in energy, and thus the contributions of these processes to the electron energy distribution function are treated exactly by this algorithm. The other processes, (25), (26), (27), and (29) involve either the gain or loss of an electron and certain assumptions are made in the treatment of these processes. For ionization [Reaction (25)], it is assumed that the incident electron loses an amount of energy equal to the ionization potential of A and the secondary electron is created with zero energy. Furthermore, the effect of these newly created zero-energy electrons on the electron energy distribution function is ignored (although their contribution to the total electron density is accounted for by the chemical kinetics equations). Similarly, electrons created by Penning ionization, process (29), are ignored as far as their effect on f is concerned but are accounted for in computing the total electron density in the kinetics. A comparison of the

number of electrons produced by electron impact ionization and by Penning ionization with the number produced by e -beam ionization is made after each run to assure the validity of neglecting the effect of the former electrons on f .

Dissociative attachment and dissociative recombination (processes (26) and (27), respectively) involve the loss of electrons from a continuum of energies but no subsequent creation at other energies. These are treated in the Hiltzmann code by including an inelastic loss term but no gain term.

The recursion relation (19) is solved by the following method. Suppose that the energy axis has been divided into I bins, each of width Δu . Choose a small number, say 10^{-20} , and set $f(I) - f(I-1) = 10^{-20}$. Then using (19) solve for all $f(u)$ down to $f(1)$. Whenever a particular value of $f(u)$ becomes greater than 10^{-20} , multiply all values calculated thus far by 10^{-20} and proceed. When all $f(u)$ have been calculated, normalize the distribution as specified. This process straightforwardly deals with all elastic collision terms and with all inelastic terms ionization, excitation, attachment, and dissociative recombination which remove energy from the electron gas.

Superelastic Collisions

These inelastic collisions, also known as "collisions of the second kind," cause difficulties for a solution technique which moves down the energy axis because they scatter electrons up the energy axis; thus an iterative solution is necessary. The trial solution for $f(u)$ is obtained exactly as before, ignoring the existence of the superelastic terms.

At this point, approximate values of f exist at all grid points allowing an estimate of the summation involving $f(u - u_i)$ in (14). Several iterations are then performed to yield successively better approximations for f . The superelastic terms are introduced partially for the first iteration by multiplying their contribution by $\sim 10^{-3}$ – 10^{-2} . For each successive iteration, this multiplying factor is increased until it remains at unity for the last few iterations. Typically, from four to six iterations are required for convergence.

Electron-Electron Interactions

Collisional processes within the electron gas can be of great significance in discharge-pumped lasers when the electron density in the gas grows great (in excess, roughly, of $2 \times 10^{14} \text{ cm}^{-3}$) [13]. These densities will occur when the gas is pumped hard with the discharge, or when the discharge is run in a self-sustained mode. Electron-electron interactions change the electron distribution function, tending to drive it toward a Maxwellian distribution at temperature T_e , without adding energy to the electron gas.

In velocity (v) space, the electron-electron collision operator is [14], [15]

$$\left(\frac{df_0^1}{dt} \right)_{ee} = \frac{Y}{v^2} \frac{\partial}{\partial v} \left[f_0^1(v) f_0^0(v) + \frac{mv^2}{3} (I_2^0 + J_{-1}^0) \frac{\partial f_0^1}{\partial v} \right] \quad (30)$$

where $N_e = \int f_0^1 d^3v$, is the electron number density with f_0^1 in units of $\text{s}^{-3} \cdot \text{cm}^{-6}$

$$\epsilon \equiv mv^2/2$$

$$Y \equiv 4\pi \left(\frac{e^2}{4\pi\epsilon_0 m} \right)^2 \ln \Lambda$$

$$I_0^0 \equiv 4\pi \int_0^v f_0^0 x^2 dx$$

$$I_2^0 \equiv \frac{4\pi}{v^2} \int_0^v f_0^0 x^4 dx$$

and

$$J_{-1}^0 \equiv 4\pi v \int_v^\infty f_0^0 x dx.$$

Using a normalized distribution function, $\int_0^\infty f_0(u) u^{1/2} du = 1$, this operator can be rewritten in energy (u) space as

$$\left(\frac{\partial f_0}{\partial t} \right)_{ee} = N_e (4.84 \times 10^{-5}) \ln \Lambda u^{1/2} \frac{\partial}{\partial u} \left[f_0(u) \mathcal{G}_0^0(u) \right. \\ \left. + \frac{2u}{3} (\mathcal{G}_2^0 + \frac{1}{2} \mathcal{G}_{-1}^0) \frac{\partial f_0}{\partial u} \right] \quad (31)$$

where

$$\mathcal{G}_0^0 \equiv \int_0^u f_0 x^{1/2} dx$$

$$\mathcal{G}_2^0 \equiv u^{-1} \int_0^u f_0 x^{3/2} dx$$

and

$$\mathcal{G}_{-1}^0 \equiv u^{1/2} \int_u^\infty f_0 dx.$$

The term Λ above is the ratio of the Debye screening radius to the impact parameter required for a 90° deflection of an electron in a binary collision with another electron. We assume $\ln \Lambda$ is constant since it varies slowly with N_e and T_e . The constant 4.84×10^{-5} is a unit conversion factor which incorporates Y and allows the electron mass to be expressed in grams.

Since this operator effectively represents a diffusive process in energy space, it will scatter electrons up the energy axis as well as down; hence, like the superelastic collision term, it must be solved iteratively. Fortunately, the electron-electron operator can be included in the coding along with the superelastic operator, in the same iteration loop: no numerical difficulties arise from their conjunction, and whatever criteria are necessary for gradual introduction of the superelastic term will be more than sufficient for the electron-electron term. Thus, although considerable extra algebra is added by the electron-electron term, additional costly iterations to the solution of f are avoided. To be consistent in cgs units and energy in eV, the correct term to include in the iteration is

$$N^{-1} \left(\frac{3.2 \times 10^{-12}}{m} \right)^{-1/2} \left(\frac{\partial f_0}{\partial t} \right)_{ee},$$

where N is the total gas density in cm^{-3} and $(\partial f_0 / \partial t)_{ee}$ is defined by (31); because of the constant factor, the resulting term will have units $\text{cm}^2 \cdot \text{eV}^{-1/2}$.

Rate Coefficients and Transport Properties

Once a normalized electron distribution function has been calculated, it is a simple matter to calculate the rate coefficients for inelastic kinetic processes by integrating (with, for example, Simpson's rule) the appropriate cross section over the energy range of the distribution function. Since the electron velocity v is given by

$$v = \left(\frac{2eu}{m} \right)^{1/2} \quad (32)$$

the rate coefficient k_j for process j can be computed from

$$k_j = (Q_j v) = \left(\frac{2e}{m} \right)^{1/2} \int_0^\infty Q_j(u) u f(u) du. \quad (33)$$

Here, Q_j is the appropriate cross section for ionization, excitation, deexcitation (superelastic), attachment, or recombination.

Other important transport properties of the discharge gas can be obtained by similar simple integrations. These include the following.

The electron drift velocity:

$$w = \frac{1}{3} \left(\frac{E}{N} \right) \left(\frac{2e}{m} \right)^{1/2} \int_0^\infty \left(\frac{u}{Q_1} \right) \frac{\partial f}{\partial u} du; \quad (34)$$

The transverse diffusion coefficient:

$$D_T = \frac{1}{3N} \left(\frac{2e}{m} \right)^{1/2} \int_0^\infty \frac{u f}{Q_1} du; \quad (35)$$

The electron mobility:

$$\mu = \frac{w}{E}; \quad (36)$$

The average electron energy:

$$\bar{u} = \int_0^\infty u^{3/2} f du; \quad (37)$$

and the electron characteristic energy:

$$\epsilon_k \equiv \frac{D_T}{\mu}. \quad (38)$$

Power Balance

Once the electron energy distribution function is known, the partitioning of the discharge power (product of discharge voltage and current) into the various energy channels of the laser gas can be computed. The balance of this power provides a numerical check on the Boltzmann equation solver, while par-

TABLE I
DISCHARGE POWER BALANCE

PROCESS	CROSS SECTION	ENERGY TRANSFERRED PER COLLISION	RATE OF ENERGY TRANSFER PER UNIT VOLUME
Momentum transfer	$Q_{m,j}$	$\frac{2m}{M} u^a$	$\frac{2m}{M} N_e N_j \left(\frac{2e}{m}\right)^{1/2} \int Q_{m,j} u^2 f du$
Excitation	$Q_{e,j}$	$\Delta E_{p,j}$	$\Delta E_{p,j} N_e N_j \left(\frac{2e}{m}\right)^{1/2} \int Q_{e,j} u f du$
Ionization	$Q_{i,j}$	$\Delta E_{p,j}$	$\Delta E_{p,j} N_e N_j \left(\frac{2e}{m}\right)^{1/2} \int Q_{i,j} u f du$
Attachment	$Q_{a,j}$	u^b	$N_e N_j \left(\frac{2e}{m}\right)^{1/2} \int Q_{a,j} u^2 f du$
Recombination	$Q_{r,j}$	u^b	$N_e N_j \left(\frac{2e}{m}\right)^{1/2} \int Q_{r,j} u^2 f du$
Superelastic	$Q_{s,j}$	$-\Delta E_{p,j}^c$	$-\Delta E_{p,j} N_e N_j \left(\frac{2e}{m}\right)^{1/2} \int Q_{s,j} u f du$

$$\text{Power in per unit volume} = EJ_D = E e N_e w$$

^aAverage energy transferred per collision

^bAll of the electron energy is lost

^cEnergy is returned to the electrons

tioning provides insight into the processes responsible for limiting or enhancing laser efficiency.

The electrons gain energy by being accelerated in the applied electric field. The rate of gain of electron energy per unit volume is $EJ_D = EeN_e w$, where J_D is the discharge current density. Some of this energy is transferred to the gas particles through the several types of collisional processes. The rate of transfer of energy per unit volume for a particular binary process p involving the collision of an electron and a particle designated by subscript j is

$$P_{pj} = N_e N_j \left(\frac{2e}{m}\right)^{1/2} \int_0^\infty \Delta E_{pj} Q_{pj} u f du \quad (39)$$

where Q_{pj} is the cross section for process p , and ΔE_{pj} is the average electron energy lost in the collision. The energy transfer rates for specific electron collisional processes of particular interest are shown in Table I.

External Circuit Coupling

When simulating an existing laser experiment, the measured temporal waveform of the discharge voltage $V_D(t)$ is used as an input parameter to the code. However, when the code is operated in a predictive mode, one must be able to compute the time history of V_D by coupling the external circuit parameters to the discharge kinetics.

The method for achieving this coupling is described here by considering, as a particular example, the circuit shown schematically in Fig. 3. This circuit contains three elements with

properties (capacitance, inductance, and resistance) which remain constant in time and a fourth element (the laser discharge) having a time-varying impedance which depends on the other three circuit elements, the discharge kinetics, and the external ionization source. The discharge impedance Z_D can be expressed as

$$Z_D = \frac{V_D}{I} = \frac{Ed}{N_e A e w} \quad (40)$$

where V_D is the potential across the discharge, I is the current in the circuit, w is the electron drift velocity [(34)], and d and A are the discharge gap length and area, respectively.

If one selects three independent variables which describe the LRC circuit of Fig. 3 to be the discharge current I , the discharge voltage V_D , and the time derivative of the discharge current dI/dt (define $G \equiv dI/dt$), then three differential equations involving these variables may be derived in a straightforward manner by applying Kirchhoff's laws to the LRC circuit:

$$\frac{dV_D}{dt} = \left[\frac{G}{eA} - \frac{dN_e}{dt} w \right] \frac{1}{N_e (dw/dV_D)}, \quad (41)$$

$$\frac{dG}{dt} = \left[\frac{dV_D}{dt} + RG + \frac{I}{C} \right] \frac{1}{L}, \quad (42)$$

$$\frac{dI}{dt} = G. \quad (43)$$

The following relationship between the current and the drift velocity was used in deriving (40) and (41):

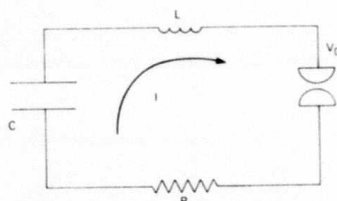


Fig. 3. Diagram of an LRC circuit coupled to discharge.

$$I = J_D A = ewN_e A, \quad (44)$$

where J_D is the discharge current density. The time rate of change, dN_e/dt , of the electron density is determined from the solution of the chemical kinetics equations.

Since (41)–(43) are a set of coupled first-order linear differential equations, they may be appended to the set of chemical kinetics equations and solved using the same algorithm. Thus the kinetics integrator keeps track of (and requires starting values of) I , dI/dt , and V_D .

The electron drift velocity and hence its derivative with respect to discharge voltage dw/dV_D depend mainly on V_D . They are coupled to the particle kinetics through their weaker dependence on fractional excitation and ionization but this effect was tested and found to be small enough to ignore for the present purposes. This negligible dependence allows the circuit equations to be merged into the set of chemical kinetics equations and solved on the same time grid along with the latter without frequent calling of the time-consuming Boltzmann equation solver. A table giving the functional dependence of dw/dV_D on V_D is generated initially for an average estimated fractional excited state density and ion density and for the range of V_D expected in a given simulation. This table is then interpolated to obtain the value of dw/dV_D required during the kinetics/circuit integration.

The absolute value of $E/N(=V_D/Nd)$ is fed into the Boltzmann transport equation solver when required to compute an updated electron energy distribution function.

The power P_D and the energy E_D deposited in the laser gas by the discharge are compared with the laser power and energy output to determine intrinsic laser efficiency. These quantities are given by

$$P_D = V_D I \quad \text{and} \quad E_D = \int V_D I dt.$$

Obviously, this procedure can be adapted to accommodate an external circuit of arbitrary topology simply by deriving the appropriate set of differential equations analogous to (41)–(43).

IV. OUTPUT AND DIAGNOSTICS

A well-calibrated laser kinetics code may be used, like any other simulation code, as a design aid to predict the performance of various system parameters. The code may actually be more useful, however, for studying experiments that have been performed than for predicting the results of future experiments. The easy accessibility of virtually every single physical parameter, many of which cannot be measured directly (and are costly and time consuming to measure inferentially), is

what makes such a code an invaluable tool in understanding complexly interactive systems, such as the rare-gas-halide lasers. It is important, then, that one's output parameters be carefully designed to provide the most useful information.

Assuming that a standard output interval has been established as a small fraction of the entire pulse length (pump + laser + afterglow), several quantities are of obvious interest: radiation parameters (intensity, energy radiated, fluorescence, net gain, total absorption); plasma properties and power balance (as defined in Section III); and the intrinsic or "local" efficiency of the pump process. This last is defined as the laser energy radiated divided by the total energy deposited in the gas, and can be calculated by summing all the excitations, ionizations, and heating caused by the e -beam and discharge. There other efficiency quantities are of interest. The creation efficiency (number of upper laser levels formed divided by number of ions made); the radiation efficiency (number of laser photons produced divided by number of upper laser levels formed); and fluorescence yield (product of the previous two).

For e -beam sustained discharge-pumped lasers, several other quantities are of interest. Most frequently used is the discharge "enhancement," which is defined (by convention) as power deposited by the discharge divided by power deposited by the e -beam. Again, this quantity can be calculated exactly, since the precise number of discharge-induced excitations and ionizations is known; it is useful, for purposes of comparison, to calculate and display the standard approximation to discharge enhancement, viz.,

$$\epsilon_{\text{Approx}} = \frac{J_D \cdot E}{\epsilon_A \gamma N_A - \sum_m (\epsilon_I n_I)_m} \quad (45)$$

where J_D and E are the discharge current density and field, respectively, ϵ_A is the average energy per ion pair, γ is the attachment rate, N_A is the number density of attaching species, and n_I and ϵ_I are the total number density and ionization potential for ions of species m formed by the discharge. The ionization rate ratio (the ratio of instantaneous values of the rates of ionizations driven by the discharge and ionizations driven by the e -beam) can also be of particular interest; when this ratio passes about 0.3, the discharge is heading for instability. Finally, the metastable loss rate ratio (number of metastable atoms ionized divided by number of metastable atoms forming the upper laser level) can also be a useful measure of discharge performance.

The actual temporal variations of the species number densities and their rates of change—printed intermittently and plotted on a semilog scale at the end of the pulse—are invaluable raw data, only a small fraction of which can actually be measured in any particular experiment.

Also of particular value in analyzing the importance of various kinetic processes is the display of the total contribution to each species' formation and depletion of each of the reactions which affects that species. With this data, one can decide precisely which of the competing energy paths dominates the laser performance. One can also decide at a glance which reaction rates need to be known precisely and which can be treated with order-of-magnitude estimates.

TABLE II
KrF LASER SIMULATIONS

EXPERIMENTAL PARAMETERS	EXPT 1	EXPT 2
Pumping mechanism	e-beam	e-beam sustained discharge
Total Pressure (atm)	1	2.01
Mix: Ar/Kr/F ₂	93.3/6.6/0.1	95.5/4.3/0.2
e-Beam Average Current Density (Amps/cm ²)	6	2
e-Beam Voltage (kilovolts)	300	400
Electrical Pulselength (nanoseconds)	500	500
Discharge Average Electric Field (KV/cm-atm)	--	2
Volume (liters)	60	30

RESULTS	EXPT	SIMULATION	EXPT	SIMULATION
Optical Output (joules)	120	124.8	36	39.6
Average Optical Flux (Watts/cm ²)	7x10 ⁵	8.1x10 ⁵	7x10 ⁵	7.8x10 ⁵
Local Efficiency (%)	7.2	8.0	3	3.4
Discharge Enhancement Ratio	--	--	2.4	2.3
Total Absorption (% cm ⁻¹)	?	0.39	?	0.3
g _o /g _a (small signal gain/absorption)	6(?)	9.3	-4	3.31
Ionization Rate Ratio	--	--	?	0.136

V. RESULTS

We present in this section representative results of simulations of two different lasers, krypton-fluoride (KrF) and xenon-fluoride (XeF), done with two different codes.

Two KrF simulations are summarized in Table II to demonstrate the high accuracy with which these methods can reproduce experimental results. Some of the excellent agreement between simulation and experiment shown here must be regarded as fortuitous, if only because some of the measured data are inferential. However, these simulation results are not chosen because they are the closest yet obtained: they are in fact representative. Similar accuracy has been obtained in simulating many other KrF laser experiments performed at Maxwell Laboratories, Inc., AVCO Everett Research Laboratories, and Northrop, and in simulating kinetics and absorption experiments at the same places and at Stanford Research Institute.

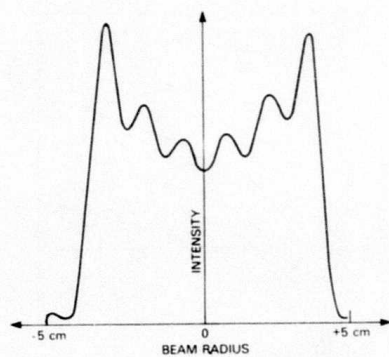
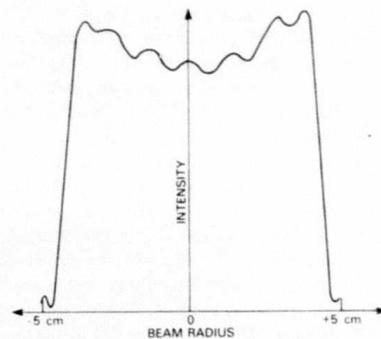
Some of the general features of KrF lasers run at room temperature can be observed in these results. The total energy density was relatively low—about 2 J/l in experiment 1 and about 1 J/l in experiment 2—because the e-beam currents were low and because experiment 1 was run at 1 atm total pressure. At total pressures of about 2–2.5 atm and e-beam current densities 10 A/cm² or more, one can produce 10 J/l reliably; harder pumping can more than double this number,

but at severe penalties in local efficiency. The local efficiency of experiment 1 (~8 percent) is representative; values of 10–12 percent can be obtained with reliability in e-beam pumped lasers. Discharge-pumped efficiencies are in fact typically lower, though by a factor of about 1.2, rather than the factor of 2 illustrated by these experiments.

Typically results of one-dimensional physical optics resonator simulations are shown in Figs. 4 and 5. In each figure, the top drawing shows the distribution of intensity across the beam incident on the output mirror of an unstable confocal resonator; the bottom drawing shows the phase distribution across the beam. Fig. 4 is from the simulation of an e-beam excited laser at AVCO Everett Research Laboratories. The cavity length was 1 m, with 71 percent output coupling; the e-beam current density was 11.5 A/cm², and the 1.2 atm gas was partitioned 97.5 Ar/2.3 Kr/0.2 F₂. Fig. 5 shows results of an optics simulation of experiment 2 in Table II. The flat phase distribution resulting in both calculations is a gratifying result.

More detailed versions of these and other simulation results, with extensive interpretation, may be found in [14].

As an example of XeF modeling, results of a simulation of an e-beam-controlled XeF laser are compared with experiment [16] in Table III. For these calculations, the measured e-beam current and discharge voltage waveforms are used as input to the code.

Fig. 4. Intensity and phase distributions for AVCO *e*-beam pumped KrF laser.Fig. 5. Intensity and phase distributions for Maxwell *e*-beam sustained discharge KrF laser.TABLE III
XeF LASER SIMULATIONS

EXPERIMENTAL PARAMETERS		
Mixture	$\text{Ne/Xe/NF}_3 = 99.7/0.225/0.075$	
Total pressure	3.0 atm @ $T = 300^\circ\text{K}$	
Laser cavity length	150 cm	
Laser gain length	100 cm	
Mirror reflectivity	50%	
Pump pulse length	1.1 μsec (e-beam and discharge)	
E-beam energy deposited	40 J/l ($J_{\text{eb}} = 3 \text{ A/cm}^2$)	
Discharge energy deposited	120 J/l	
Total pump energy	160 J/l	
RESULTS		
<u>E-beam only</u>	EXPT	MODEL
Optical output	0.88 J/l	0.99 J/l
Local efficiency	2.2%	2.5%
<u>E-beam controlled discharge</u>		
Optical output	2.8 J/l	3.7 J/l
Local efficiency	1.75%	2.3%
Discharge enhancement	3.2:1	3.7:1

The predictions of laser performance agree within experimental error. The slightly high values of optical output may be explained from the incomplete treatment by the model of direct formation and mixing (by heavy particles and electrons) of the *B* and *C* states of excited XeF. Detailed studies of the role of the *C* state in XeF lasers have been carried out for *e*-beam pumping [17] but the effect of discharge electrons (possibly increased mixing) in XeF *B*- and *C*-state kinetics is not yet well understood.

Curves showing the computed temporal evolution of selected laser-medium components for the XeF laser model of Table III are plotted in Fig. 6. The pump pulses (*e*-beam and sustainer) for this simulation are switched on at a time corresponding to zero on the abscissa of Fig. 6, have a 100 ns risetime and are cut off at 1200 ns.

The curve labeled " $h\nu_L$ " is the number density of intracavity laser photons traveling along the laser axis. The buildup time of ~ 200 ns for the laser flux agrees well with the experiment. Note the drop in XeF* density when the laser flux begins to build up towards saturation. The curve for NeXe* is shown since for these conditions it is the main precursor of the upper laser level XeF*.

For long-pulse rare-gas-halide lasers it has been observed that the pulse duration over which one can obtain high efficiency is limited by the onset of discharge instability. Some insight into the mechanism for the instability onset is apparent from Fig. 6. The steady rise in electron (e^-) density during the pulse is shown from the kinetics calculations to be due to a steadily declining electron loss rate caused by depletion of the electron attenuator NF_3 . The dashed curve in the figure indicates an NF_3 depletion of about a factor of two for the conditions modeled here.

The increase in ionization rate accompanying the rise in electron density, when coupled with a reduced attachment rate caused by NF_3 depletion, tends to drive the discharge toward instability. Both the experiment and the simulation show that the discharge remains stable for the complete 1200 ns pump pulse at 160 J/l total energy input. However, for an E/N value only ~ 10 percent higher than that used for the experiment of Fig. 6, the model shows a faster than exponential rise to an unrealistically high electron density before pump cutoff and, in agreement, the experiment shows a discharge arc resulting in a rapid drop in discharge impedance and premature termination of the optical pulse.

VI. CONCLUSION

None of the individual techniques described here is particularly novel. But the careful interworking of them has produced a predictive capacity of unprecedented precision in high-powered lasers, and made significant contributions to the developments of these lasers. These results were obtained not by concentration on sophisticated numerics, but by close cooperation with experimentalists while both codes and lasers were being developed. In fact, conscientious efforts were made to keep the numerics the simplest that could be made to do, so that experimental uncertainties were always greater than computational ones. In such a hybrid model the chief

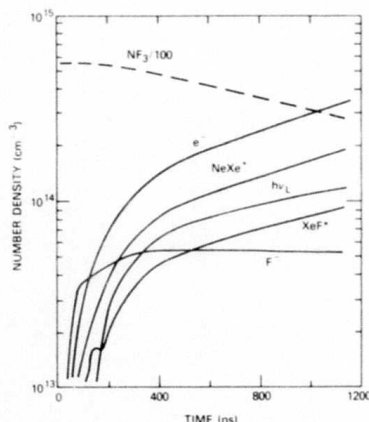


Fig. 6. Time history of number densities of selected species in *e*-beam-controlled XeF laser simulation.

difficulties one must be conscious of arise not from subtleties in the numerical approximations themselves, but from inconsistencies (qualitative and quantitative) in the fusion of many physical assumptions.

ACKNOWLEDGMENT

L. J. Palumbo extends his gratitude to T. G. Finn and L. F. Champagne for their close cooperation in developing the XeF code and for providing experimental data for comparison with calculations.

REFERENCES

- [1] D. H. Douglas-Hamilton and R. S. Lowder, "Carbon dioxide electric discharge laser kinetics handbook," Air Force Weapons Lab., NM, Rep. AFWL TR-74-24, 1978.
- [2] P. W. Milonni and A. H. Paxton, "Model for the unstable-resonator carbon monoxide electric-discharge laser," *J. Appl. Phys.*, vol. 49, pp. 1012-1027, 1978.
- [3] T. H. Johnson and A. M. Hunter, "DF-CO₂ transfer laser kinetics code," in *Laser Digest*. New Mexico: Air Force Weapons Lab., 1975, p. 174.
- [4] C. E. Treanor, "A method for the numerical integration of coupled first-order differential equations with greatly different time constants," *Math. Comput.*, vol. 20, pp. 39-45, 1966; also, C. E. Treanor, "A method for the numerical integration of coupled first-order differential equations with greatly different time constants," Cornell Aeronautical Lab., Inc., Buffalo, NY, CAL Rep. AG-1729-A-4, 1964.
- [5] M. J. Berger and S. M. Seltzer, "Tables of energy losses and ranges of electrons and positrons," National Aeronautics and Space Administration, Washington, DC, Rep. NASA SP-3012, 1964.
- [6] R. O. Hunter, Maxwell Labs., Inc., private communication.
- [7] D. B. Brown and R. E. Ogilvie, "An electron transport model for the prediction of x-ray production and electron backscattering in electron microanalysis," *J. Appl. Phys.*, vol. 37, pp. 4429-4433, 1966.
- [8] D. B. Brown, D. B. Wittry, and D. F. Kyser, "Prediction of x-ray production and electron scattering in electron-probe analysis using a transport equation," *J. Appl. Phys.*, vol. 40, pp. 1627-1636, 1969.
- [9] T. C. Salvi, "A description and comparison of methods for computing diffraction integrals," in *Laser Digest*. New Mexico: Air Force Weapons Lab., 1975, pp. 71-79.
- [10] D. E. Phelps, R. Baumgardner, and G. H. Canavan, "GDL power

- extraction using fast Fourier transform," presented at the AIAA Twelfth Aerospace Sciences Meeting, Washington, DC, Paper 74-181, Jan. 30-Feb. 1, 1974.
- [11] E. A. Sziklas and A. E. Siegman, "Mode calculations in unstable resonators with flowing saturable gain. 2: Fast Fourier transform method," *Appl. Opt.*, vol. 14, pp. 1874-1889, 1975.
- [12] L. S. Frost and A. V. Phelps, "Rotational excitation and momentum transfer cross sections for electrons in H_2 and N_2 from transport coefficients," *Phys. Rev.*, vol. 127, pp. 1621-1633, 1962; Also, J. J. Lowke, A. V. Phelps, and B. W. Irwin, "Predicted electron transport coefficients and operating characteristics of CO_2 - N_2 -He laser mixtures," *J. Appl. Phys.*, vol. 44, pp. 4664-4671, 1973.
- [13] W. H. Long, Jr., "Electron kinetics in the KrF laser," *Appl. Phys. Lett.*, vol. 31, pp. 391-394, 1977.
- [14] T. H. Johnson and A. M. Hunter, "Physics of the krypton-fluoride laser," *J. Appl. Phys.*, to be published.
- [15] I. P. Shkarofsky, T. W. Johnston, and M. P. Bachynski, *The Particle Kinetics of Plasmas*. London: Addison-Wesley, 1966, p. 284.
- [16] L. F. Champagne and N. W. Harris, "Characteristics of the electron-beam-controlled XeF laser," *Appl. Phys. Lett.*, vol. 33, pp. 248-250, 1978.
- [17] T. G. Finn, L. J. Palumbo, and L. F. Champagne, "The role of the C state in the XeF laser," *Appl. Phys. Lett.*, vol. 34, pp. 52-55, 1979.

Depletion of the Halogen Donor in the XeF Laser

A numerical modeling effort was conducted to investigate depletion of the halogen donor in e-beam pumped XeF lasers. The purpose of this investigation was to determine the extent of NF_3 depletion in the laser mixture, to characterize its effects on laser performance, and to estimate under what conditions these effects are significant. Using our kinetics model, we have calculated the extent of depletion and its possible consequences in the optimal laser mix (4 atm Ne/12 torr Xe/6 torr NF_3) for pumping currents of 10 A/cm^2 , pulse lengths of 1 and 10 μsec , and operation at elevated temperatures.

The major model predictions are the following: a) almost 25% of the NF_3 is depleted after 1 μsec , however, the effect on laser output is not significant; b) the major effects of depletion are likely to be an increase in the absorption due to Xe_2^+ , and greater formation through the Xe^* - neutral channel; c) for 10 μsec operation, the consequences and extent of depletion depend on the electron attachment rates and the termolecular recombination rates of the depletion products, NF_2 , NF and F .

I. Background

Efficient operation of the XeF laser has been achieved in neon diluent for pulse durations of approximately 1 μsec , and with energy loadings of less than 100 J/l. In order to project the laser performance at longer pulses with loadings of significantly more energy, one must determine what new effects will occur under these conditions and assess their impact.

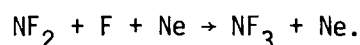
Two effects which are small for 1 μ sec operation but significant for longer pulses are depletion of the halogen donor, NF_3 , and gas heating from pump energy deposition. Depletion of the halogen donor can effect several aspects of the laser: the formation chain, absorption, quenching and interception. In the XeF laser, quenching and interception by NF_3 have only a small effect on the laser output. However, NF_3 , which produces F^- by dissociative attachment, controls the ion balance in the laser plasma, which in turn, controls the dominant formation and absorption processes. Thus, depletion of NF_3 may decrease the efficiency of the formation and extraction processes. Consequently, we have addressed depletion as it affects the ion balance in the laser plasma. However, we estimate that a temperature rise of a few hundred $^\circ\text{K}$ will occur for long pulses due to e-beam energy deposition. Recent results on heated XeF indicate that the laser performance decreases above a certain temperature.¹ If the laser works well only in a narrow temperature range, then for long pulse operation, the performance may be adversely affected by the amount of energy deposited by the e-beam.

II. Approach and Results

For the model simulation, the optimum laser mixture at 10 A/cm^2 pumping rate obtained by Rokni et. al.² was used. This mixture is 4 atm neon, 12 torr xenon and 6 torr NF_3 . The pumping pulse duration was varied from 1 μ sec to 10 μ sec. Simulations were run varying the attachment rates and recombination rates of the depletion products.

The effect of elevated temperature was crudely approximated by the following assumptions: first, the XeF ground state removal rate was significantly increased;³ second, the absorption cross section at the laser wavelength of Xe_2^+ was reduced⁴ so that greater amounts of xenon could be added to the mixture;⁵ and third, vibrational relaxation of the XeF (B) state manifold was increased.¹

The extent of depletion of NF_3 is determined by the balance between the removal and reformation processes. Dissociative attachment of electrons is the dominant depletion process. The major replenishment process is three-body recombination of the depletion products, i.e.,



If the recombination rate is insignificant then ~ 25% of the NF_3 will be depleted in the first microsecond. Moreover, 90% will be depleted in 3.5 μsec . However, if the three-body recombination rate is 10^{-31} the NF_3 concentration will stabilize at more than half its initial value.

The most serious effect of depletion will be to decrease the concentration of F^- , a key species in both the formation and extraction processes. In the ion formation chain, which accounts for almost 90% of the XeF (B) production during the first microsecond of the pulse, F^- recombines with various xenon ion complexes to form the upper laser level. Furthermore, by recombining with Xe_2^+ , F^- removes it as a major absorption species. The principal effect of F^- depletion will be to increase the absorption due to Xe_2^+ . Another effect will be to shift the formation process from one completely dominated by ion-ion

recombination reactions to one in which excited-neutral reactions are of comparable importance. Although ion-ion recombinations form the XeF (B) state with 80% efficiency,⁶ reactions of Xe* with NF₂ or NF may not be nearly as efficient. Thus, the formation efficiency may decrease as well as the extraction efficiency.

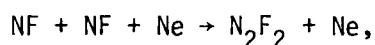
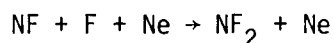
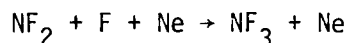
Other possible harmful effects of depletion involve the depletion products themselves. Interception or quenching by the NF₂, NF or F could be significant if the corresponding rate constant were of the order 10⁻⁹. As a final point, it has been recently pointed out to us that NF₂ does not absorb at 350 nm, but NF might.

III. Assessment of Depletion Effects

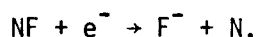
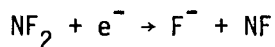
We have assessed the extent and effect of NF₃ depletion over the range where the three-body recombination rate constant of the depletion products is varied from 10⁻³⁴ to 10⁻³⁰ cm⁶/sec, and their attachment rate constant is varied from 10⁻¹⁰ to 5 x 10⁻⁹ cm³/sec. In general, the extent of depletion depends primarily on the termolecular recombination rate, and the consequences depend mainly on the attachment rate of the depletion products. If the recombination rate constant is greater than 10⁻³¹ cm⁶/sec, the NF₃ is reformed so rapidly that depletion is not significant. Likewise, if the electron attachment rate constant is the same as that of NF₃ (5 x 10⁻⁹ cm³/sec), the F⁻ concentration does not drop and the laser performance is unaffected. In order to avoid complications resulting from the XeF ground state and incomplete vibrational relaxation, we have calculated laser performance under "heated" conditions with various attachment and recombination rates for the depletion products. "Heated" conditions were

approximated by the following: (1) the XeF ground state was assumed to be unbound, (2) the absorption cross section at the laser wavelength of Xe_2^+ was set at half the room temperature value and the concentration of xenon increased to 1.5 times the room temperature value, (3) the relaxation time for vibrational mixing of the B-state manifold was set at 1 nsec. Moreover, it was assumed that neutral reactions involving Xe^* and the depletion products NF_2 and NF did not branch to the B-state.

Selected results of the calculations for heated XeF are summarized in Fig. 1. The computed laser output energy for a 10 μsec pump pulse is plotted in this figure as a function of k_{rec} , for various values of the electron attachment rate coefficient, β . Here, k_{rec} is the rate constant for the following termolecular recombination reactions.



and β is the rate constant for



Other relevant attachment and recombination rates were obtained from the literature.

The important conclusions drawn from Fig. 1 are: a) the laser performance will not degrade if the attachment rate constant of the

depletion products is approximately $5 \times 10^{-9} \text{ cm}^3/\text{sec}$, or if the three-body recombination rate is at least $1 \times 10^{-31} \text{ cm}^6/\text{sec}$; b) the laser performance will degrade only 10% if the attachment rate constant is at least $5 \times 10^{-10} \text{ cm}^3/\text{sec}$ and the recombination rate is at least $1 \times 10^{-32} \text{ cm}^6/\text{sec}$.

IV. Summary and Recommendations

We can draw the following conclusions:

a) The extent of depletion depends primarily on the termolecular recombination rate which controls the NF_3 reformation.

b) The effect of depletion depends on the electron attachment rate of the depletion products which control the F^- production.

c) The first major effect of depletion will be increased absorption due to Xe_2^+ .

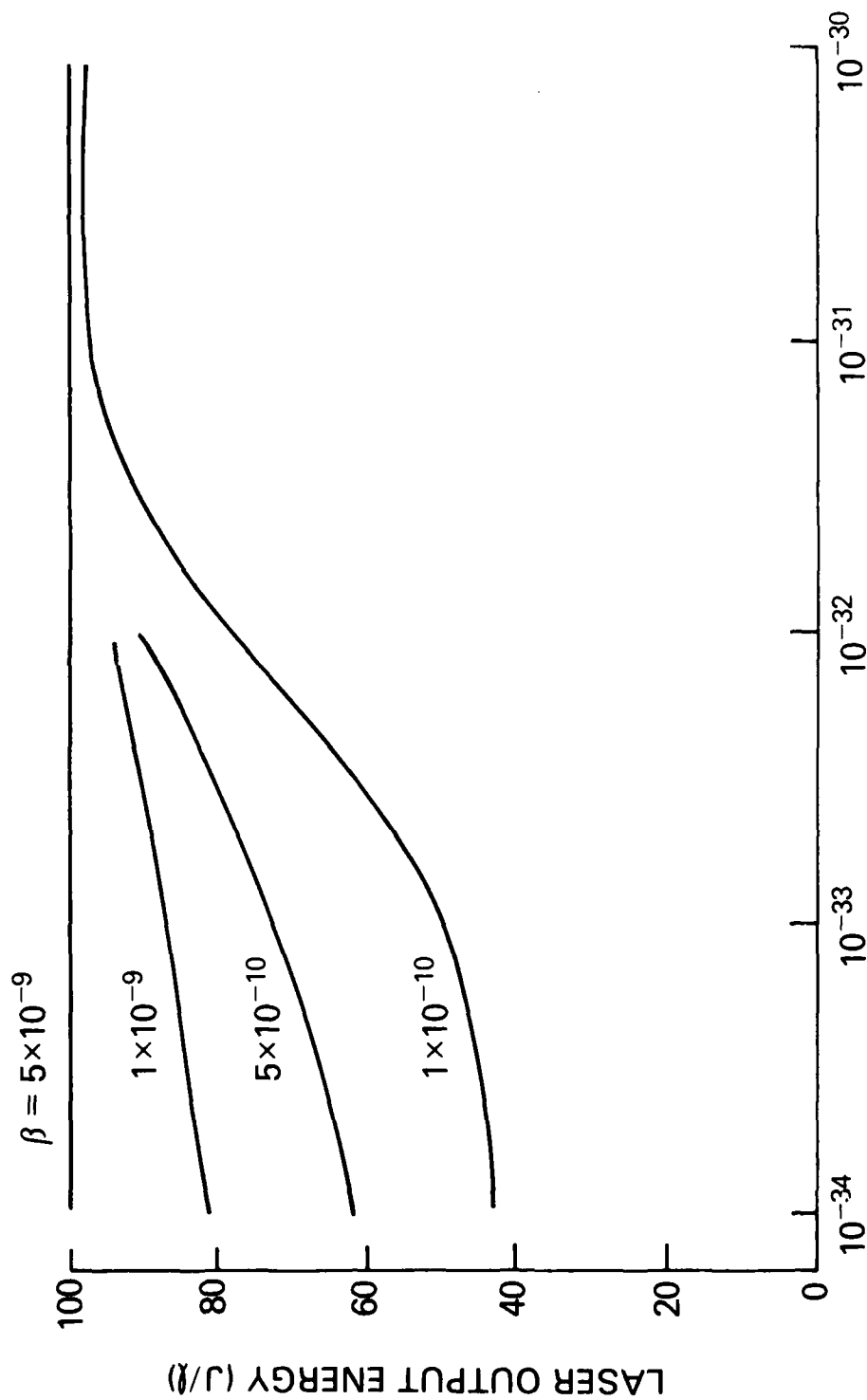
d) The second major effect will be increased formation through Xe^* neutral reactions, however, the total formation rate will remain approximately constant.

e) Effects of depletion on laser performance range from negligible to significant depending on the recombination and attachment rates.

As a result of this study we recommend that the following quantities are necessary to determine the effect of depletion on the laser performance: a) electron attachment and termolecular recombination rate constants for NF_2 and NF ; and b) the rate constants and branching ratios for reactions of Xe^* , and F^* with NF_2 and NF . In addition, rate constants for NF_2 and NF quenching of XeF^* and F_2^* and photoabsorption properties of NF are also important.

References

1. J. C. Hsia, J. A. Mangano, J. H. Jacob and M. Rokni, "Improvement in XeF Laser Efficiency at Elevated Temperatures," Appl. Phys. Lett. 34, 208-210 (1 February 1979).
2. M. Rokni, J. H. Jacob, J. A. Mangano, J. C. Hsia and A. Hawryluk, Papers CA-2, CA-3, and CA-4, 30th Annual Gaseous Electronics Conference, Palo Alto, CA, 18 October 1977.
3. T. G. Finn, L. J. Palumbo and L. F. Champagne, "A Kinetics Scheme for the XeF Laser," Appl. Phys. Lett. 33, 148-151 (15 July 1978).
4. W. R. Wadt, D. C. Cartwright and J. S. Cohen, "Theoretical Absorption Spectra for Ne_2^+ , Ar_2^+ , Kr_2^+ and Xe_2^+ in the Near Ultraviolet," Appl. Phys. Lett. 32, 672-674, (15 November 1977).
5. L. F. Champagne, private communication.
6. T. G. Finn, L. J. Palumbo and L. F. Champagne, "The Role of the C State in the XeF Laser," Appl. Phys. Lett. 34, 52-55 (1 January 1979), (reprint of article in Appendix).



TERMOLICULAR RECOMBINATION RATE (cm⁶/sec)

Fig. 1. Computed XeF laser output energy as a function of the molecular recombination rate constant of NF₃ depletion products for various values of the electron attachment rate coefficient (β) of NF₂ and NF. Calculations are for a pump pulse duration of 10 μsec and for approximate "heated" conditions.

APPENDIX I

Presented at: Thirty-first Annual Gaseous Electronics Conference,
Buffalo, NY, 17-20 October 1978, Paper E-2 (Workshop
Session)

The Role of Electron Kinetics in Discharge-Pumped Rare-Gas Halide Lasers

L. J. Palumbo
Laser Physics Branch
Naval Research Laboratory
Washington, D. C. 20375

A high level of activity by several research groups in the past few years has led to the development of the rare-gas-monohalide lasers as the most efficient class of visible/UV lasers to date. With several important applications as the reward, much work is continuing to develop further their potential for high output power and efficiency. The excitation method which promises the highest ultimate efficiency and the most straightforward scale-up to high powers is the acceleration of the laser-medium electrons in an applied electric field. Thus, in order to develop these lasers to optimum performance, it is important to understand the effect of electrons and their energy distribution on the formation and quenching kinetics of the lasing species and on the stability of the discharge.

Numerical studies which involve the solution of the Boltzmann transport equation for electron-beam-controlled and UV-preionized discharges in typical rare-gas-halide laser gas mixtures have been carried out.

These studies illuminate some of the major effects of discharge electrons on laser performance. Calculations of the partitioning of discharge energy into various channels of the laser medium have indicated limitations on the amount of energy which can be channeled into the upper laser level. The effects on discharge stability of the strength of the applied field, excitation and laser pulse length, and depletion of the molecular halogen donor during the laser pulse have been studied both numerically and experimentally. Other effects found to be important include coupling between external circuit elements and the discharge and the effect of electron-electron collisions on the electron energy distribution function.

ELECTRON BEAM PUMPED LASERS

Electron Beam Pumped XeCl Laser

The electron beam pumped XeCl laser has been demonstrated to have output power and efficiency comparable to the best observed results in KrF under similar pumping conditions during the past year.¹ This demonstrated capability coupled with the fact that the XeCl laser exhibits several characteristics which distinguish it from the rare gas fluoride lasers has generated considerable interest in this laser system. One example was the demonstration of efficient Raman conversion of 308 nm emission to the blue-green portion of the spectrum.² Also, the absence of measurable degradation in output power under static fill operating conditions distinguishes this laser from the rare gas fluorides (XeF, KrF) which have demonstrated high power and efficiency. Finally, the measured small signal gain of the XeCl laser is greater than that observed for either XeF or KrF lasers under similar pumping conditions. A power efficiency of ~ 6.5% was demonstrated for the electron beam pumped XeCl laser. These results were obtained in a 0.5 μ sec optical pulse when mixtures of neon, xenon and HCl were excited at a pumping current of ~ 7.5 A cm⁻² incident to the active volume. Laser emission was observed on the (0,1) and (0,2) vibrational bands of the B \rightarrow X transition at 308.0 and 308.2 nm respectively.³ A small signal gain of ~ 2.6% cm⁻¹ and a background absorption of ~ 0.26% cm⁻¹ were observed under

these operating conditions. Based on these measurements the saturation intensity is calculated to be $\sim 0.35 \text{ MW cm}^{-2}$.

References

1. L. F. Champagne, Appl. Phys. Lett. 33, 523 (1978).
2. R. Burnham and N. Djeu, Opt. Lett. 3, 215 (1978).
3. J. Tellinghuisen, J. M. Hoffman, G. C. Tisone and A. K. Hays, J. Chem. Phys. 64, 2482 (1976).

Efficient operation of the electron-beam-pumped XeCl laser

L. F. Champagne

Naval Research Laboratory, Washington, D.C. 20375

(Received 6 June 1978, accepted for publication 11 July 1978)

Efficient operation (50%) of the long-pulse (0.5 μ sec) XeCl laser is obtained by electron-beam pumping of mixtures of neon, xenon, and HCl. Laser emission is observed at 308.0 and 308.2 nm. A small-signal gain of 2.6% cm^{-1} is measured from which the saturation intensity is calculated to be $\sim 0.35 \text{ MW cm}^{-2}$ and the optical absorption at the laser wavelength is calculated to be $\sim 0.26\% \text{ cm}^{-1}$. The electron-beam-pumped XeCl laser can be operated under static fill conditions with no measurable degradation in output power.

PACS numbers: 42.55.Fn, 42.60.By, 42.60.Da

The electron-beam-pumped XeCl laser was first demonstrated in 1975, using as laser constituents, argon, xenon, and chlorine.¹ The laser efficiency and relative fluorescence efficiency measurements made by Ewing and Brau indicated that the XeCl laser was not as promising a candidate for scaling to higher efficiencies as was the KrF.

Since that time, a great deal has been learned about transient optical absorption in rare gases and the effect which this absorption has on the performance of both e-beam-pumped and e-beam-controlled rare-gas halide lasers.^{2,3} For the XeF laser this absorption is attributed to the dimer ions Ar_2^+ and Xe_2^+ and is essentially eliminated by using neon as a diluent in place of argon.⁴⁻⁸ The broad absorption band of these species extends to the XeCl emission band at 308 nm.⁹⁻¹¹ In addition, ground-state absorption from Cl_2 occurs in this spectral range.¹²

Thus, efficient operation of the XeCl laser can only be achieved by avoiding argon as a diluent, preventing significant Xe_2^+ formation and the use of a halogen donor which does not absorb at 308 nm. Burnham¹³ recently demonstrated high efficiency in a discharge-pumped XeCl laser using HCl as the molecular halogen donor. Using this donor as well as neon diluent we have demonstrated high power and efficiency for the electron-beam-pumped XeCl laser. The results obtained compare favorably in efficiency to the best results obtained for KrF in the same experimental apparatus. Moreover, in marked contrast to the rare-gas fluorides (XeF, KrF) the XeCl laser operates repeatedly with a static fill of gas without measurable degradation in performance.

In this experiment, a Maxwell cold-cathode gun which has been described previously² is used. The laser

chamber is 1 m long and has an active volume of 380 cm^3 . The laser chamber is designed to operate over a pressure range 1–5 atm. Time-resolved output power is measured with an S-5 photodiode. Output energy is measured using a GenTec ED-500 pyroelectric detector. Gain measurements are made using a Chromatix CMX-4 flashlamp-initiated dye laser. Spectral measurements are made using a $\frac{1}{4}$ -m Jarrell-Ash Ebert monochromator. Commercial grades of neon, xenon, and HCl were used in this experiment. Throughput filters were used to remove water vapor and other impurities from the laser constituents.

Figure 1 is a typical stimulated emission spectrum from the XeCl laser. Laser output was observed on (0,1) and (0,2) vibrational bands of the $B \rightarrow X$ transition at 308.0 and 308.2 nm, respectively.¹⁴ The relative intensities of these transitions were not influenced by

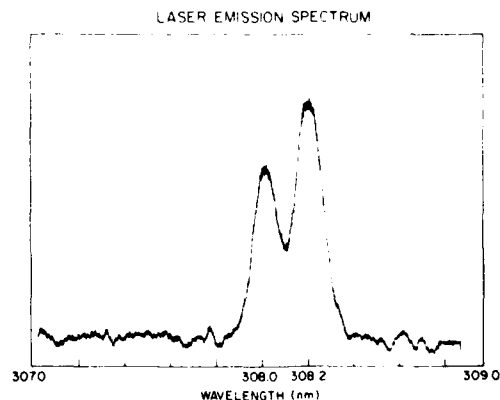


FIG. 1. Typical laser emission spectrum from XeCl.

pumping intensity, output coupling, or other experimental parameters.

Figure 2 plots the efficiency of the XeCl laser as a function of pressure over the pressure range 1–5 atm. Both maximum output power and efficiency were observed at 4 atm. At this pressure and for the optimum concentration of Ne: Xe: HCl (98.9:1.0:0.067) ~ 3.0 J l⁻¹ was extracted in a 0.5-μ sec optical pulse at an overall electrical efficiency of ~5.0%. The best output power at each pressure investigated was obtained for a gas composition in which the xenon to HCl ratio was 15:1, with the concentration of these species being 1.08×10^{18} cm⁻³ for xenon and 7.2×10^{16} cm⁻³ for HCl.

Unlike XeF and KRF, the XeCl laser was operated for tens of pulses from a single gas fill without measurable degradation in output power. The small variations in output which were observed (<10%) were directly proportional to observed fluctuations in the electron-beam current density which is incident to the foil. This contrasting performance between the rare-gas fluoride lasers and the XeCl laser is attributed to differences which involve the halogen donor. The three-body recombination rate for hydrogen chloride¹⁵ is comparable to that for fluorine.¹⁶ Therefore, these results indicate that HCl, Cl₂, and Cl⁻ do not react as readily with their environment as does F₂ and F⁻.

The small-signal gain of the electron-beam-pumped XeCl laser was measured by tuning the output from the flashlamp-excited dye laser to be coincident with the observed transition at 308.0 nm. At this wavelength the experimental gain was measured to be ~2.6% cm⁻¹. Figure 3 is a plot of the experimentally observed output power (*I*) as a function of output coupling for the XeCl laser under optimum operating conditions. Maximum output power was obtained with an output coupling of 72%. Analysis of the data indicates the presence of a significant transient optical absorption in the laser medium similar to that observed for Ar/Xe/NF₃ mixtures.² From this data the saturation intensity (*I*_s) and optical absorption $[1 - (1 - A)^2]$ can be estimated using the

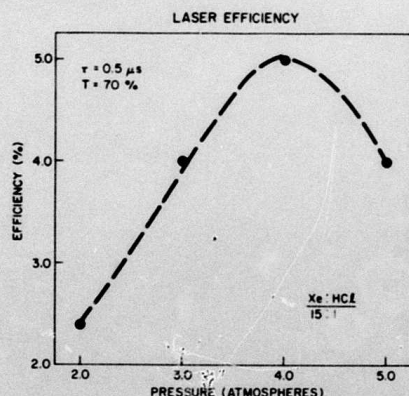


FIG. 2. Efficiency of the XeCl laser as a function of the total pressure.

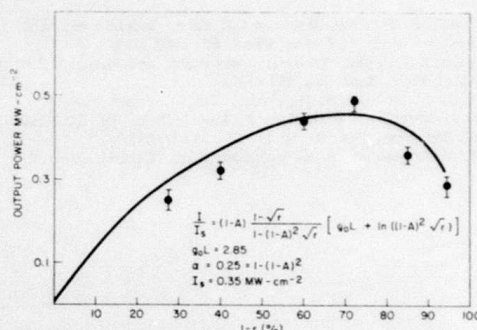


FIG. 3. XeCl laser output power as a function of output coupling.

equation²

$$\frac{I}{I_s} = (1-A) \frac{1-r^{1/2}}{1-(1-A)^2 r^{1/2}} \{g_0 L + \ln[(1-A)^2 r^{1/2}]\}.$$

This equation is a modified version of an expression first derived by Rigrod¹⁷ which relates output power, gain, and saturation intensity for high-gain lasers. In this modified expression we have included a lumped loss just in front of each mirror to approximate the loss within the laser medium itself. A best fit to the data gives a saturation intensity of ~0.35 MW cm⁻² and a transient optical absorption of ~0.26% cm⁻¹. The saturation intensity for XeCl is comparable to that for XeF. However, the transient optical absorption is large compared to that observed for the XeF laser in neon diluent.⁵ If this transient absorption could be removed or significantly reduced, then the output power and efficiency of the XeCl laser could be improved. Because of its high efficiency and its ability to operate without recycling the gas the XeCl laser offers the promise of being a very useful laser for many applications.

The author is grateful for many helpful discussions with R. Burnham, N. Djeu, and T. G. Finn and for the technical assistance of K. Tayman and D. M. Shores.

¹J. J. Ewing and C. A. Brau, *Appl. Phys. Lett.* **27**, 350 (1975).

²L. F. Champagne, J. G. Eden, N. W. Harris, N. Djeu, and S. K. Searles, *Appl. Phys. Lett.* **30**, 160 (1977).

³L. F. Champagne, 30th Annual Gaseous Electronics Conference, Palo Alto, Calif., 1977 Paper CA-5 (unpublished).

⁴L. F. Champagne and N. W. Harris, *IEEE J. Quantum Electron.* **QE-13**, 63-D (1977).

⁵L. F. Champagne and N. W. Harris, *Appl. Phys. Lett.* **31**, 513 (1977).

⁶J. H. Jacob, J. A. Mangano, and M. Rokni, Ref. 3, Paper CA-3.

⁷L. F. Champagne, *Electronic Transition Lasers III*, edited by K. L. Kompa and H. Walther (Springer-Verlag, Berlin, 1978), p. 32.

⁸B. Forestier and B. Fontaine, *4th Colloquium on Electronic Transition Lasers III*, edited by K. L. Kompa and H. Walther (Springer-Verlag, Berlin, 1978).

- ⁹Walter J. Stevens, Maureen Gardiner, Arnold Karo, and Paul Julianne, *J. Chem. Phys.* **67**, 2860 (1977).
- ¹⁰Willard R. Wadt, David C. Cartwright, and James S. Cohen, *Appl. Phys. Lett.* **31**, 672 (1978).
- ¹¹H. H. Michels and R. H. Hobbs, *Ref. 3, Paper BA-2*.
- ¹²P. J. Seery and D. Britton, *J. Phys. Chem.* **68**, 2263 (1964).
- ¹³R. Burnham, *Opt. Commun.* **24**, 161 (1978).
- ¹⁴J. Tellinghuisen, J. M. Hoffman, G. C. Tisone, and A. K. Hays, *J. Chem. Phys.* **64**, 2484 (1976).
- ¹⁵R. R. Gledt and T. A. Jacobs, *J. Chem. Phys.* **55**, 4144 (1971).
- ¹⁶I. P. Guzov, S. B. Kormer, L. V. L'vor, V. T. Punin, M. V. Sinitsyn, E. A. Stankeev, and V. D. Urtin, *Sov. J. Quantum Electron. A* **14**, 680 (1976).
- ¹⁷W. W. Rigrod, *J. Appl. Phys.* **36**, 2487 (1965).

Absorption Processes in XeCl Laser

Although the saturation intensity for XeCl is comparable to that for XeF the transient optical absorption is large compared to that observed for the XeF laser in neon diluent. If this transient absorption could be removed or significantly reduced then the output power and efficiency of the XeCl laser could be further improved.

Figure 1 plots the predicted extraction efficiency η as a function of the ratio of background absorption β to small signal gain α . The curve is derived from the modified Rigrod analysis for saturation intensity in a medium which exhibits a uniformly distributed loss. Optimum output coupling and low gain are assumed. The ratio of small signal gain to absorption for the XeCl laser under optimum operating conditions and at room temperature is 0.1. This translates to an extraction efficiency of $\sim 50\%$ of what is formed. If this ratio could be increased by either reducing transient absorption or increasing small signal gain then the extraction efficiency would also increase.

As a first step in determining whether absorption could be reduced experiments were performed to identify the dominant absorbing species.² Transient absorption in neon xenon and HCl mixtures and various rare gas combinations were measured. These results were matched with a numerical model to determine the dominant absorbing species in the XeCl laser. Briefly, we find that in pure neon plasmas Ne_2^* is the dominant absorber. Addition of xenon reduces this absorption through the mechanism of Penning Ionization. Absorption is not changed by adding HCl to the optimum neon/xenon concentration. Also, ground

state absorption due to HCl is not significant at the laser wavelength.³ These experiments indicate that the dominant absorbing species in laser mixtures is the dimer ion Xe_2^+ .

Figure 2a plots the measured absorption as a function of xenon concentration which was observed experimentally. Results were obtained by probing neon/xenon plasma with a flashlamp-pumped, frequency-doubled dye laser. The probe laser output was tuned to coincide with the 308.0 nm stimulated emission from the XeCl laser. The output from the probe laser was monitored with S-5 photodiodes before entering and after leaving the absorbing medium. A reduction in absorption at the laser wavelength was observed when small amounts of xenon were added to neon. As the xenon concentration was increased, absorption was observed to increase indicating that a new absorbing species involving xenon was introduced. The minimum measured absorption in neon/xenon mixtures was $\sim 0.25\% \cdot \text{cm}^{-1}$. This minimum was observed for xenon concentration ranging from 0.2 to 0.5%. For the XeCl laser, the optimum xenon concentration (1%) for best laser performance falls well within this minimum absorption region. Addition of HCl to neon/xenon mixtures did not alter the transient absorption markedly. This observation was corroborated by the fact that no measurable absorption in optimum neon/HCl mixtures was observed at this wavelength.

Figure 2b plots the relative number density of Ne_2^* and Ne_2^+ for the various xenon concentrations as predicted by the model. The dominant absorber for the optimum neon/xenon mixture is the dimer ion Xe_2^+ . There may be some smaller contribution which is attributed to atomic

transitions in neon between the 3s and 5p states centered at 3079.2, 3078.9, and 3077.0 Å.

Since the dimer ion, Xe_2^+ is the dominant absorber species then we know that the cross section for absorption by this species is a sensitive function of temperature.⁴ Wadt's ab initio calculations indicated that the cross section for absorption can be reduced by as much as a factor of two at the peak absorption wavelength with only moderate heating. However, there is poor agreement between the observed and calculated absorption peak as a function of wavelength. Preliminary experiments indicate that the calculated peak for absorption is ~ 20 to 30 nm closer to the visible than the experimentally observed absorption peak for Xe_2^+ (Fig. 3). Figure 3 is a plot of the measured absorption in xenon plasmas using the broad band probing technique. A large broad band of absorption with no line structure is indicative of dimer ion absorption. If the calculated absorption cross section is shifted to match the measured peak of absorption and if we assume that the overall shape of the absorption cross section does not change, then the ab initio calculations predict that absorption by Xe_2^+ at 308 nm has an inverse temperature dependence. This may account in part for the reduction in measured small signal gain which is observed at elevated temperatures as shown in Fig. 4.

Figure 4 is a plot in the measured small signal gain and background absorption in mixtures of neon, xenon and HCl as a function of temperature. The temperature of the laser chamber was varied from 300°K to 450°K. The measured small signal gain decreased with increasing

temperature. At elevated temperatures both laser performance and small signal gain were sensitive functions of when and how well the chamber walls were passivated. The results reported here were observed several minutes after the cell was passivated. The relatively large error (~ 10 to 20%) associated with the gain measurements is due to the increased reactivity which HCl exhibited with the chamber walls at elevated temperature. The measured background absorption while not increasing dramatically was subject to a large error range ($\sim 50\%$). This is attributed to the difficulty in accurately reproducing the probe wavelength when a continuously tunable probe source is used. These preliminary results indicate that there is a small but inverse temperature dependence in the measured small signal gain. The results are not sufficiently quantitative to determine whether the decrease in measured small gain is due to an increase in the background adsorption or a decrease in the real small signal gain. However, the results are sufficiently quantitative to warrant investigating laser performance at temperatures below 300°K . [If either the real gain or background absorption changes then laser extraction efficiency will improve as indicated from Figure 1.]

References

1. L. F. Champagne and N.W. Harris, Appl. Phys. Lett. 31, 513 (1977)
2. L. F. Champagne, L. T. Palumbo and T. G. Finn, Appl. Phys. Lett 34 315 (1979)
3. Jacques Romand, Ann. de Phys. 4, 527 (1979)
4. Willard and R. Wadt, David C. Cartwright and Hames S. Cohen, Appl. Phys. Lett. 31, 672 (1977)

EXTRACTION EFFICIENCY FOR OPTIMUM COUPLING AND LOW GAIN

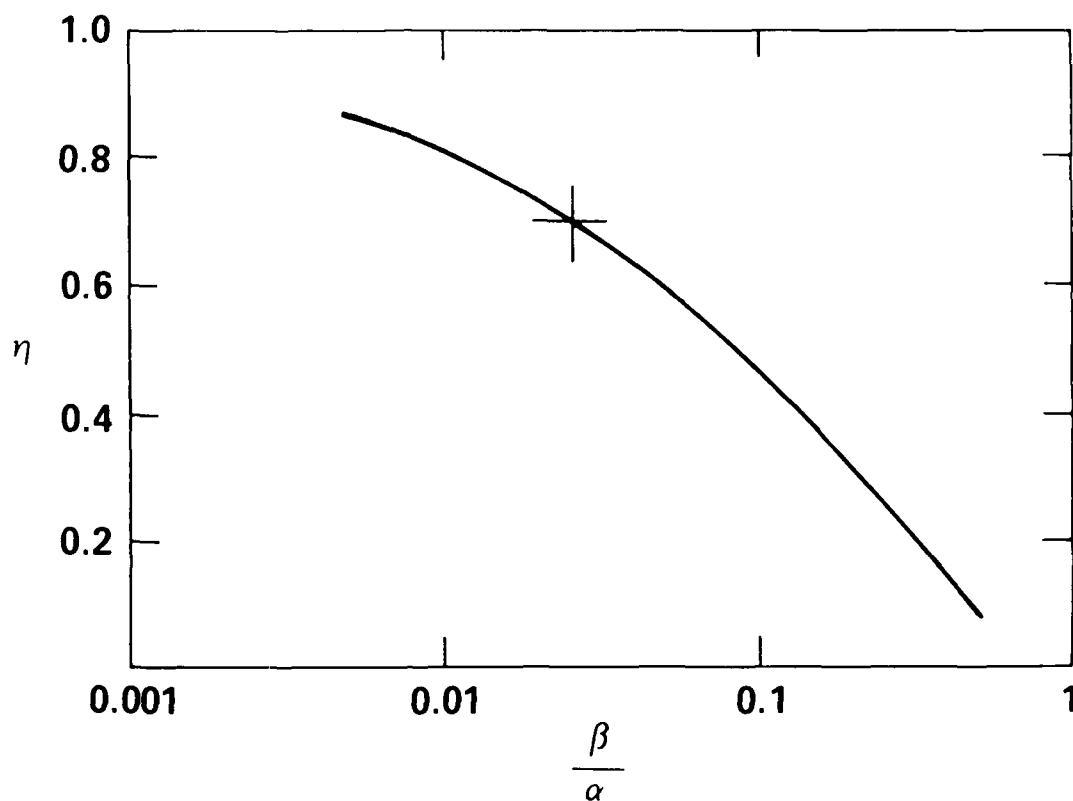


Figure 1. Extraction efficiency as a function of the ratio of absorption (β) to gain α .

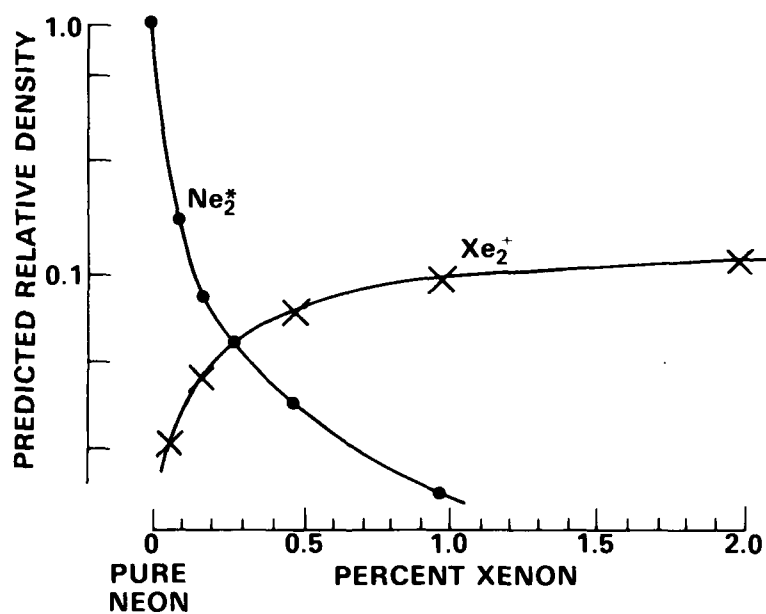
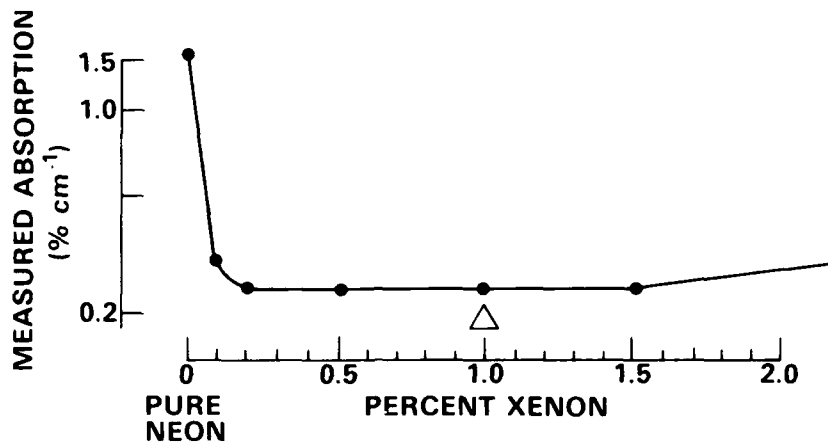


Figure 2a. Measured absorption as a function of xenon concentration at 308.0 nm.

2b. Predicted relative number density as a function of xenon concentration for two excited state species Ne_2^* and Xe_2^+ .

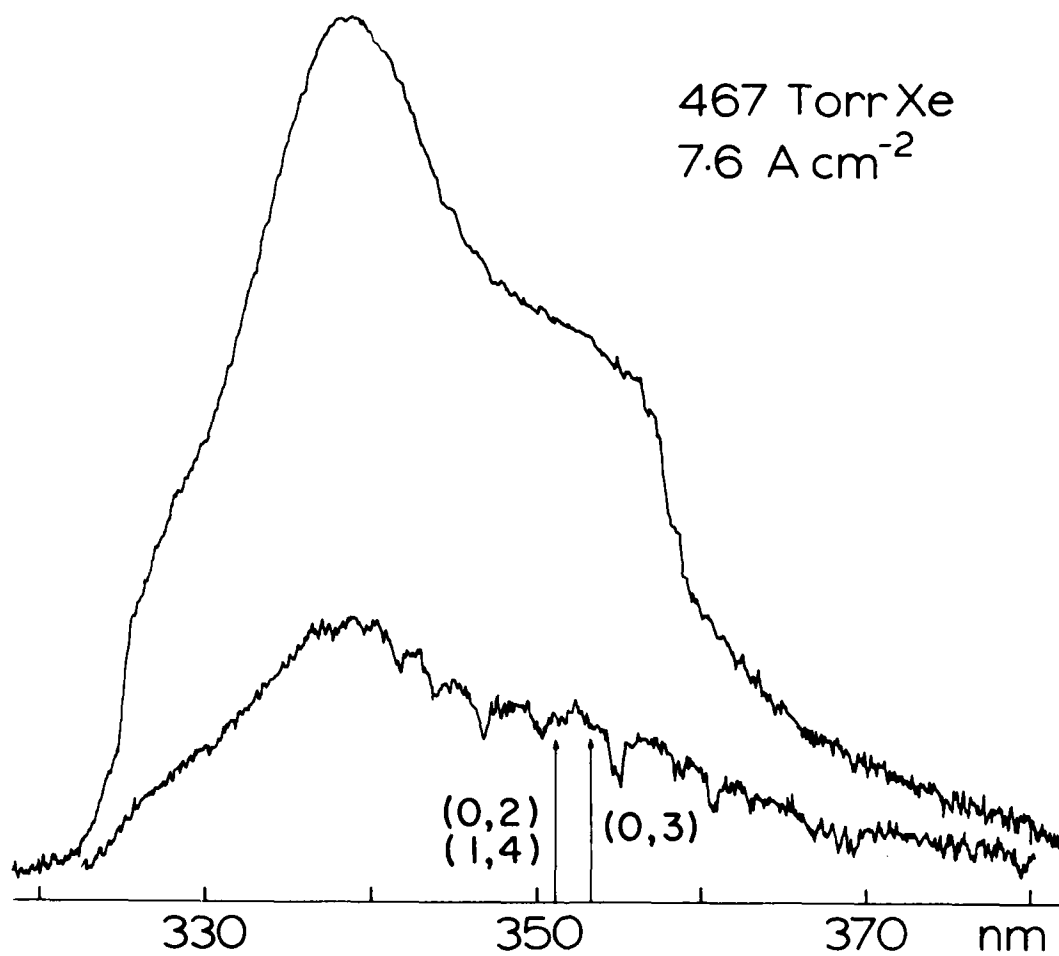


Figure 3. Two microdensitometer tracings show the broad band probe source when it is transmitted through excited xenon.

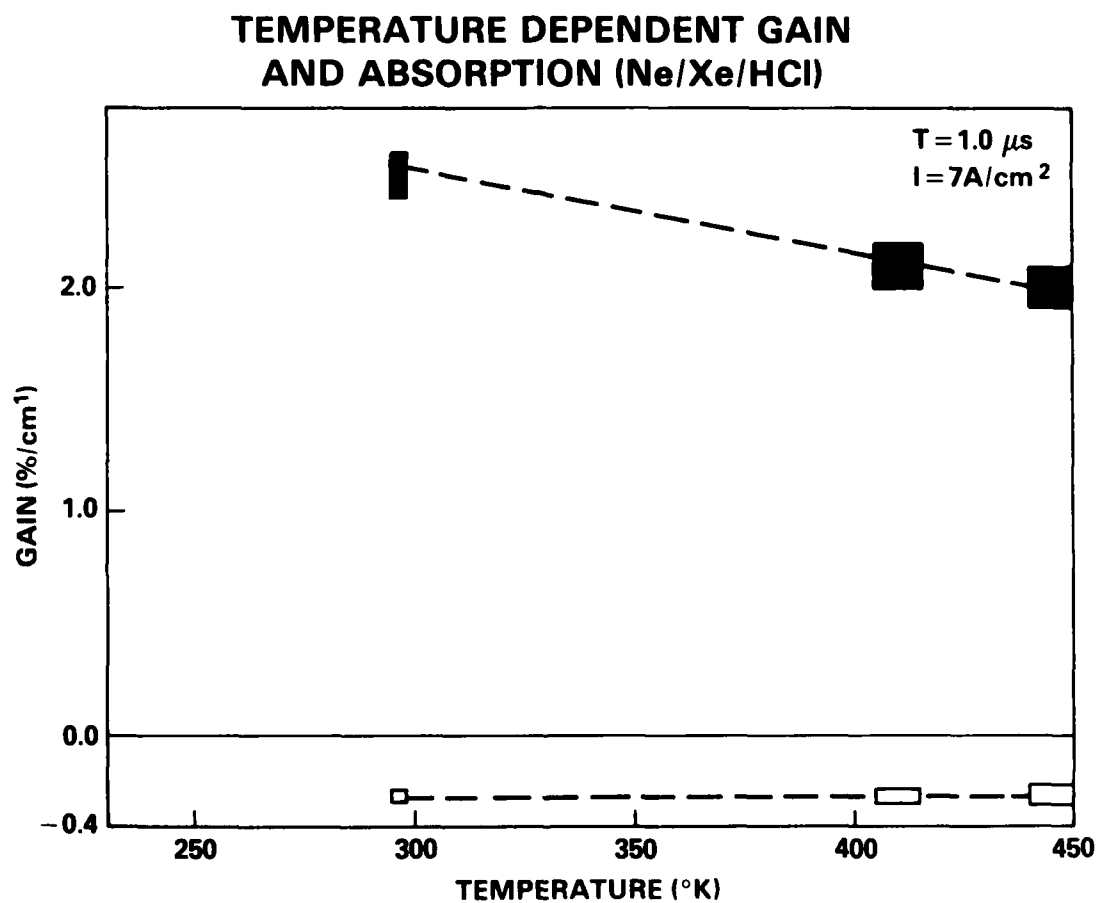


Figure 4. The measured small signal gain and background absorption in optimum laser mixtures as a function of temperature.

Absorption processes in the XeCl laser

L. F. Champagne, L. J. Palumbo, and T. G. Finn^{a)}

Laser Physics Branch, Naval Research Laboratory, Washington, D. C. 20375

(Received 16 October 1978; accepted for publication 5 December 1978)

Transient absorption in Ne/Xe/HCl mixtures and various rare gas combinations are measured. The observed results are matched with a numerical model to determine the dominant absorbing species in the XeCl laser. In pure neon plasmas Ne^* is a dominant absorber. Addition of xenon greatly reduces this absorption through the mechanism of Penning ionization. Absorption is not changed by adding HCl to the optimum neon-xenon concentration.

PACS numbers: 42.55.Hq, 42.60.He, 42.60.By

We recently reported on the efficient operation of an electron-beam-pumped XeCl laser in neon diluent.¹ The measured small signal gain of the XeCl laser was greater than the measured gain of the XeF laser. However, experimental results indicated that transient optical absorption in the XeCl laser was also large. A large transient absorption is detrimental to the laser performance.²⁻⁵

In this paper we report detailed measurements on the extent of these absorption processes near 308.0 nm. The experimental results do indicate that transient optical absorption in neon plasmas is broad, large at the laser wavelength ($1.5\% \text{ cm}^{-1}$) and increases linearly with increasing current. The addition of xenon to neon reduces this absorption to values comparable to those observed in neon-xenon mixtures at 351.1 nm.^{4,5}

The laser chamber used for these gain and absorption experiments has been described previously.¹ In these experiments the current density incident to the active volume was varied from 2 to 7 A cm^{-2} . A chromatix CMX-4 flashlamp-initiated dye laser was used to probe the active medium. The frequency-doubled output from a dye solution containing rhodamine 6-G probed the gas mixtures of interest in the wavelength region from 292 to 312 nm. The time-resolved dye laser output was monitored both before and after the laser chamber with S-5 photodiodes. The output spectrum of the dye laser was monitored with a $\frac{1}{2}$ -m Minuteman mon-

ochromator. The monochromator was calibrated with a mercury pen lamp.

Figure 1 plots the gain and absorption as a function of wavelength for a 1- μsec optical pulse under optimum operating conditions. For 1- μsec operation, the peak small signal gain was $2.4\% \text{ cm}^{-1}$ and the absorption was $\sim 0.24\% \text{ cm}^{-1}$. The background absorption in the laser mixture was measured at $\sim 0.5 \mu\text{sec}$ after the beginning of the optical pulse. Several shots were taken at each frequency setting. The axial

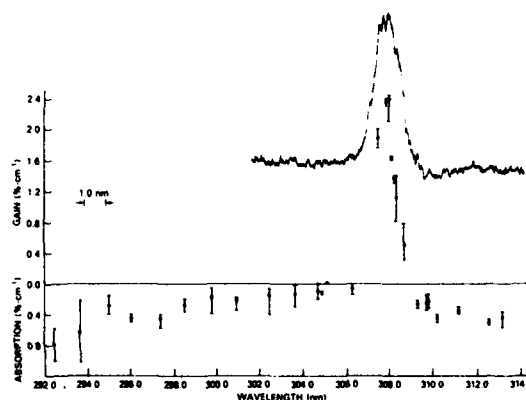


FIG. 1. Measured gain and absorption as a function of wavelength for a 1- μsec optical pulse.

^{a)}Present address: Science Applications, Inc., Arlington, Va. 22205.

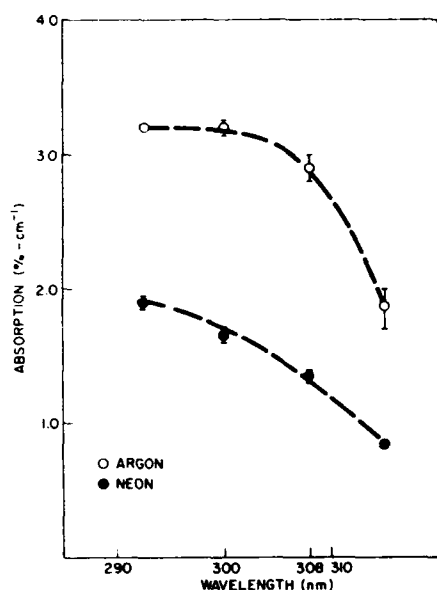


FIG. 2. Measured absorption as a function of wavelength in pure argon and neon plasmas.

fluorescence spectrum is superimposed on the gain absorption data. A weak secondary-emission band centered about 340 nm was also observed. This emission is attributed to the $C \rightarrow A$ band of XeCl . This secondary emission is weaker than the equivalent $C \rightarrow A$ emission in XeF .^{6,7}

The laser constituents were examined separately to determine the various contributions to the relatively large observed absorption in the laser mixture. Figure 2 plots the absorption in pure argon and pure neon as a function of wavelength. In this experiment the current density incident to the active volume was 6.5 A cm^{-2} . The energy deposited into each rare gas was kept comparable by varying the total pressure. In argon the absorption was broadly peaked over a region from 292 to 300 nm and at the laser wavelength it was $2.9\% \text{ cm}^{-1}$. In neon, absorption increased with decreasing wavelength. At the laser wavelength the transient absorption was $\sim 1.5\% \text{ cm}^{-1}$. While the measured absorption in pure neon plasmas was only one-half that of argon, it was still large.

Figure 3 plots the absorption of 308-nm radiation in argon-xenon and neon-xenon mixtures. A reduction in absorption at the laser wavelength was observed when small amounts of xenon were added to both argon and neon. In the neon case, the reduction in absorption was much greater. For both argon and neon diluents the absorption increased as the xenon concentration was increased, indicating that a new absorbing species involving xenon was introduced. The minimum measured absorption in neon-xenon mixtures at 308.0 nm was $\sim 0.25\% \text{ cm}^{-1}$. This minimum was observed for xenon concentrations ranging from 0.2 to 1.5%. Measurable increased absorption was observed for xenon concentrations $\sim 3.0\%$. For the XeCl laser, the optimum xenon con-

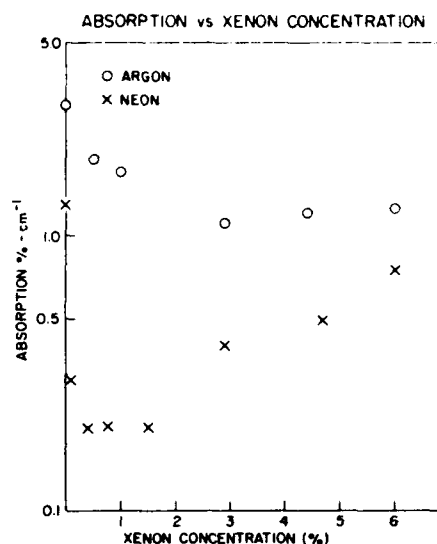


FIG. 3. Measured absorption at 308.0 nm in both argon and neon as a function of xenon concentration.

centration (1%) for best laser performance falls well within this minimum region. Thus, the laser performance is not limited by the amount of xenon which can be added. At 351.1 nm, a minimum measured absorption of $0.2\% \text{ cm}^{-1}$ was observed for xenon concentrations of $\sim 0.1\%$. For xenon concentrations $> 0.2\%$, absorption increased sharply. Previously, we have shown that the increase in absorption at 351.1 nm is attributed to the dimer ion, Xe_2^+ .^{1,11} Theoretical calculations^{8,9} predict that the absorption by Xe_2^+ is lower at

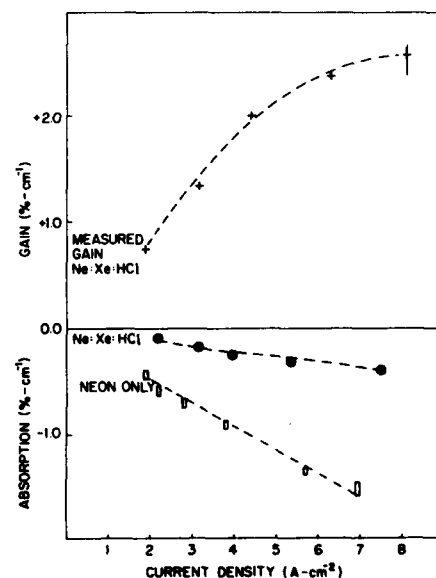


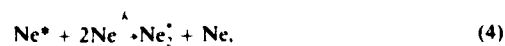
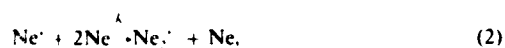
FIG. 4. Measured gain at 308.0 nm and absorption in XeCl laser mixtures as a function of current density incident to the active volume.

308.0 nm than at 351.1 nm. Thus, the correlation between xenon concentration and Xe_2^+ absorption is not as strong at 308.0 nm as it is at 351.1 nm.

Figure 4 plots the measured gain and absorption in optimized Ne/Xe/HCl mixtures and absorption in pure neon as a function of current density incident to the active volume. The optimum total pressure for the laser was 4 atm. The measured gain increased with increasing current and reached a peak value of $\sim 2.6\%$ cm^{-1} at the highest pumping currents. The measured absorption in both laser mixture and in the pure neon plasma increased linearly with current density. In both cases the absorption approached zero as the current density approached zero. When the optimum concentration of HCl (0.067%) was added to the optimum concentration of neon and xenon (98.93 : 1.0), no significant reduction or increase in absorption was observed.

The observed absorption in pure neon plasmas was broad banded (Fig. 2), increased linearly with increased electron-beam pumping current (Fig. 4), and was greatly reduced when small amounts of xenon (0.2%) were added (Fig. 3). Numerical models of pure neon-xenon mixtures show that the only species whose number densities follow the experimentally observed absorption as a function of pumping current and xenon admixture are the electronically excited atoms (Ne^*) and the excited dimers (Ne_2^+). Since the absorption is broadband, the absorber must be the dimer. When xenon is added to the mixture the excited neutral species are removed through the mechanisms of Penning associative ionization. Although the dimer ion (Ne_2^+) absorption is also broadband, the predicted reduction in its density when xenon is added is much smaller than the observed reduction in absorption. One would expect Ne^* and Ne_2^+ to be removed by charge-transfer reactions with xenon. However, the reaction rate constants for these processes are small ($< 10^{-11}$ cm^3/sec),¹⁰ and thus they have little effect on the dimer-ion concentration. The dimer-ion concentration does drop slightly due to the increased electron concentration resulting from Penning ionization of xenon. In addition, the model predicts a less than linear dependence on pumping current for the Ne_2^+ number density.

The dependence of the number densities of Ne_2^+ and Ne^* on electron-beam pumping current can be estimated by considering the dominant reactions involved in production and loss of Ne_2^+ and Ne^* :



These reactions are described by the following differential equations:

$$\frac{d[\text{Ne}^*]}{dt} = S - k_1[\text{Ne}^*][\text{Ne}]^2, \quad (6)$$

$$\frac{d[\text{Ne}_2^+]}{dt} = k_1[\text{Ne}^*][\text{Ne}]^2 - k_2[e][\text{Ne}_2^+], \quad (7)$$

$$\frac{d[\text{Ne}^*]}{dt} = k_2[e][\text{Ne}_2^+] - k_3[\text{Ne}^*][\text{Ne}]^2, \quad (8)$$

$$\frac{d[\text{Ne}_2^+]}{dt} = k_3[\text{Ne}^*][\text{Ne}]^2 - A[\text{Ne}_2^+]. \quad (9)$$

S is the electron-production rate from the high-energy electron beam, e is the electron number density, and A is the spontaneous emission coefficient. At these pressures $[\text{Ne}_2^+] \gg [\text{Ne}^*]$; thus, $[e] \approx [\text{Ne}_2^+]$. For the steady-state conditions, Eqs. (6) and (7) reduce to

$$S \propto [\text{Ne}_2^+]^2, \quad (10)$$

and Eqs. (6) through (9) yield

$$S \propto [\text{Ne}_2^+]. \quad (11)$$

These two equations show that the dimer-ion density increases as the square root of the current while the excited dimer increases linearly with current.

Although the foregoing analysis is based on some simplifying assumptions, conclusions drawn from the detailed calculations of the kinetic model are in substantial agreement.

In comparing gain and absorption data for the XeCl laser with that of the XeF laser there are some similarities. The background absorption in neon plasmas is large at both wavelengths. This background absorption is significantly reduced when xenon is added to neon. However, in marked contrast to the XeF laser, the addition of the halogen donor (HCl) does not reduce the background absorption. Also, in XeCl laser mixtures this background absorption is observed to increase with increasing current. Although the background absorption for the XeCl laser is much greater than that observed for the XeF laser, the small signal gain for the XeCl laser is also much greater. The absorption present in Ne/Xe mixtures is either not removed when HCl is added or is replaced by another absorbing species for which HCl is the precursor.

The authors gratefully acknowledge the many helpful discussions with R. Burnham and the technical assistance of K. Tayman and D.M. Shores.

I. F. Champagne, Appl. Phys. Lett. **33**, 523 (1978).

I. F. Champagne, J. G. Eden, N. W. Harris, N. Djou, and S. K. Searles, Appl. Phys. Lett. **30**, 160 (1977).

I. F. Champagne and N. W. Harris, Appl. Phys. Lett. **31**, 513 (1977).

M. Rokni, J. H. Jacob, and J. A. Mangano, Appl. Phys. Lett. **32**, 622 (1978).

T. G. Finn, I. J. Palumbo, and I. F. Champagne, Appl. Phys. Lett. **33**, 148 (1978).

D. Kligler, H. H. Nakano, D. L. Heustis, W. K. Bischel, R. M. Hill, and C. K. Rhodes, Appl. Phys. Lett. **33**, 39 (1978).
T. G. Finn (private communication).
Willard R. Wadt, David C. Cartwright, and James S. Cohen, Appl. Phys. Lett. **31**, 672 (1977).

H. H. Michels and R. H. Hobbs, 30th Annual Gaseous Electronics Conference, Palo Alto, Calif. 1977, paper BA-2 (unpublished).
R. Johnson, J. MacDonald, and M. A. Biondi, J. Chem. Phys. **68**, 2992 (1978).

Transient Absorption in Electron-Beam Excited Rare Gases at XeF Laser Wavelengths

Transient absorption experiments in pure and mixed rare gases were performed at the XeF laser wavelength using a broadband probe technique. The major absorbing species in this region are identified. There is a strong broadband absorption in electron-beam excited argon which is due to Ar_2^+ . In neon plasmas the broadband absorption is much weaker. However, there are a number of strong line absorptions due to Ne (3s-4p) transitions, one of which coincides with the 351 nm emission band of the XeF laser. Addition of xenon reduces Ne* absorption. The amount of xenon used is limited by the formation of Xe_2^+ which is also a strong absorber in the 350 nm region.

Transient absorption in e-beam excited rare gases has been recognized as a serious disadvantage to the development of high energy lasers as it lowers the laser extraction efficiency and limits scalability. Absorption studies in both uv and visible regions of the spectrum have been reported using either single wavelength or continuously tunable laser probe techniques.¹⁻⁶ Since e-beam excited rare gases are used as high energy storage media for several lasers, an understanding of the absorption phenomena in addition to measuring absorption is highly desirable. This requires the identification of the transient absorbing species which may include excited atoms, excited dimers and dimer ions depending on the wavelength region of interest and the rare gases used.

Theoretical calculations⁷ indicate that all rare gas dimer ions have a broad absorption spectrum in the uv and visible regions with the positions of the absorption peaks shifting to longer wavelengths for the heavier rare gases. Hence, it is not unusual to find more than one excited state specie responsible for absorption at any given wavelength. The concentrations of these absorbers are also expected to change with e-beam current density, pressure and temperature. Therefore, an absorption measurement at a single wavelength, though quantitative, provides limited information about the absorbers themselves. A wider spectral region must be probed in order to better characterize these transient absorbers. In this paper we report the application of a broadband probe technique to study transient absorption in the 330-360 nm region in e-beam excited rare gases under long pulse operation. This technique offers a significant amount of information in a single pulse, allowing one to study broadband absorption and line absorption simultaneously and to determine the relative contribution of all species as a function of wavelength. Our

investigations include e-beam excited pure Ne, Ar, Xe as well as Ar/Xe and Ne/Xe mixtures. Absorption characteristics relevant to electron-beam pumped XeF laser operation will be discussed.

The experimental apparatus was a 1-meter laser chamber used previously for gain and absorption measurements.³ Electron beam pulses of 1 μ sec duration and variable current density from 2 to 8 A cm⁻² were delivered to the gas at 300K. The probe source was the broadband dye emission (330-360 nm) of p-terphenyl in ethanol pumped by a coaxial xenon flashlamp (Phase-R Corp. Model DL-2100-CXH). The optical pulse, ~ 0.5 μ sec (FWHM), was synchronized with the e-beam pulse to probe the excited gas at the peak of the beam current. The wavelength integrated dye emission intensity signal monitored by a S-5 photodiode and the current pulse were monitored on a dual-beam oscilloscope for each shot. The dye emission passed through the 1-meter long cell. The output spectrum was photographed on Kodak Tri-X Pan film using a Minuteman 0.5 meter spectrometer with a 1200 grooves/mm grating blazed at 2000 Å (~ 3 Å resolution). In recording the absorption spectrum, a single shot provided adequate exposure on the film. In order to properly compare absorption in e-beam excited rare gases, one of the criteria of these measurements is that the pressure of the rare gases was varied such that energy deposition in the gas in each case was comparable.

The absorption spectra of e-beam excited pure neon at 4 atm are shown in Fig. 1. Comparison of the dye emission spectrum with and without e-beam excitation revealed numerous line absorptions superimposed on a weak broadband absorption. The line absorptions are attributed to known transitions out of the low-lying excited 3P_1 and 3P_2 states of Ne. At low e-beam pumping currents, distinct line absorption features were observed.

With increased pumping, some line features were no longer apparent as absorption appeared in regions between the atomic lines. The observed absorption characteristic was indeed transient and was not observed 1 μ sec after the current pulse. Of particular concern to the XeF laser operation is the presence of neon line absorption at 3510.7 Å. This lies close to the $v' = 0 \rightarrow v'' = 2$ transitions of XeF at 3512 Å and coincides with the $1 \rightarrow 4$ transition at 3510.8 Å. With equal energy deposited in 2 atm of pure argon, the absorption spectrum showed a much more severe broadband absorption than neon with few weak line features because there are no Ar lines with large oscillator strengths in this region. The time behavior and the increased absorption with pumping current were, however, the same as in the neon case.

The addition of a small quantity of xenon to neon significantly altered the absorption characteristics as illustrated in Fig. 2. The microdensitometer tracings are those of the dye emission spectrum with and without e-beam excitation of the rare gases. With 0.2% Xe in 4 atm of Ne (middle), the Ne line absorption features were greatly reduced and a small reduction in the broadband absorption was observed as compared to the pure Ne case (top). With Xe concentration increased to 2% (bottom), all Ne line features were removed and an increase in the broadband absorption appeared. In the case for pure Xe (bottom), comparable energy was deposited into 467 torr of Xe. The excited Xe plasma exhibited strong broadband absorption in this wavelength region, much more so than even in the argon case. The effect of adding xenon to 2 atm of argon is much less dramatic. Little or no change occurred in the absorption spectrum with xenon concentration up to 1%. Again, as Xe concentration was further increased, the absorption spectrum began to resemble that in Fig. 2 (bottom).

The long pulse XeF laser was initially operated with electron beam excitation of Ar/Xe/NF₃ gas mixtures⁸ and the diluent gas argon was later replaced by neon.³ This substitution resulted in increased extraction efficiency and the improvement was attributed to reduction of the transient absorption within the laser medium.³ With the help of a kinetic model, Finn et. al.⁹ examined these absorption measurements³ conducted in pure Ne, Ne/Xe mixtures and the laser mixtures. They conclude that Ne₂^{*} is most likely the major absorber in pure Ne plasma and under-optimum laser conditions Xe₂⁺ is the dominant absorber. In light of our present observations, the relevance of the diluent gas (Ne versus Ar) and the effect which the admixture gas (Xe) has on absorption in the XeF laser operation can be better understood.

The results of recent absorption measurements^{3,10} are shown in Fig. 3. Our present observations agree well with these measurements on a qualitative basis. At 3511 Å the absorption in pure Ne plasma actually exceeds that in argon. This is due to the strong Ne^{*} line absorption present at 3510.7 Å. However, the addition of xenon has a very different effect on each diluent gas. Up to 1% of Xe addition to argon, the absorption at 3511 Å is essentially unchanged from the value measured in pure argon. In contrast, the addition of 0.2% of Xe to neon sharply reduced the absorption and this is due to the reduction of Ne^{*} absorption mainly, as illustrated by the changes in absorption spectra in Fig. 2. Reduction of Ne^{*} is most likely a result of Penning ionization of Xe by Ne^{*} but the Xe interception of Ne^{*} formation via dissociative recombination of Ne₂⁺ should also be considered. Further increase of xenon concentration in neon resulted in a gradual increase in absorption. Our absorption spectra indicated that under these circumstances the Ne^{*}

absorption was completely removed but the broadband absorption increased. The latter is associated with the increase in formation of Xe_2^+ .

So far, we have been concerned with the 3511 Å output of the XeF laser. The other band at 3532 Å is the $v' = 0 \rightarrow v'' = 3$ transition. The 3511 Å emission is observed to be substantially weaker than that at 3532 Å in long pulse e-beam excited Ne/Xe/NF₃ laser mixtures.¹¹ The pure neon absorption spectrum in Fig. 2 (top) shows that there is no Ne* absorption at 3532 Å only a weak broadband absorption which is present over the whole spectral region investigated. At 0.2% Xe in Ne which is the optimum Xe concentration in XeF laser, the Ne* absorption at 3511 Å is reduced but not completely removed (see Fig. 2, middle). There still exists a difference in the amount of absorption present at the two wavelengths. Two absorbing species are found at 3511 Å but only one at 3522 Å. It is possible that the difference in emission intensity of the two bands could be accounted for by the difference in transient absorption. Since absorption in pure argon plasma is essentially broadband, the use of argon as the diluent will present comparable absorption at both wavelengths. This is consistent with the observation of comparable emission intensity from both bands in e-beam excited Ar/Xe/NF₃ mixtures.¹¹

The identification of absorbing species other than excited atoms is less straightforward. Nevertheless, based on theoretical calculations and experimental information accumulated so far, Ar_2^+ is mainly responsible for the broadband absorption in Ar/Xe/NF₃ mixtures over this wavelength region. The broadband absorption in Ne is likely to be due to Ne_2^+ even though ab initio calculations by Wadt et. al.⁷ indicate that Ne_2^+ absorption in 350 nm region is weak.

In summary, we have demonstrated the technique of using a broadband emission source to study the transient absorption in e-beam excited rare gases. This technique is limited only by the spectral range of the spontaneous dye emission. Neon is a significantly better diluent gas for the XeF laser than argon because the broadband absorption is weaker and the Ne* line absorption is lowered in the presence of xenon. One of the reasons why the Xe concentration in the XeF laser must be kept low is because of the strong correlation between Xe and Xe_2^+ formation and the large absorption cross section of Xe_2^+ at this wavelength.

We wish to thank Dr. J. R. McDonald of the Naval Research Laboratory for the loan of the dye laser and Dr. C. Brown of the Naval Research Laboratory for the use of the microdensitometer. We are also grateful to D. M. Shores and K. Tayman for their technical assistance. R. S. F. Chang thanks the National Research Council for an NRC-NRL postdoctoral award.

References

1. E. Zamir, D. L. Huestis, D. C. Lorents and H. H. Nakano in Electronic Transition Lasers II, edited by L. E. Nelson, S. N. Suchard and J. I. Steinfeld (MIT Press, 1977).
2. A. M. Hawryluk, J. A. Mangano and J. H. Jacob, Appl. Phys. Lett. 31, 164 (1977).
3. L. F. Champagne and N. W. Harris, Appl. Phys. Lett. 31, 513 (1977); L. F. Champagne, L. J. Palumbo and T. G. Finn, Appl. Phys. Lett. 34, 315 (1979).
4. R. O. Hunter, J. Oldenettel, C. Howton and M. V. McCusker, Final Technical Report, February 1977-November 1977, Maxwell Laboratories (unpublished).

5. J. B. West and W. H. Long, Jr., J. Chem. Phys. 70, 3457 (1979).
6. E. Zamir, D. L. Huestis, H. H. Nakano, R. M. Hill and D. C. Lorents, IEEE, J. Quantum Electron., QE-15, 281 (1979).
7. W. J. Stevens, M. Gardner, A. Karo and P. Julienne, J. Chem. Phys. 67, 2860 (1977); W. R. Wadt, D. C. Cartwright and J. S. Cohen, Appl. Phys. Lett. 31, 672 (1977).
8. L. F. Champagne, J. G. Eden, N. W. Harris, N. Djeu and S. K. Searles, Appl. Phys. Lett. 30, 160 (1977).
9. T. G. Finn, L. J. Palumbo and L. F. Champagne, Appl. Phys. Lett. 33, 148 (1978).
10. L. F. Champagne, Appl. Phys. Lett. 35, 516 (1979).
11. L. F. Champagne (unpublished).

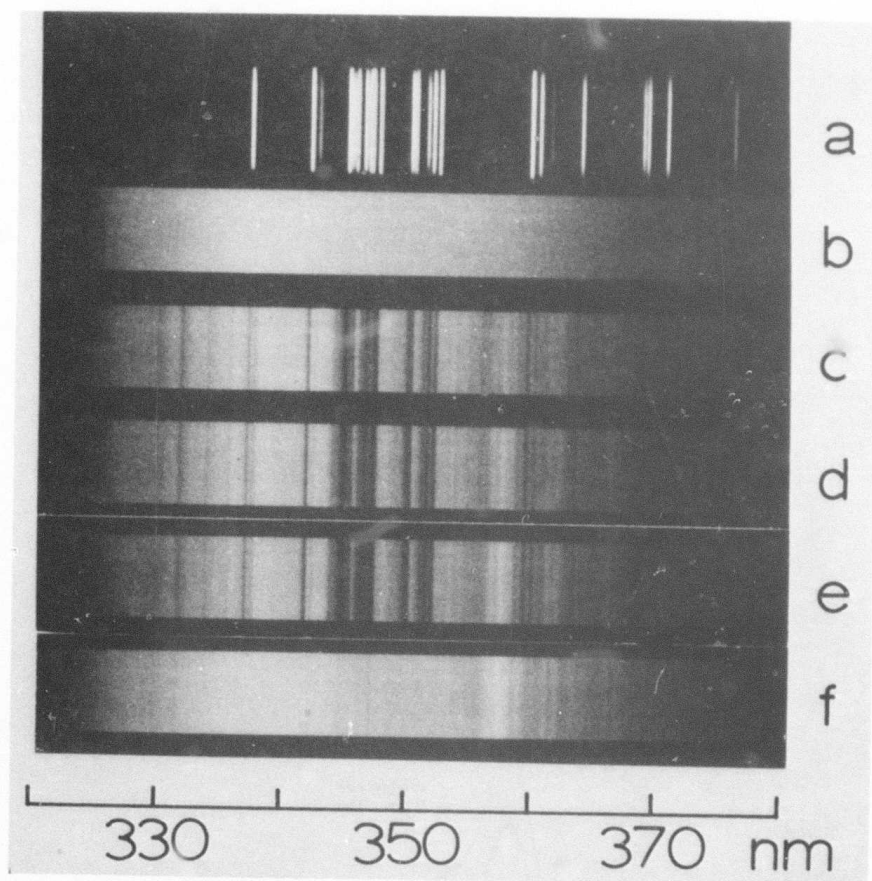


Figure 1. Absorption spectra of electron beam excited pure Ne at 4 atm. (a) Ne atomic spectra for calibration; (b) Dye emission spectrum without e-beam excitation of Ne; (c, d and e) Dye emission spectra with e-beam excitation at 3.8, 5.0 and 7.6 A cm⁻² respectively; and (f) 1 μ sec after e-beam current pulse.

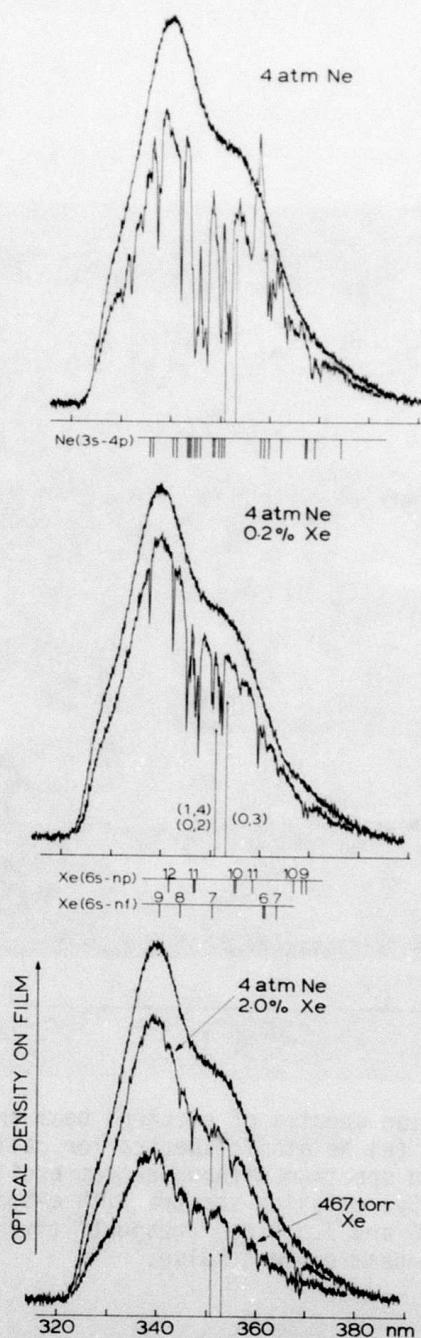


Figure 2. Microdensitometer tracings of the transient absorption spectrum as a function of Xe concentration in 4 atm of Ne at 7 A cm^{-2} . In each case, the top and smoother trace represents the dye emission spectrum without the excitation of the rare gases. The XeF (B-X) lasing transitions are indicated by $v' - v''$.

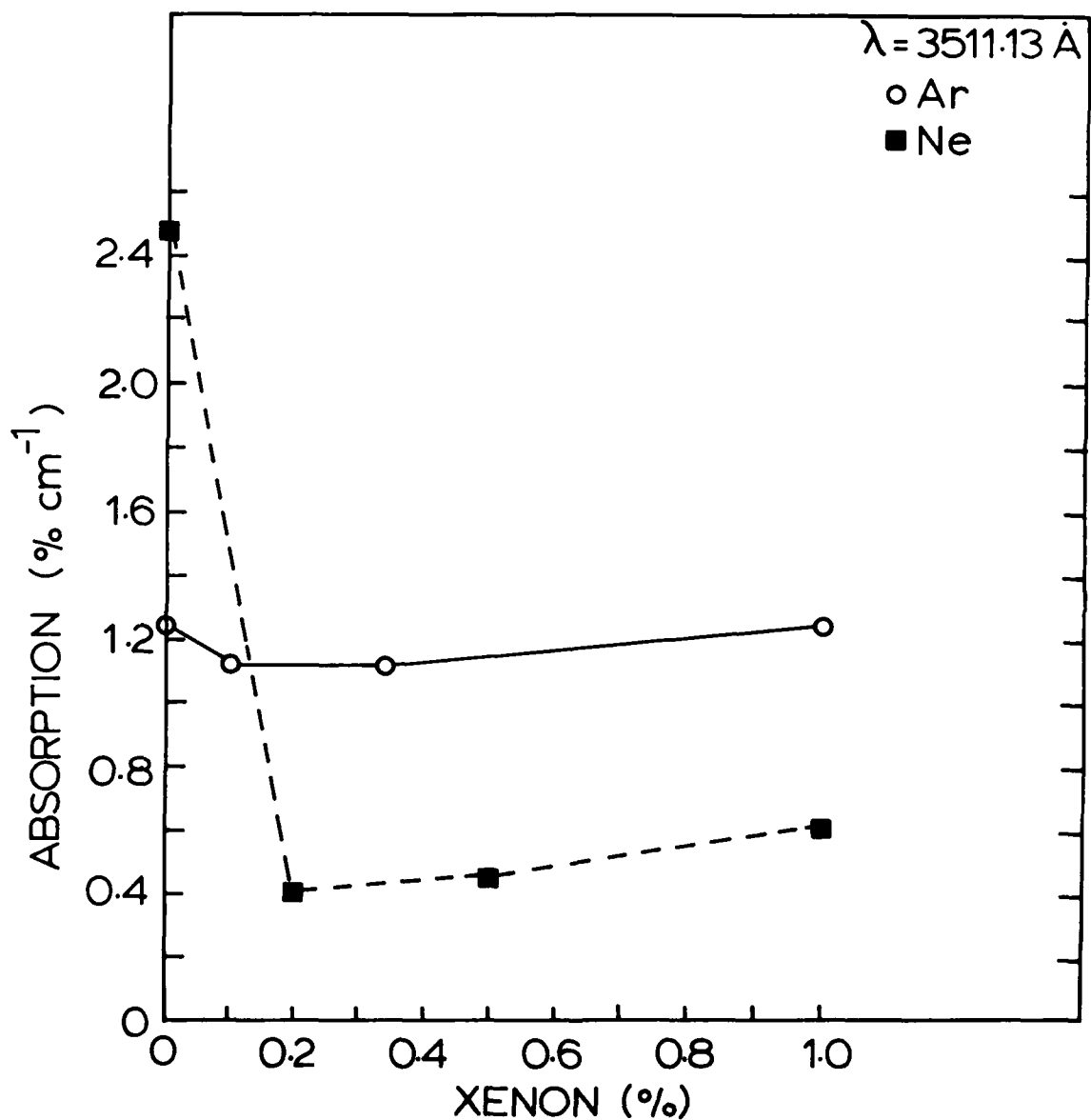


Figure 3. Measured absorption at 3511 Å in both Ar and Ne as a function of Xe concentration at 7 Å cm⁻². The Ar and Ne pressures were kept at 2 and 4 atm respectively.

Temperature Dependent Absorption Processes in the XeF Laser

During the past year, experiments were undertaken to compliment the existing data base on heated XeF laser performance. The results of these experiments provide both a better understanding of those physical processes which contribute to the improved performance of the XeF laser as a function of temperature and information by which further improvements to the laser may be made.

Previously, improved performance at elevated temperature was attributed to changes which occur within the laser species itself rather than in the laser medium. This improvement was attributed to both an improved relaxation of the vibrational manifold of the upper laser level as well as to improved dissociation of the lower laser level. The increased population in the $v' = 1$ and $v' = 0$ combined with a net decrease in population of the lower vibrational manifold especially levels $v'' = 2, 3$ and 4 would result in a greater population inversion. However, several experimental observations do not support this theory.

With ambient heating (to 175°C) there was a dramatic improvement in the stimulated emission at 351 nm $[(1,4), (0,2)]$ but a decrease in stimulated emission was observed at 353 nm $(0,3)$.^{1,2} Also, any improvement in the vibrational relaxation of the upper manifold as a function of temperature should be accompanied by an increase in the net spontaneous emission from the upper laser level. This was not observed.^{1,3} Dissociation of the lower laser level would not necessarily result in a change in the net spontaneous emission but should effect both the 351 nm emission band and 353 nm emission band equally. Attempts to attribute improved performance of the laser to changes within the laser species itself were further complicated by the observation that

the relative spontaneous emission between 351 nm and 353 nm measured via side fluorescence was not observed to change significantly as a function of temperature.^{1,3} This was in marked contrast to the observed stimulated emission as a function of temperature.^{1,2} By performing transient absorption and axial fluorescence measurements as a function of temperature changes within the laser medium itself could be observed. The results of these experiments combined with the previous experimental observation yield a consistent explanation as to why the electron beam pumped XeF laser works better at elevated temperature.

Transient absorption studies were made using two different probing techniques; single wavelength probing and broad band probing. The results of single wavelength probing using the rare gas ion laser are detailed below.⁴ Briefly, we find that in pure neon plasmas there are two types of absorption present; a broad but weak band of absorption is observed, which increases with increasing temperature and a strong narrow band ($\sim 20 \text{ \AA}$) of absorption is observed around 351 nm. Moderate heating reduces this narrow band absorption. Improved performance of the XeF laser at elevated temperature is primarily due to a reduced absorption in the laser medium at 351 nm. The results of broad band absorption experiments in neon plasmas and mixed rare gases as well as axial fluorescence measurements in Ne/Xe/NF₃ mixtures support these conclusions.

Figure 1 represents typical data taken in pure neon plasmas with the broad band probing technique. A neon lamp was used to calibrate wavelength. The broad band probe source used was a dye emission from p-terphenyl in ethanol with an emitting region from 330 to 360 nm. Transient absorption while the discharge was on was observed at three pumping currents; 3.8 A-cm^{-2} , 5.0 A-cm^{-2} and 7.6 A-cm^{-2} . This pumping current was incident to the active volume. Spontaneous emission in this wavelength region from the neon plasma

was small. Time resolved absorption at .2 μ sec and one microsecond was also observed. At low pumping currents we observed strong narrow line absorption in pure neon plasmas throughout the probed region. As the pumping current was increased the line absorption became less pronounced and absorption between these lines increased. At high pumping current a band of absorption was observed. These absorption lines coincide exactly with the atomic transitions of neon shown with the neon lamp. There are three atomic transitions in neon between the 3s and 4p states centered at 3510.7, 3515.2 and 3520.5 Å.⁵ This absorption band coincides with the (1,4) and (0,2) vibrational band of the B \rightarrow X transition of XeF @ 351 nm.⁶ This absorption band is superimposed on a weak but broad band of absorption which extends over the entire probing region. The weak broad band of absorption which increased with increasing pump current is attributed to the dimer ion Ne₂⁺.

Figure 2 superimposes two microdensitometer traces from the broad band probe source. Broad band emission from the probe source is compared under two conditions; one with the electron beam exciting 4 atm of neon and one without excitation. With the discharge on we observe strong narrow bands of absorption superimposed on a weaker but broad band of absorption which extends over the entire region. One strong narrow band of absorption coincides with the 351 nm emission band of the XeF laser but there is no correspondingly strong band of absorption at 353 nm.

Figure 3 plots typical data in pure neon plasmas as a function of temperature. The neon lamp was used to calibrate wavelength. Transient absorption is observed at different temperatures. As the temperature is increased, the absorption lines become more pronounced. This is attributed to an overall reduction in the strong narrow band of absorption in the 351 nm

region especially between the lines. The broad background absorption increases slightly with increasing temperature.

In order to compare temperature-dependent changes in the laser medium to those temperature-dependent changes associated with the laser species itself, axial fluorescence measurements were made and the results compared with side fluorescence measurements made elsewhere.^{1,3}

Axial fluorescence is a measure of the spontaneous emission in the presence of absorption along the optical axis. Side fluorescence minimizes the effects of absorption.

Two temperature effects were observed with axial fluorescence measurements. At room temperature, the spontaneous emission at 351 nm was less intense than 353 nm emission for pumping currents in the range from 2-7 A-cm⁻². But at 150°C the relative intensity of the two spontaneous emission bands were comparable in this pumping current range. Also, the net spontaneous emission decreased with increasing temperature. Figure 4 is the axial emission spectra for optimum neon-xenon NF₃ mixtures at two different pumping currents and two different temperatures. A neon pen lamp is used to calibrate wavelength. At both pumping currents net spontaneous emission along the optical axis decreased with increasing temperature. This contrasts with side fluorescence measurements in that neither the relative intensity of the two emission bands nor the net spontaneous emission was observed to change with temperature.^{1,3} This indicates that the broad band of absorption observed in neon plasmas is present in the laser mixture and just as in the case of the pure neon plasma this absorption increases with increasing temperature.

The reduced spontaneous emission along with optical axis at elevated temperatures is attributed to an increase in the weak broadband absorption. The

increased intensity of the 351 nm emission band with increasing temperature which is observed along the optical axis is attributed to a reduction of the strong narrow band absorption at 351 nm. The observation of no measurable increase in the net spontaneous emission with temperature in the absence of absorption indicates that the improved performance of the XeF laser with moderate heating is more likely due to a reduction in medium absorption than to increased energy extraction from the upper laser level. However, increased dissociation of the lower laser level would not result in an increase in net spontaneous emission.

That increased dissociation of the lower laser level can occur with moderate heating is generally accepted. However, the presence of a broad band of absorption due to Ne_2^+ and the observation that this absorption increases with increasing temperature tends to counteract any improvement in laser performance which ground state dissociation would otherwise provide. As a result of these two competing effects there will be an optimum ambient temperature for which the stimulated emission at 353 nm will reach a maximum value. At both lower and higher temperatures stimulated emission at 353 nm will be reduced from this peak value.

The results of both single wavelength probing and broad band probing experiments are in excellent agreement. Based on these results and axial fluorescence experiments we conclude that there are two types of absorption present in pure neon plasmas, a weak but broad band of absorption which is attributed to the dimer ion Ne_2^+ and a strong narrow band of absorption which is attributed to the atomic transitions in neon. The weak but broad band of absorption increases with increasing temperature but the strong narrow band of absorption decreases with increasing temperature. Both types of absorption are present in laser mixtures.

The improved performance in the XeF laser is primarily due to a reduction in the strong narrow band absorption at 351 nm when the laser mixture is heated. No experimental verification exists to support the contention that moderate heating will increase the vibrational relaxation of the upper laser level. The increase in the broad band absorption (Ne_2^+) at elevated temperature tends to counteract any improvement which would arise from increased dissociation of the lower laser level.

The observation of a strong narrow band of absorption in neon which coincides with the emission band at 351 nm at room temperature has implications for further improvement in the XeF laser. This information could be applied to experiments in which the XeF laser could be injection locked provided the absorption band does not completely overlap the emission band. Also, in an amplifier this narrow band of absorption could be saturated by an optical pump source of sufficient intensity.

References

1. J. C. Hsia, J. A. Mangano, J. H. Jacob and M. Rokni, Appl. Phys. Lett. 34, 208 (1979).
2. L. F. Champagne (unpublished).
3. K. Tang (unpublished).
4. L. F. Champagne, Appl. Phys. Lett. 35, 516 (1979).
5. Tables of Spectral Lines of Neutral and Ionized Atoms, edited by A. R. Striganov and N. S. Sventitskii (Plenum, New York, 1968).
6. J. Tellinghuisen, G. C. Tisone, J. M. Hoffman, and A. K. Hays, J. Chem. Phys. 64, 4796 (1976).

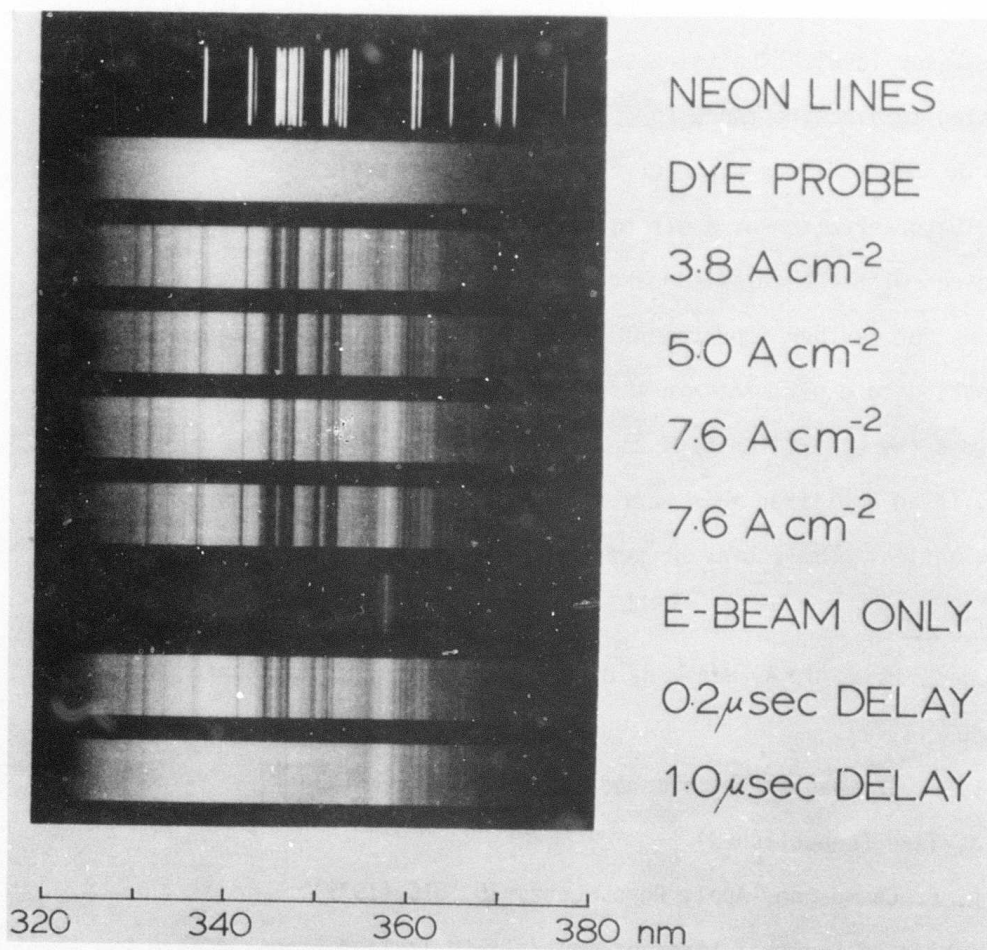


Figure 1. Absorption spectra of electron beam pumped neon plasma at 4 atm as a function of pumping current.

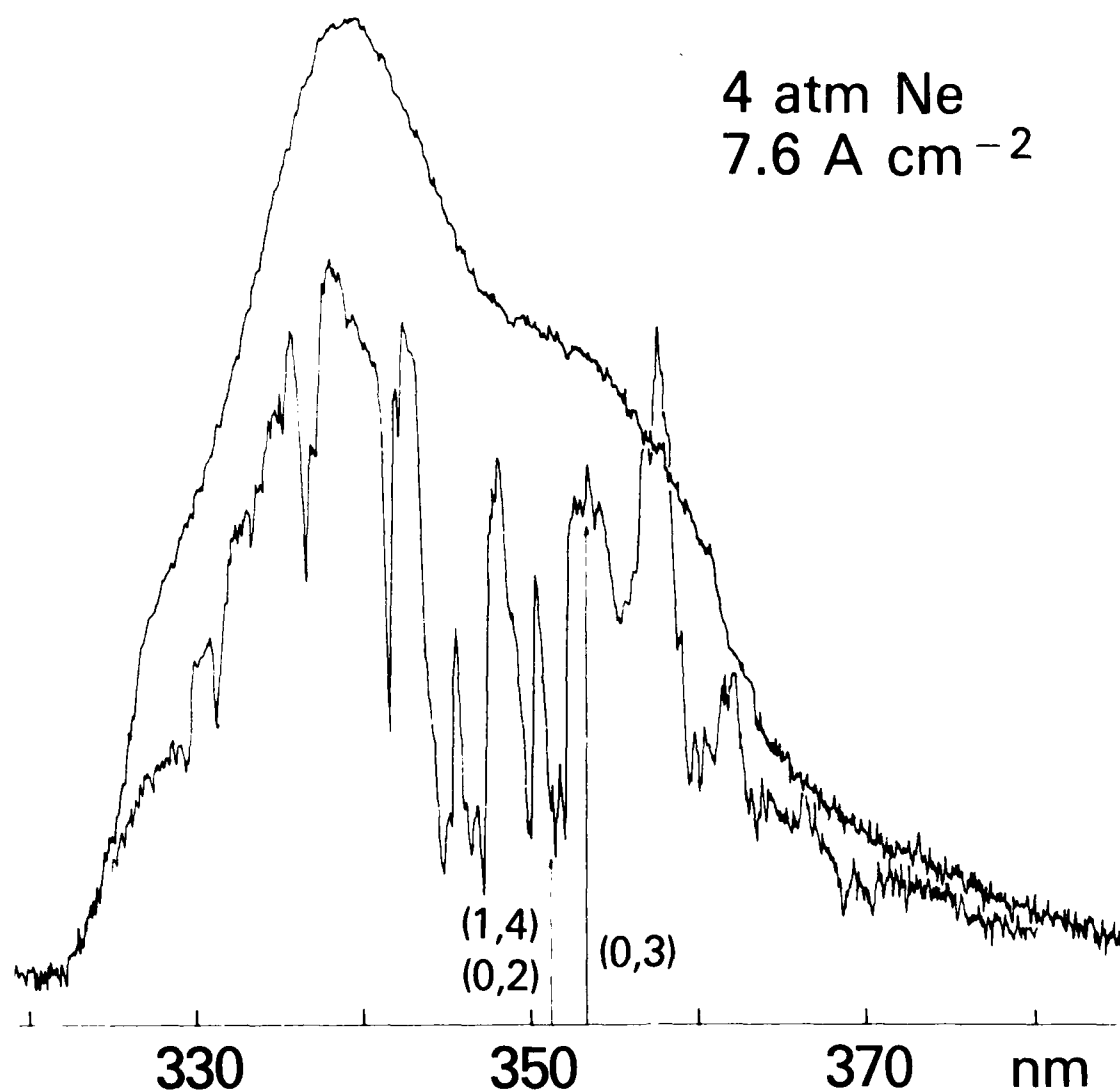


Figure 2. Microdensitometer traces of broad band probe source with and without transient optical absorption.

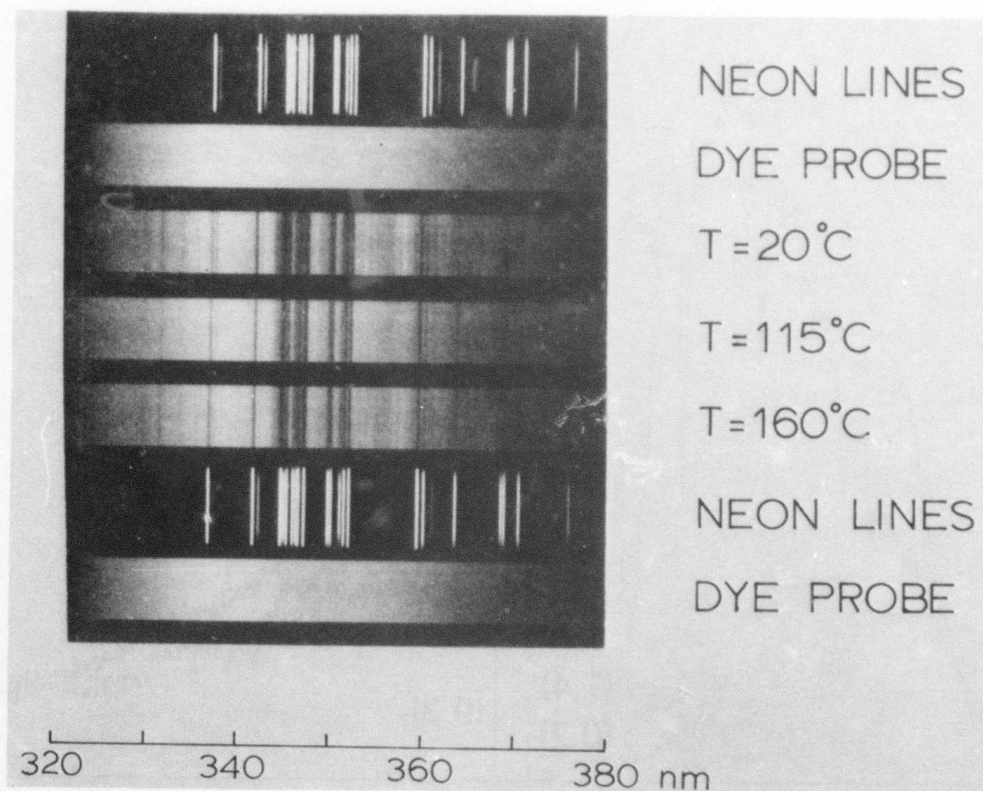


Figure 3. Absorption spectra of electron beam pumped neon plasma at 4 ama as a function of temperature.

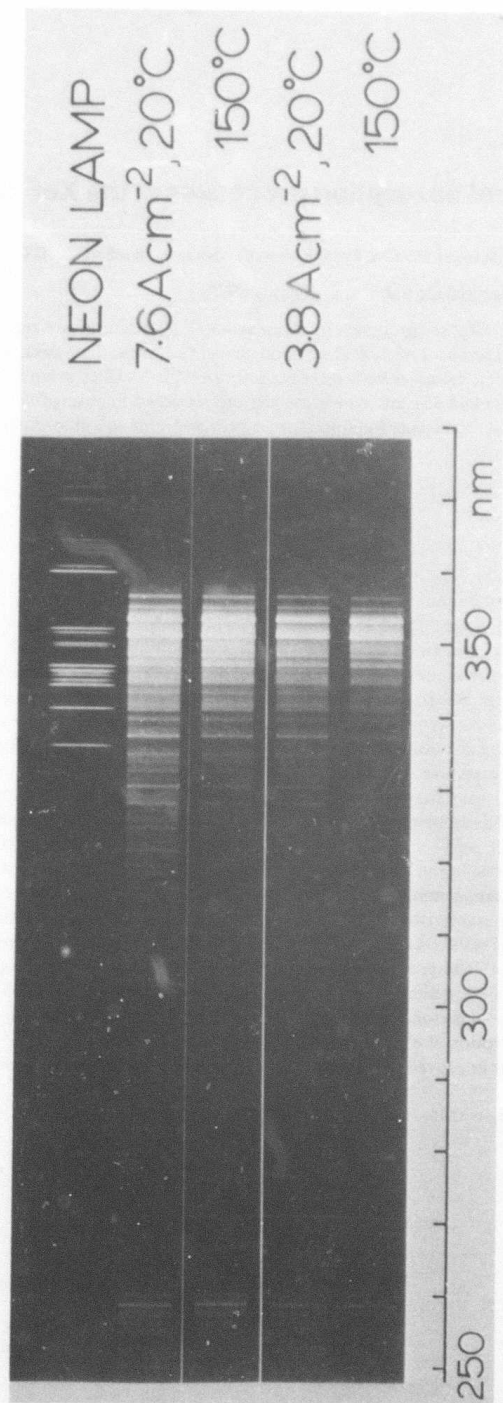


Figure 4. Axial spontaneous emission spectra in neon/xenon/NF₃ mixtures as a function of pumping current and temperature.

Temperature-dependent absorption processes in the XeF laser

L. F. Champagne

Laser Physics Branch, Optical Sciences Division, Naval Research Laboratory, Washington, D.C. 20375

(Received 11 June 1979; accepted for publication 31 July 1979)

Temperature-dependent absorption processes in neon/xenon/NF₃ mixtures are reported. In pure neon plasmas there are two types of absorption present; a broad but weak band of absorption is observed, which increases with increasing temperature, and a strong narrow band of absorption is observed around 351 nm. Moderate heating reduces this absorption. Improved performance of the XeF laser at elevated temperature is primarily due to reduced absorption in the laser medium at 351 nm.

PACS numbers: 42.55.Hq, 42.60.He, 42.60.By

For short pumping pulses (≤ 50 ns) by discharge,¹ proton beam,² or electron beam,³ the xenon fluoride laser is observed to emit on two distinct bands at 351.1 and 353.2 nm, independent of the diluent which is used. In each case the observed intensity from the two bands is comparable. For long-pulse electron beam pumping of argon/xenon/NF₃ mixtures, two-band emission is also observed.⁴ When neon is used as diluent and the laser mixture is pumped by an electron beam for times > 100 ns, the emission at 351 nm is observed to be substantially weaker than that observed at 353 nm.⁴ However, in the first 100 ns emission at 351 nm is comparable to emission at 353 nm.⁴

Recently, improved performance in the XeF laser has been observed when mixtures of neon, xenon, and NF₃ are heated to $\sim 175^\circ\text{C}$.⁴ One of the characteristics of this improved performance is the increased emission at 351 nm with increasing temperature. Presently, this improvement is attributed in part to increased energy extraction from the upper laser level and in part to increased dissociation of the lower laser level.^{4,5} Reduced absorption at elevated temperatures may also contribute to the improved performance.

In this letter we report the results of absorption studies as a function of temperature in the 351-nm region. Briefly, we observe two types of absorption in neon plasmas; a broad but weak absorption from 3378 to 3638 Å, and a strong band of absorption which coincides with the 351-nm emission band of the xenon fluoride laser. Addition of xenon and NF₃ does not completely remove this absorption at 351 nm but does remove it at 353 nm. Moderate heating reduces absorption in pure neon plasmas at 351 nm but increases it elsewhere, including 353 nm. Absorption in neon/xenon mixtures is lower at elevated temperatures than at room temperature. In the laser mixture, the measured small-signal gain at 351 nm increases by a factor of 2 when the temperature is increased from 20 to 150 °C but the small-signal gain at 353 nm is not a sensitive function of temperature.

The net spontaneous emission measured along the optical axis decreases with increasing temperature. Also, the relative emission intensity at 351 nm increases with respect to 353-nm emission as the temperature increases.

The laser chamber used in these experiments is essentially the same as that used previously.⁶ A current density of

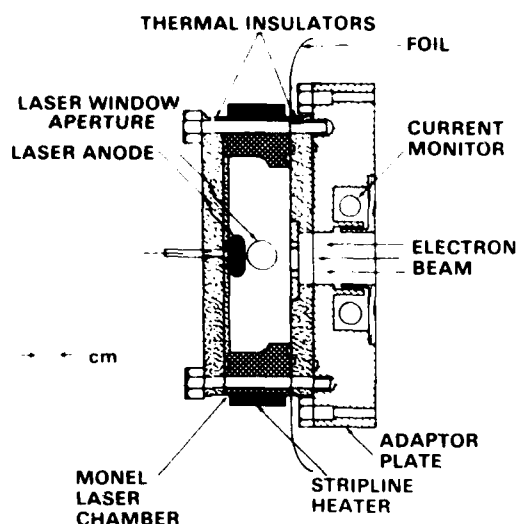


FIG 1 Schematic diagram of the laser cell. The cell can be operated over a temperature range 20–150 °C.

$\sim 7 \text{ A cm}^{-2}$ irradiated an active volume of 387 cm^3 . Pumping pulses were $1.2 \mu\text{sec}$ in duration. Some modifications were made to the laser cell in order to operate in the temperature range 20–150 °C (Fig. 1). The modifications included the addition of two stainless steel plates, which serve as thermal insulators, to house the monel laser chamber. Heating was provided by resistive stripline heaters positioned at the top and bottom of the laser chamber. The active length and volume was not changed. The current density incident to the

active volume was reduced by about 10% when the thermal insulator was placed between the primary electron beam and the laser chamber.

Both a rare-gas ion laser and flash lamp pumped dye laser were used to probe the discharge. The rare-gas laser was used to accurately reproduce well-known wavelengths. The flash lamp pumped dye laser was used to provide a profile of absorption in the region of interest. The wavelength of the dye laser could be accurately determined but retuning the dye laser to a specific wavelength was very difficult and was not attempted here. The output spectrum of the dye laser was monitored with a $\frac{1}{2}\text{-m}$ Minuteman monochromator. The monochromator was calibrated with a mercury pen lamp. The time resolved output from either probe laser was monitored before and after the laser chamber with S-5 photodiodes.

Figure 2 is a plot of the room-temperature profile of absorption in a pure neon plasma as a function of wavelength. In addition, absorption at $T \sim 150 \text{ °C}$ is plotted at two specific wavelengths: 3511.13 and 3542 Å. The pumping current incident to the active volume (7 A cm^{-2}) was experimentally equal to that used in pumping the optimum laser mixture at a total pressure of 4 amagats. Under these conditions the energy absorbed by the gas mixtures at the two different temperatures was comparable. Absorption measurements at accurately known wavelengths are denoted by + and ϕ . The absorption measurements taken with the flash lamp pumped dye laser are denoted by ■ and □. At room temperature, a broadband but weak absorption was observed in the region from 3378.3 to 3637.8 Å. Superimposed on this was an absorption of large amplitude, asymmetrical in shape, and approximately 20 Å (FWHM) wide.

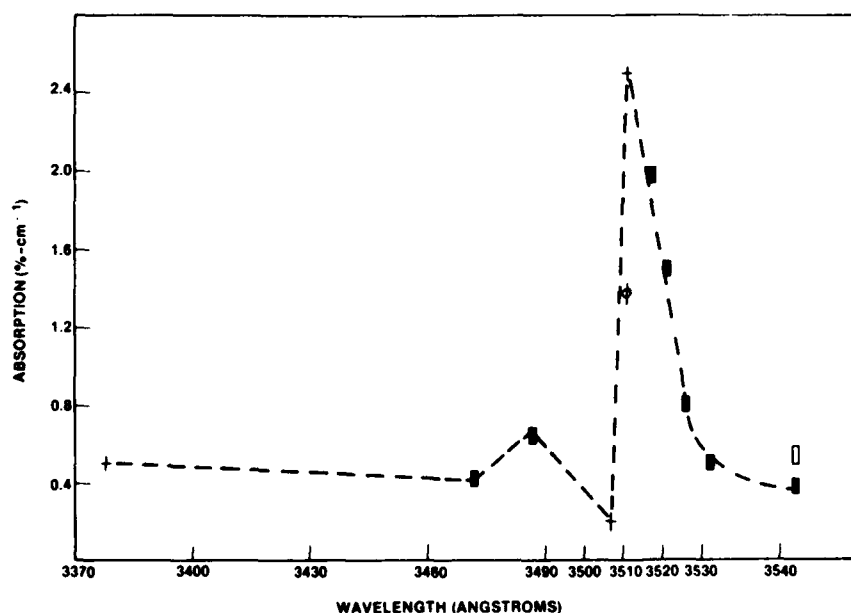


FIG. 2. Profile of transient absorption in neon plasma. Plot includes accurately known wavelengths (+) and several probe wavelengths generated by a flash lamp pumped dye laser (■). Absorption at $T \sim 150 \text{ °C}$ is plotted for two wavelengths (ϕ , □).

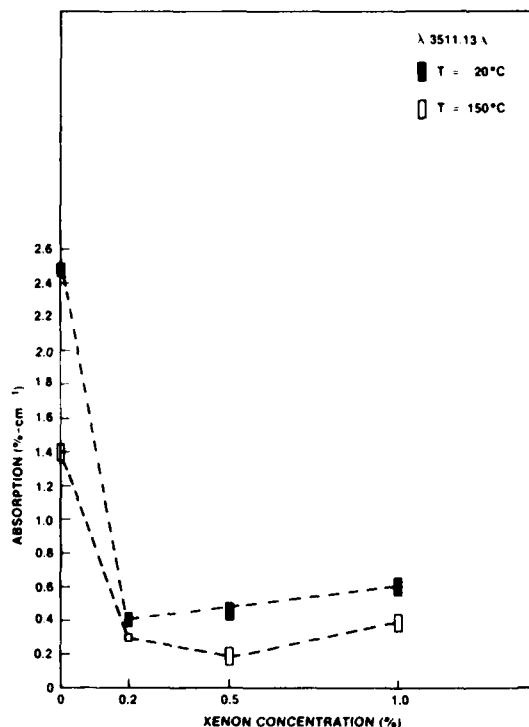


FIG. 3. Measured absorption at 3511.13 Å in neon as a function of xenon concentration at two different temperatures.

Probing with the krypton ion transition at 3507.4 Å, the measured absorption was $\sim 0.2\% \text{ cm}^{-1}$. Probing with the argon ion transition at 3511.13 Å, the measured absorption was $2.5\% \text{ cm}^{-1}$. Measured absorption at these two points defined a sharply rising absorption in the region from 3507.4 to 3511.1 Å. The dye laser was tuned to coincide with the 3532-Å output of the XeF laser. The measured absorption was $0.5\% \text{ cm}^{-1}$, which was experimentally equal to that observed at wavelengths well removed from the gain region (3378.3 and 3637.8 Å). When the dye laser was tuned over the region from 3532 to 3511 Å, the transient absorption gradually increased with decreasing wavelength. The weak but broad absorption which is observed in pure neon plasmas in this region of the spectrum is attributed to a dimer species¹¹ (Ne_2^+ or Ne_2^*) rather than an electronically excited atom (Ne^*) or ion (Ne^+). It was not possible to unambiguously determine whether the absorption increased linearly with current because the absorption was weak and the range over which the pumping current could be varied was limited. The observed peak absorption, while comparable in amplitude to that observed in argon plasmas at $\sim 3500 \text{ Å}$, is much narrower.¹⁰ However, the width, $\sim 20 \text{ Å}$ (FWHM), is much broader than is predicted for either pressure broadening or resonant broadening of a single atomic transition. There are three atomic transitions in neon between the 3s and 4p states centered at 3510.7, 3515.2, and 3520.5 Å.¹² This absorption band coincides with the (1,4) and (0,2) vibrational bands of the $B \rightarrow X$ transition of XeF at 351 nm.^{13,14}

When the pure neon was heated to 150 °C, the transient absorption at 3511.1 Å was reduced from 2.5 to $\sim 1.4\% \text{ cm}^{-1}$, while the absorption at 3542 Å increased slightly and the absorption at 3637.8 Å increased from 0.45 to $0.6\% \text{ cm}^{-1}$. The substantial reduction in absorption at 3511.1 Å is greater than can be accounted for by temperature broadening alone under these moderate heating conditions. When neon is heated from 20 to 150 °C, this 20-Å band of absorption either shifts slightly toward the visible region of the spectrum or is reduced, but the broader background absorption increases slightly. Although the absorption in neon plasmas is large at 3511.1 Å, it can be significantly reduced by adding xenon at either 20 or 150 °C as shown in Fig. 3.

In Fig. 3 all measurements were taken using the rare-gas ion laser tuned to 3511.1 Å. Optical absorption was observed to be lower in pure neon plasmas at elevated temperatures. When small concentrations of xenon were added to neon at either temperature the absorption was reduced further. At both temperatures, as the concentration of xenon was increased the optical absorption increased from its minimum value. At 150 °C the transient optical absorption in pure neon and neon-xenon mixtures was less than that observed at 20 °C. The amount of xenon which gives the minimum absorption at $T = 150 \text{ °C}$ is about twice that required to minimize absorption at room temperature.

The observed effect which temperature has on absorption is consistent with the predictions of Wadt.¹¹ This ab-

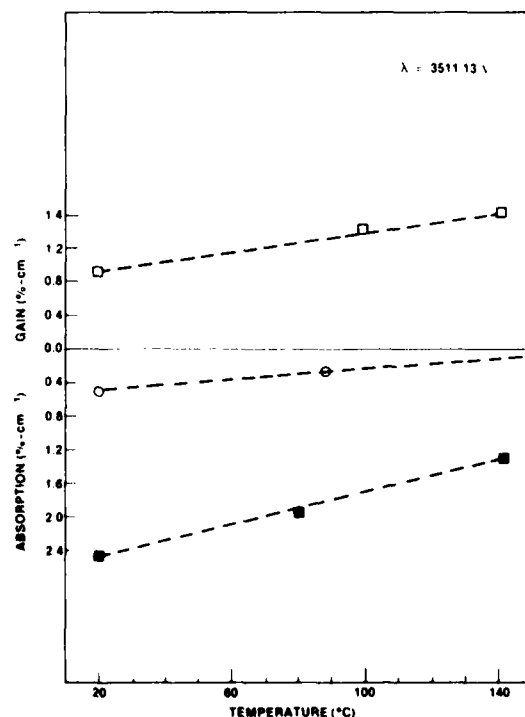


FIG. 4. Measured gain (□) in laser mixture at 3511.13 Å and absorption in pure neon (■) and optimum neon-NF mixtures (○) as a function of temperature.

sorption is attributed to the dimer ion Xe_2^+ .¹⁰ Theory predicts that the cross section for absorption by the dimer ion Xe_2^+ will be reduced by a factor of ~ 2 when the gas is moderately heated.

Figure 4 plots the measured gain for Ne/Xe/NF₃ mixtures and the absorption for both neon and neon/NF₃ mixtures at 3511.1 Å as a function of temperature. The amount of NF₃ used was 0.06%, a typical concentration for optimum laser performance. Total pressure was 4 amagats. Absorption in pure neon plasmas decreased linearly with increasing temperature and was reduced by a factor of 2 in going from 20 to 150 °C. When the optimum concentration of NF₃ was added to neon, the optical absorption was 0.5% cm⁻¹ at 20 °C and ≤ 0.1 cm⁻¹ at 150 °C. By contrast, at 3532 Å no measurable absorption in neon-NF₃ mixtures was observed at either temperature. At room temperature the measured gain at 3511.1 Å was $\sim 0.85\%$ cm⁻¹ and as the temperature was increased to 150 °C the measured gain increased to $\sim 1.45\%$ cm⁻¹. The measured gain at 353.2 nm was 1.7% cm⁻¹ at room temperature and ~ 1.790 at 150 °C. The optimum laser mixture for best performance did not change with temperature.

At room temperature, the absorption in neon is much larger at 351 nm than at 353 nm. Addition of xenon or NF₃ to neon eliminates this absorption at 353 nm but not at 351 nm. That the measured gain at 351 nm increases with temperatures indicates that either the real gain g_0 (measured gain less background absorption) is increasing, the transient absorption is decreasing, or a combination of these two effects occurs. This temperature-dependent change is confined to those vibrational bands which emit at 351 nm and does not affect the 353-nm emission band. In order to compare temperature-dependent changes in the laser medium to those temperature-dependent changes associated with the laser species itself, axial fluorescence measurements were made and the results compared with side fluorescence measurements made elsewhere.^{2,15}

Axial fluorescence is a measure of the spontaneous emission in the presence of absorption along the optical axis. Side fluorescence minimizes the effects of absorption.

Two temperature effects were observed with axial fluorescence measurements. The net spontaneous emission decreased with increasing temperature. Also, at room temperature, spontaneous emission at 351 nm was less intense than 353-nm emission for pumping currents in the range 2–7 A cm⁻². But at 150 °C, the relative intensity of the two spontaneous emission bands was comparable for these pumping currents. Observing the side fluorescence, Tang¹⁵ noted no measurable change in net spontaneous emission with temperature. Also, the relative intensity of the two emission bands was comparable and did not change with temperature.^{6,15}

The reduced spontaneous emission along with optical axis at elevated temperatures is attributed to an increase in the broadband absorption. The increased intensity of the 351-nm emission band with increasing temperature which is observed along the optical axis is attributed to a reduction of the strong narrow band absorption at 351 nm. The observation of no measurable increase in the net spontaneous emis-

sion with temperature in the absence of absorption indicates that the improved performance of the XeF laser with moderate heating is more likely due to a reduction in medium absorption than to increased energy extraction from the upper laser level. However, increased dissociation of the lower laser level would not result in an increase in net spontaneous emission.

In another experiment neon was replaced with argon as the diluent in an electron beam pumped XeF laser operated at room temperature for 1 μs. Stimulated emission of comparable intensity was observed on both bands. This result is consistent with the observation of a strong narrow band of absorption present in neon which coincides with the 351-nm emission band. It is not consistent to assume that dissociation of the lower laser level of the laser species occurs only at elevated temperatures when neon is used as diluent, but at room temperature when argon is used as diluent. The improved laser performance at elevated temperature is attributed primarily to a reduction in medium absorption rather than to processes which affect the lasing species.

In conclusion, there are two types of absorption processes present in neon/xenon/NF₃ mixtures. There is a weak but broad absorption which is attributed to either the dimer ion Ne_2^+ or the excited dimer Ne_2^* . This absorption increases with temperature. There is also a strong narrow band of absorption which coincides with 351-nm emission band in XeF. This absorption is attributed to the three atomic transitions in neon. This band of absorption is reduced or shifted with increasing temperature. Improved performance of the XeF laser at elevated temperature is attributed to a net reduction in absorption at 351 nm.

The author acknowledges useful discussions with R. Burnham, R. Chang, K. Tang, and T.G. Finn and is grateful to D.M. Shores and K. Tayman for their technical assistance.

¹R. Burnham, N.W. Harris, and N. Djeu, *Appl. Phys. Lett.* **28**, 86 (1976).

²J.G. Eden, J. Golden, R.A. Mahaffey, J.A. Pasour, and R.W. Waynant, *Appl. Phys. Lett.* **35**, 133 (1979).

³E.R. Ault, R.S. Bradford, Jr., and M.L. Bhaumik, *Appl. Phys. Lett.* **27**, 413 (1975).

⁴J.C. Hsia, J.A. Mangano, J.H. Jacob, and M. Rokni, *Appl. Phys. Lett.* **34**, 208 (1979).

⁵L.F. Champagne (unpublished).

⁶R.O. Hunter, J. Oldenettel, C. Howton, and K. Tang (unpublished).

⁷J.C. Hsia, J.A. Mangano, M. Rokni, A. Hauruk, and J.H. Jacob, 30th Annual Gaseous Electronics Conference, Palo Alto, California, 1977, Paper CA4 (unpublished).

⁸T.G. Finn, L.J. Palumbo, and L.F. Champagne, *Appl. Phys. Lett.* **33**, 148 (1977).

⁹L.F. Champagne, J.G. Eden, N.W. Harris, N. Djeu, and S.K. Searles, *Appl. Phys. Lett.* **30**, 160 (1977).

¹⁰L.F. Champagne and N.W. Harris, *Appl. Phys. Lett.* **31**, 513 (1977).

¹¹Willard R. Wadt, David C. Cartwright, and James S. Cohen, *Appl. Phys. Lett.* **31**, 672 (1977).

¹²*Tables of Spectral Lines of Neutral and Ionized Atoms*, edited by A.R. Strigantsev and N.S. Sventitskii (Plenum, New York, 1968).

¹³J. Tellinghuisen, G.C. Tison, J.M. Hoffman, and A.K. Hays, *J. Chem. Phys.* **64**, 4796 (1976).

¹⁴J. Goldhar, J. Dicke, L.P. Bradley, and L.D. Pleasance, *Appl. Phys. Lett.* **31**, 677 (1977).

¹⁵K. Tang (unpublished).

VISIBLE LASER STUDIES

Dissociative Excitation of HgBr_2 by Rare Gas Metastable Atoms and $\text{N}_2(\text{A}^3\Sigma_u^+)$

The dissociative excitation of HgBr_2 by rare gas metastable atoms and $\text{N}_2(\text{A}^3\Sigma_u^+)$ has been studied in a flowing afterglow apparatus. Reaction of HgBr_2 with the lighter rare gas (He, Ne and Ar) metastable atoms gave strong Hg^* line emissions. Intense HgBr ($\text{B } ^2\Sigma^+ \rightarrow \text{X } ^2\Sigma^+$) emission (300-513 nm) from Xe ($^3\text{P}_2$) and N_2 (A) reactions was observed. The rate constants for HgBr^* (B) formation from HgBr_2 excitation by Xe ($^3\text{P}_2$) and N_2 (A) were determined as $(5.3 \pm 1.5) \times 10^{-10} \text{ cm}^3 \text{ sec}^{-1}$ and $\geq 1 \times 10^{-10} \text{ cm}^3 \text{ sec}^{-1}$ at 350°K, respectively. Also, the formation rate constant for HgBr^* (C) from $\text{HgBr}_2 + \text{Xe } (^3\text{P}_2)$ was determined to be $(1.1 \pm 0.3) \times 10^{-10} \text{ cm}^3 \text{ sec}^{-1}$.

Laser action has recently been achieved on the $B\ ^2\Sigma^+ + X\ ^2\Sigma^+$ transition of HgX through dissociation of HgX_2 in an electrical discharge.^{1,2} Since Allison and Zare³ reported small cross sections for electron impact dissociation of the mercuric halides, the excitation mechanism for these laser systems using discharges in the HgX_2 molecule is not certain. On the other hand, a marked increase in laser efficiency and output power from the discharge pumped mercuric halide dissociation lasers has been obtained when nitrogen was added to the laser discharge.² Both electronically excited nitrogen and vibrationally excited nitrogen may be responsible for the improvement.

In the present work, we report the experimental results of dissociative excitation of $HgBr_2$ by metastable rare gas atoms (He, Ne, Ar, Kr and Xe) and N_2 ($A\ ^3\Sigma_u^+$) molecules. Rate constants of $HgBr^*$ formation from $HgBr_2$ reacting with Xe (3P_2) and N_2 ($A\ ^3\Sigma_u^+$) were measured.

Rare gas metastable atoms were generated by flowing purified rare gas through a hollow cathode discharge. The discharge source and the flow reactor used in this study were similar to designs used by Setser and his coworkers⁴ for observation of emission from reaction of the rare gas metastable atoms. A diagram of the flow reactor is shown in Fig. 1. Instead of flowing the parent rare gas through the discharge as in the case of He, Ne and Ar, Kr and Xe metastable atoms were produced by adding less than 1% of Kr or Xe to an argon flow before the discharge.⁵ Electronic energy transfer from argon metastable atoms to krypton and xenon thus provided the source of Kr and Xe metastables downstream. N_2 ($A\ ^3\Sigma_u^+$) molecules, mainly in $v = 0$ and $v = 1$, were produced by adding N_2 through the first reagent inlet to an argon flow.⁶ The $Ar\ (^3P_2) + N_2$ reaction produced $N_2\ (C\ ^3\Pi_u)$ and $N_2\ (B\ ^3\Pi_g)$ which radiatively cascade to the lowest metastable $N_2\ (A\ ^3\Sigma_u^+)$. Due to the

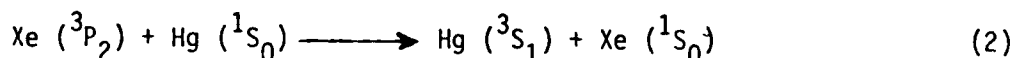
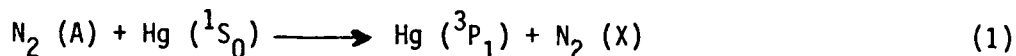
short radiative lifetime of the N_2 ($C^3\Pi_u$) and ($B^3\Pi_g$) states, 58 nsec⁶ and $\sim 1 \mu\text{sec}$ ⁴ respectively, only the long lived N_2 ($A^3\Sigma_u^+$) with measured radiative lifetime of 2 sec⁷ would survive several milliseconds in flow time downstream to the second reagent inlet.

Several milligrams of $HgBr_2$ were placed in a cell connected to the second reagent inlet. A carrier gas, argon, was used to transport the $HgBr_2$ vapor into the main stream. An oven with suprasil quartz windows to view the emissions from the two mixing zones was built to enclose the cell and the flow reactor. Temperatures at several locations inside the oven were monitored to ensure uniform heating. The reactor was pumped by a 500 l/min vacuum pump. The pressure at the second mixing zone was measured by a Wallace-Tiernan pressure gauge and was typically below 2 Torr. Emission from the reaction of $HgBr_2$ with rare gas metastables and N_2 (A) was monitored through the quartz tube which was joined to the pyrex section right before the second mixing zone. The detection system consisted of a 1/2 meter Jarrell-Ash monochromator fitted with an EMI 9635Q photomultiplier tube. The anode current was measured with a Keithley microammeter and the spectra were recorded on a strip chart recorder.

Table 1 summarizes the emission observed in the 250-600 nm wavelength region. In the reaction of lighter rare gas metastable atoms with $HgBr_2$, only mercury atomic lines were observed. However, $HgBr$ (B-X) emission intensity increased strongly with the lowering of the metastable energy in going from Ar and Kr to Xe and N_2 . A similar trend was found in the corresponding reaction of $HgCl_2$ with rare gas metastable atoms.⁸ The energy diagram for various $HgBr_2$, $Hg + 2Br$, $HgBr + Br$, N_2 and rare gas metastable states is shown in Fig. 2. It is apparent that the excitation energies of He^* , Ne^* and Ar^* are well above that of the $HgBr^* + Br$ product

channels, and hence other reaction pathways are more important. Also, the He, Ne and Ar metastable atoms have enough energy to Penning ionize the HgBr_2 molecule which has an ionization potential of 10.6 eV. The formation of HgBr^* in the reactions involving Kr^* , Xe^* and $\text{N}_2(\text{A})$ can be explained by energy transfer from the metastables to HgBr_2 followed by dissociation producing HgBr in the $\text{B } ^2\Sigma^+$ state and the $\text{C } ^2\Pi$ state, if energetically possible.

Figure 3 shows the emission spectra from $\text{N}_2(\text{A}) + \text{HgBr}_2$ and $\text{Xe } (^3\text{P}_2) + \text{HgBr}_2$ reactions at 1.7 Torr of mainly argon. The broad HgBr (B-X) emission peaked at 502 nm and extended well into the UV. The HgBr (B-X) emission spectrum from the reaction of $\text{Xe } (^3\text{P}_2)$ with HgBr_2 showed very little vibrational structure compared to that observed in the $\text{N}_2(\text{A}) + \text{HgBr}_2$ reaction. This is due to more vibrational levels of HgBr (B) state being formed in the case of excitation by Xe^* with emission to a large number of levels in the ground state of HgBr being overlapped. The Hg line emission at 2537 Å ($6 \text{ } ^3\text{P}_1 \rightarrow 6 \text{ } ^1\text{S}_0$) and 4358 Å ($7 \text{ } ^3\text{S}_1 \rightarrow 6 \text{ } ^3\text{P}_1$) in Fig. 3 were probably the results of energy transfer from $\text{N}_2(\text{A})$ and Xe^* to ground state Hg atoms.

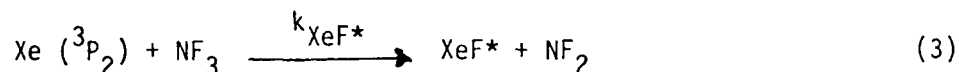


Ground state Hg atoms could be produced as a product of dissociation of HgBr_2 but more likely introduced as an impurity in the HgBr_2 powder.

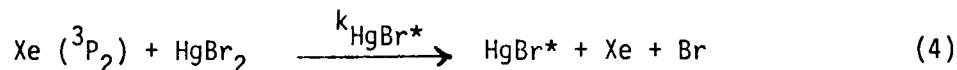
In the Xe and Kr metastable atom reaction with HgBr_2 , emission around 280 nm was observed (see Fig. 4) and identified as that of the HgBr (C-X) transition. The XeBr (B-X) emission which peaks at 2875 nm was not detected even though the $\text{XeBr}^* + \text{HgBr}$ product channel is exothermic by about 0.8 eV.

Reactive quenching of Xe* by HgBr₂ is apparently not competitive with energy transfer in this case.

The reaction of Xe (³P₂) with NF₃ was used as the reference reaction for assignment of rate constants to exit channels for quenching of Xe (³P₂) by HgBr₂ giving products which subsequently emit radiation. The rate constant for



has been measured⁹ to be $1.04 \times 10^{-10} \text{ cm}^3 \text{ sec}^{-1}$ at 300°K. The total emission intensity of the XeF (B-X) and (C-A) transitions was compared to the HgBr* emission



Assuming there is no quenching of the emitting states, the rate constant for HgBr* formation can be deduced from the following expression;

$$\frac{I_{\text{XeF}^*}}{I_{\text{HgBr}^*}} = \frac{k_{\text{XeF}^*} [\text{Xe } (^3\text{P}_2)] [\text{NF}_3]}{k_{\text{HgBr}^*} [\text{Xe } (^3\text{P}_2)] [\text{HgBr}_2]} \quad (5)$$

NF₃ was diluted in argon (typically < 10%) to 1 atm in a reservoir for use in the experiments. A second reservoir was filled with 1 atm of pure Ar. The flow from these two reservoirs was regulated by a single metering valve. The pure argon flow passed through the HgBr₂ cell while the Ar/NF₃ flow bypassed the cell. The main flow was not disturbed as reagent flow was switched from one reservoir to the other after emission spectra had been recorded. Thus, the concentration of Xe (³P₂) remained constant during the scans of both the reference and HgBr* spectra and was cancelled out in equation (5). The emission spectra were corrected for spectral response

of the detection system. Direct measurement of the HgBr_2 vapor pressure at the oven temperature (70-80°C) was not possible. Instead the vapor pressure data reported by Keller¹⁰ were used to determine the HgBr_2 concentration. The results are shown in Table 2. The HgBr^* formation rate constant for the $\text{N}_2(\text{A}) + \text{HgBr}_2$ reaction was determined by adding enough N_2 to convert all the $\text{Xe}(^3\text{P}_2)$ in the flow to $\text{N}_2(\text{A})$ through the reaction, $\text{Xe}(^2\text{P}_2) + \text{N}_2 \rightarrow \text{N}_2^*(\text{B,A}) + \text{Xe}$, and then comparing the XeF^* and HgBr^* emission intensities. Our value represents a lower limit to this rate constant since $[\text{Xe}(^3\text{P}_2)] \geq [\text{N}_2(\text{A})]$. Uncertainty in the HgBr_2 vapor pressure in the flow region represents the largest source of error in these measurements.

The rate constant derived above for dissociative excitation of HgBr_2 by $\text{N}_2(\text{A})$ yielding $\text{HgBr}(\text{B})$ may be compared to the total effective quenching rate of $\text{N}_2(\text{A})$ by HgBr_2 measured in a separate experiment.¹¹ The latter rate was found to be approximately $3.5 \times 10^{-10} \text{ cm}^3 \text{ sec}^{-1}$. Thus, it appears that $\text{HgBr}(\text{B})$ is produced with a branching ratio between 0.2 and 0.3 in reactions of $\text{N}_2(\text{A})$ with HgBr_2 . This low branching ratio is mainly responsible for the rather low (~ 1%) efficiency of the discharge-pumped mercury bromide dissociation laser. On the other hand, the large rate constant for excitation of $\text{HgBr}(\text{B})$ in collisions with $\text{Xe}(^3\text{P}_2)$ suggests that transfer from this excited state may provide a much more efficient pumping mechanism for the mercury bromide laser.

The authors wish to acknowledge useful discussions with Professor D. W. Setser (Kansas State University) and the technical assistance of D. M. Shores.

References

1. E. J. Schimitsche' and J. E. Celto, Opt. Lett. 2, 64 (1978).
2. R. Burnham, Appl. Phys. Lett. 33, 156 (1978).
3. J. Allison and R. N. Zare, Chem. Phys. 35, 263 (1978).
4. D. H. Stedman and D. W. Setser, Chem. Phys. Lett. 2, 542 (1968).
5. D. H. Stedman and D. W. Setser, Prog. React. Kinet. 6, 193 (1971).
6. J. E. Hesser, J. Chem. Phys. 48, 2518 (1968).
A. W. Johnson and R. G. Fowler, J. Chem. Phys. 53, 65 (1970).
W. R. Bennett, Jr. and J. Flint, Phys. Rev. A18, 2527 (1978).
7. D. E. Shemansky and N. P. Carleton, J. Chem. Phys. 51, 682 (1969).
8. a. J. H. Kolts and D. W. Setser (unpublished).
b. R. S. F. Chang and R. Burnham (unpublished).
9. J. E. Velazco, J. H. Kolts and D. W. Setser, J. Chem. Phys. 65, 3468 (1976).
10. L. L. Quille, ed., The Chemistry and Metallurgy of Miscellaneous Materials (McGraw-Hill, New York, 1950).
11. R. Burnham, Paper BB-7, Thirty Second Annual Gaseous Electronics Conference, Pittsburgh, PA (October 9, 1979).

Table 1. Emissions from $\text{HgBr}_2 + \text{M}^*$ reactions.

Reaction	$\text{Hg}^* 6p^3P_1$	$7s^3S_1$	$6d^3D$	HgBr(B-X)	HgBr(C-X)
$\text{HgBr}_2 + \text{He } (2^3S)$	S	S	S	N	N
Ne $(^3P_2)$	S	S	S	N	N
Ar $(^3P_2)$	S	S	N	N	N
Kr $(^3P_2)$	S	S	N	W	W
Xe $(^3P_2)$	W	W	N	S	W
$\text{N}_2 (A^3\Sigma_u^+)$	W	N	N	S	N

S = strong

W = weak

N = none

Table 2. HgBr* formation rate constants at 350⁰K

Reaction	Rate Constant (10 ⁻¹⁰ cm ³ sec ⁻¹)
Xe (³ P ₂) + HgBr ₂ —————→ HgBr* (B) + Xe + Br	5.3 ± 1.5
Xe (³ P ₂) + HgBr ₂ —————→ HgBr* (C) + Xe + Br	1.1 ± 0.3
N ₂ (A) + HgBr ₂ —————→ HgBr* (B) + N ₂ (X) + Br	≥ 1

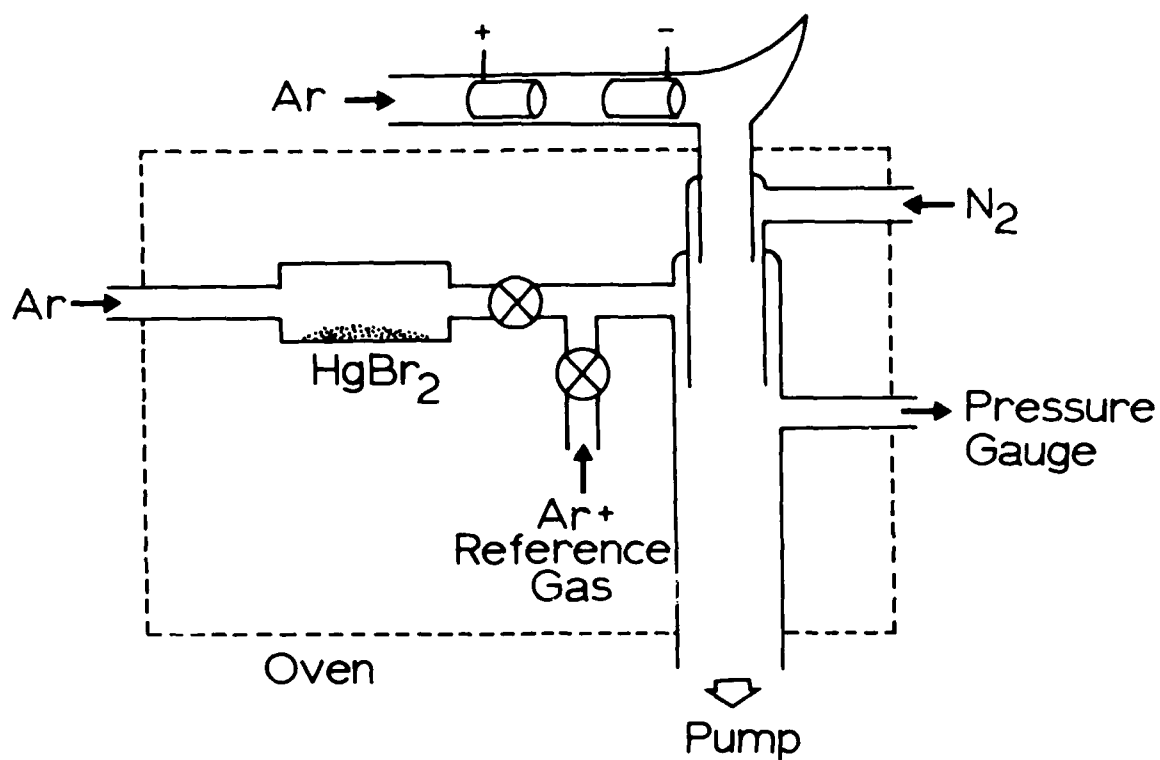


Figure 1. Diagram of the hollow cathode discharge flow apparatus.

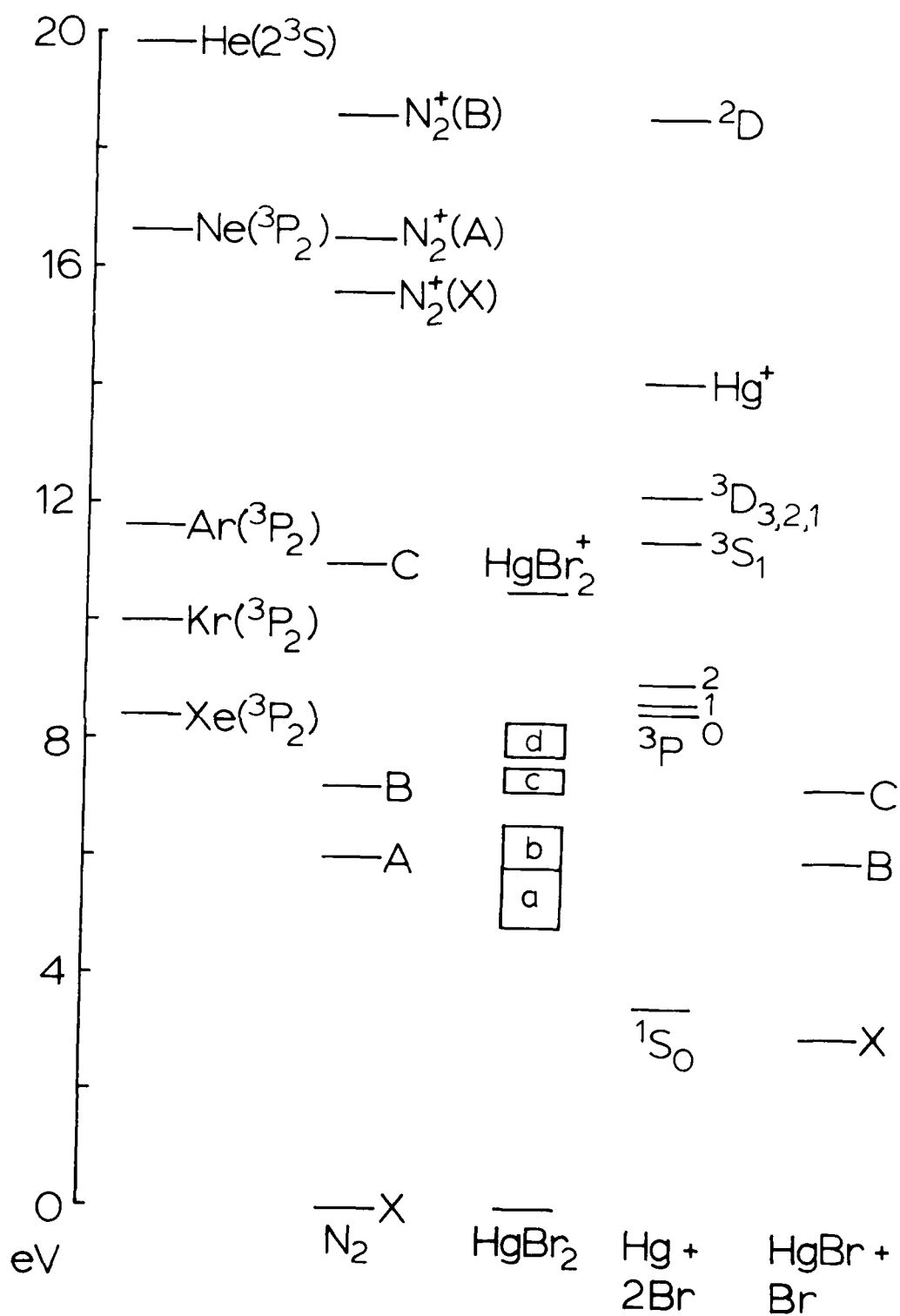


Figure 2. Energy diagram for N_2 , $HgBr_2$, $HgBr + Br$, $Hg + 2Br$ and rare gas metastable states.

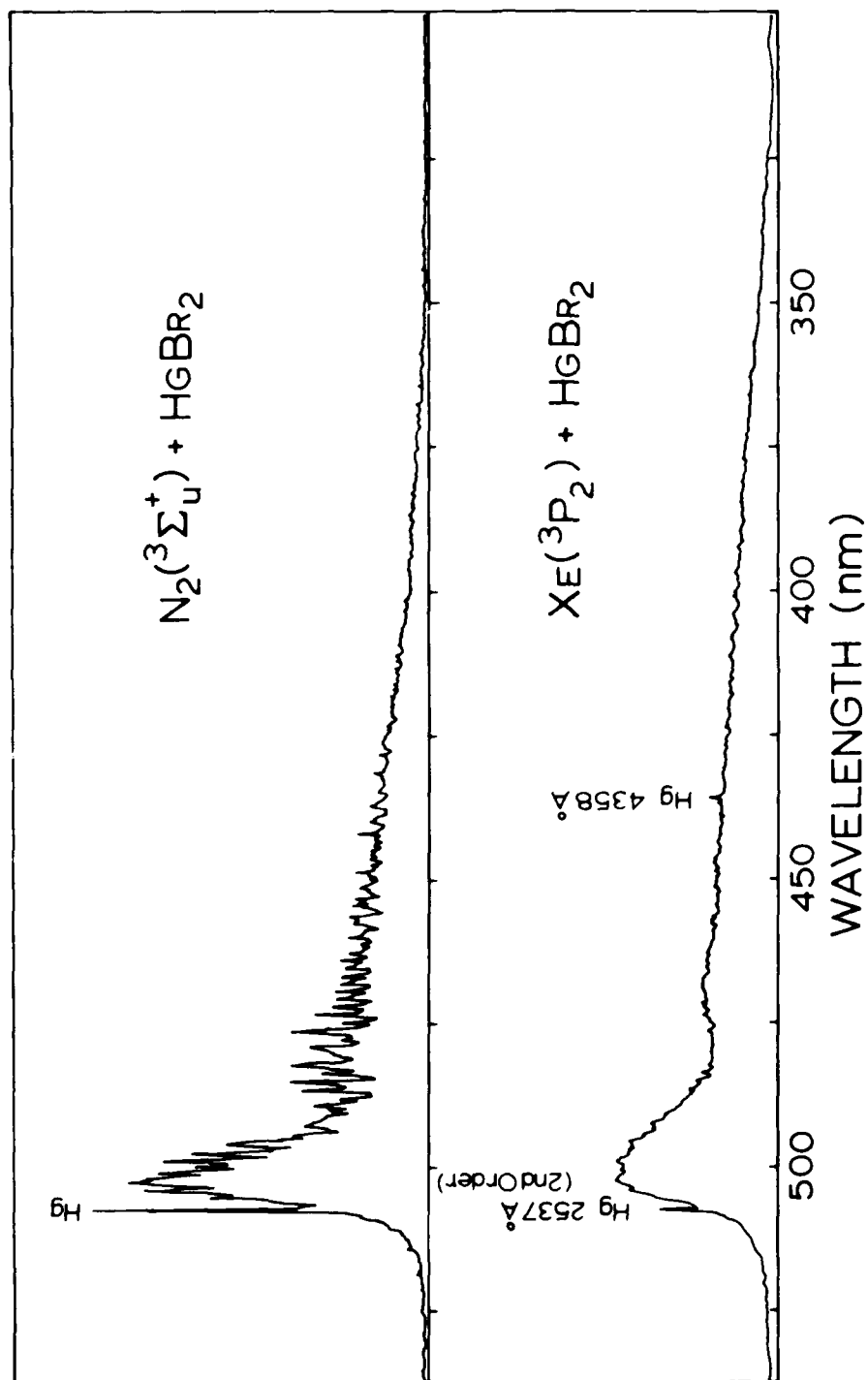


Figure 3. Emission spectra of HgBr (B-X) for N_2 (A) + HgBr₂ (Top) and Xe (³p₂) + HgBr₂ (Bottom); the pressure at the reaction zone was 1.7 torr.

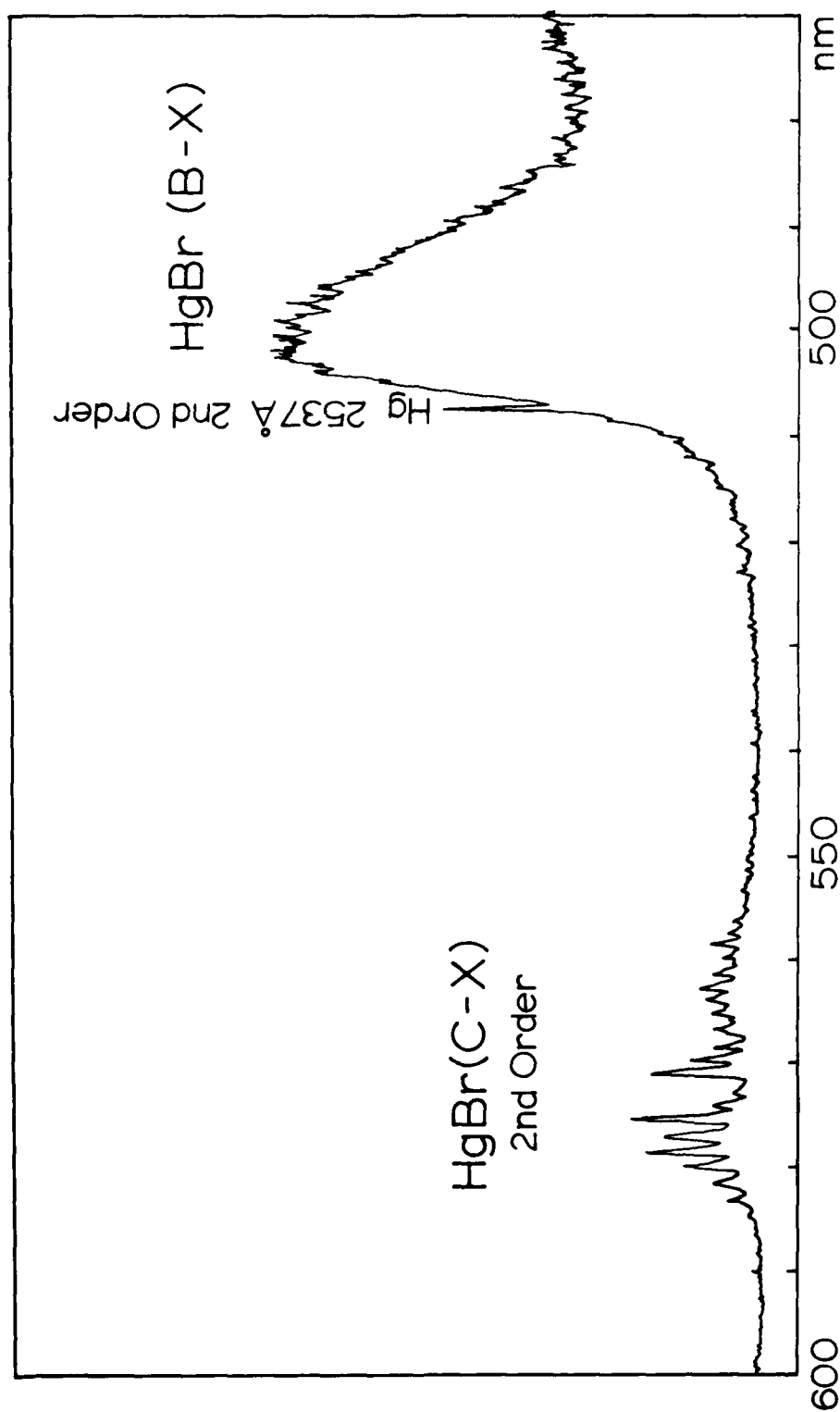


Figure 4. Second order emission spectra of HgBr (C-x) from the Xe (3P_2) + HgBr₂ reaction; the pressure at the reaction zone was 1.7 torr.

Absorption by Kr_2F^* at 358 nm

An extremely sensitive intracavity laser technique was used to probe for gain or absorption in the Kr_2F^* emission continuum. Experiments were conducted at 196⁰K and at room temperature. A detailed time-dependent computer model for e-beam pumped Ne/Kr/ F_2 gas mixtures was developed to analyze the absorption measurements. Analysis of the data with this model has identified that the primary absorbers at 358 nm are Ne_2^+ , Kr_2^+ and Kr_2F^* . The analysis also provides estimates of the Ne_2^+ and Kr_2F^* photoabsorption cross sections ($8.1 \times 10^{-19} \text{ cm}^2$ and $5.4 \times 10^{-18} \text{ cm}^2$, respectively). Also, the quenching rate of Kr_2F^* by F_2 was measured as a function of temperature.

Absorption in the Near-Ultraviolet Wing of the Kr_2F^* (410 nm) Band

J. G. EDEN, MEMBER, IEEE, R. S. F. CHANG, AND L. J. PALUMBO

Abstract—An intracavity laser technique has been used to study the absorption of electron-beam pumped Ne/Kr/F₂ gas mixtures (196 and 300 K) in the “blue wing” of the Kr_2F^* emission continuum. The experiments were conducted at 358 nm using the $v' = 0 \rightarrow v'' = 1$ transition of the N_2 ($C \rightarrow B$) laser. Comparing the results with the predictions of a computer model, the species primarily responsible for absorption have been identified as Ne_2^+ , Kr_2^+ , and Kr_2F^* . The photoabsorption cross sections for Ne_2^+ and Kr_2F^* (Kr_2F^+) at 358 nm have been estimated to be $8.1 \cdot 10^{-19}$ and $5.4 \cdot 10^{-18} \text{ cm}^2$, respectively. The Kr_2F^* absorption cross section is roughly 20 percent of that reported for Kr_2^+ at the same wavelength. The fluorescence efficiency of Kr_2F^* in e -beam excited 94.93 percent Ne/5 percent Kr/0.07 percent F₂ ($p_{\text{total}} = 4000$ torr) gas mixtures has been found to be a factor of 2.8 higher than that of the N_2 ($C \rightarrow B$) band in Ar/5 percent N_2 mixtures. Also, the rate constant for quenching of Kr_2F^* by F₂ was measured to be $(4.1 \pm 0.5) \cdot 10^{-10} \text{ cm}^3 \cdot \text{s}^{-1}$ at 300 K and $(3.0 \pm 0.5) \cdot 10^{-10} \text{ cm}^3 \cdot \text{s}^{-1}$ at 196 K.

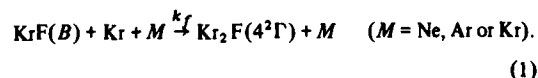
1. INTRODUCTION

IN THE course of investigating the properties of diatomic rare gas-halide laser media pumped by electron beams, several laboratories recently observed [1]–[4] broad, structureless continua lying to the red of the familiar $B \rightarrow X$ and $C \rightarrow A$ bands. Subsequently, these continua were assigned [1], [5] to bound-to-free transitions of Rg_2X^* (Rg = rare gas, X = halogen atom) molecules which calculations [6]–[10] have

verified are strongly ionic in nature ($\text{Rg}_2^+X^-$). To date, fluorescence from the $4^2\Gamma \rightarrow 1^2\Gamma$, $2^2\Gamma$ [6], [7] bands of Ar_2F [1]–[4], Kr_2F [1]–[4], Ar_2Cl [2], Kr_2Cl [2], and Xe_2Cl [2] have been identified.

The study of these excited triatomic species has led to several interesting and significant conclusions. The first is that theoretical considerations [6], [7] suggest that the weak perturbation of Rg_2^+ by X^- causes Rg_2X^* to absorb UV radiation in much the same way as does Rg_2^+ . For example, Wadt and Hay [6] have calculated the peak absorption wavelengths and oscillator strengths for the $4^2\Gamma \rightarrow 9^2\Gamma$ transition of Ar_2F^* and Kr_2F^* to be virtually identical to those of the corresponding rare-gas dimer ions Ar_2^+ and Kr_2^+ . This absorption clearly may have a significant impact on the extraction efficiency of diatomic rare gas-halide lasers.

Secondly, Rokni and co-workers [11] have shown that, as predicted by potential calculations [6], formation of Rg_2X^* (specifically, Kr_2F^*) occurs primarily through the three-body collision



Reaction (1) represents a significant loss channel for $\text{KrF}(B)$ molecules in rare gas/F₂ mixtures above ~ 1 atm.

Finally, the strong emission available from the triatomic rare gas-halide molecules suggests that the Rg_2X^* molecules are attractive laser candidates in their own right. In particular, the intense fluorescence observed from the Kr_2F^* molecule in excited, high pressure (>1 atm) Ar/Kr/F₂ gas mixtures prompted Hunter and co-workers (HOHM) [12] to attempt to

Manuscript received April 6, 1979; revised May 7, 1979. This work was supported in part by the Defense Advanced Research Projects Agency (DARPA).

J. G. Eden is with the Department of Electrical Engineering, University of Illinois at Urbana-Champaign, Urbana, IL 61801.

R. S. F. Chang and L. J. Palumbo are with the Naval Research Laboratory, Washington, DC 20375.

obtain laser oscillation from the molecule at $\lambda \sim 400$ nm in the violet. Due to the long spontaneous radiative lifetime of Kr₂F* (133–181 ns) [6], [13] and the broad bandwidth of the $4^2\Gamma \rightarrow 1^2\Gamma$ continuum ($\Delta\lambda \sim 43$ nm), a Kr₂F laser would potentially have low gain ($\sigma_{\text{sp}} \sim 5 \cdot 10^{-18}$ cm²) suitable for amplifier applications, and be tunable and efficient. Unfortunately, peak absorptions as high as 0.15 percent \cdot cm⁻¹ at 441.6 nm were measured by HOHM [12] in electron-beam pumped Ar, Kr, and F₂ gas mixtures at room temperature.

Several investigators [3], [14] have reported a strong increase in Kr₂F* emission intensity at lower temperatures (<200 K). This low temperature fluorescence enhancement is consistent with the negative temperature dependence of k_f in (1) calculated by Shui [15]. Also, HOHM's studies involved the use of argon as a diluent and so a large fraction of the absorption observed could have been due to the argon dimer ion, Ar₂⁺ (see [16]). Cooling of the laser gas also serves to sharpen the Ar₂⁺ or Kr₂⁺ absorption spectral profiles [16], thus minimizing the rare-gas molecular ion absorption in the Kr₂F* emission band. Therefore, taking into account the enhanced formation rate of Kr₂F* at low temperatures and the possible overlap of the Ar₂⁺ and Kr₂⁺ absorption profiles with the probe wavelength, the negative results of HOHM "... are inconclusive with respect to the possibility of obtaining efficient [laser] output in the visible" from Kr₂F* [12].

For these reasons, a study of the collisional and optical properties of Kr₂F* molecules produced in *e*-beam pumped Ne, Kr, and F₂ mixtures at dry ice and room temperature was undertaken. The results of these experiments, which will be reported here, include:

- 1) the measurement of the fluorescence efficiency of Kr₂F* relative to the N₂(C \rightarrow B) band,
- 2) determination of the rate constants for quenching of Kr₂F* ($4^2\Gamma$) by F₂ at 196 and 300 K,
- 3) observation of strong absorption in the near-UV wing of the Kr₂F* emission band at 358 nm, and
- 4) the identification of Kr₂F* itself, Ne₂⁺ and Kr₂⁺ as the dominant absorbing species. By comparing the experimentally determined gas pressure variation of this absorption with the predictions of a comprehensive computer kinetics model, the absorption cross sections for Kr₂F* and Ne₂⁺ at $\lambda = 358$ nm have been estimated to be $5.4 \cdot 10^{-18}$ cm² and $8.1 \cdot 10^{-19}$ cm², respectively.

The intracavity laser technique, which was used to measure the gas medium absorption, and the fluorescence experimental apparatus will be described in Section II. Section III discusses in detail the computer kinetics model used in this study. Finally, Section IV presents the data and discusses the implications for a prospective Kr₂F* laser and Section V summarizes the conclusions of the paper.

II. EXPERIMENTAL

The experiments reported here consisted of two parts. First, the Kr₂F* fluorescence of room temperature and cooled (dry ice, 196 K) Ne/Kr/F₂ gas mixtures excited by an intense electron beam was examined. The second segment of the study involved measurement of the absorption of these same gas mixtures at 358 nm using an intracavity laser absorption technique.

A. Spontaneous Emission Experimental Apparatus

The experimental apparatus used for the spontaneous emission experiments was composed of 1) an electron-beam generator, 2) a high-pressure fluorescence cell and associated vacuum and gas handling equipment, and 3) a spontaneous emission detection system. The electron-beam generator, which has been described in detail previously [17], produced a 50 ns FWHM pulse of 450 keV electrons. A diverter switch installed in the last section of the 8 Ω pulse forming water line enabled the electron pulsewidth to be shortened to ~ 10 –15 ns FWHM. The *e*-beam diode was maintained at a vacuum of better than 10^{-4} torr and the electrons exited the diode through a 25 μ m thick titanium foil. For the anode-cathode gap of 1.6 cm used in these experiments, the current density at the Ti foil was ~ 1 kA \cdot cm⁻².

A second metal foil, 37.5 μ m thick Inconel 718, was welded to the stainless-steel fluorescence cell. Inconel was used in this case since titanium is strongly attacked by the halogens. The cell itself was simply a ~ 30 cm long section of 3.8 cm OD stainless-steel tubing heliarc-welded to a ~ 1 cm thick stainless-steel plate. A $\sim 16 \times 2.9$ cm slot was machined in the plate to define the *e*-beam excitation area and 7 cm ($2\frac{3}{4}$ in) diameter "knife-edge" vacuum fittings were welded on each end of the cell to provide mountings for 2.5 cm diameter Suprasil quartz windows. The cell aperture was circular (1.3 cm diameter) and the windows were sealed to the cell using silicone rubber O-rings. The axis of the fluorescence cell was oriented perpendicular to the electron beam and was situated ~ 1.5 cm from the Inconel foil.

The rare gases used in these studies were of research grade and the stated purity of the F₂ was 98 percent. All gases were used without further purification but a fresh gas mixture was prepared for each *e*-beam shot. As is true for any experiments involving the halogens (and F₂ in particular), passivation of the cell was found to be essential for obtaining repeatable results. This was accomplished by allowing ~ 100 torr of F₂ to stand in the cell for ~ 1 h. To cool the gas mixtures, a stainless-steel enclosure that could hold dry ice was built for the cell.

The axial spontaneous emission from the excited Ne/Kr/F₂ gas mixtures was recorded either on photographic film or by a photodiode. The photodiode (Hamamatsu S-20) was located ~ 0.5 m from the cell and the spectral regions of interest were isolated using dielectric bandpass or colored glass filters. Also, neutral density filters were sometimes inserted in the optical path to prevent saturation of the photodiode. Axial emission spectra were recorded on Polaroid Type 55 or 57 film using a 1 m Jarrell-Ash spectrograph and a UV quality quartz lens of ~ 30 cm focal length.

B. Intracavity Absorption Technique

Fig. 1 shows a simplified diagram of the technique used to measure absorption at 358 nm. Since low net gain or absorption (< 1 percent \cdot cm⁻¹) was expected for the Kr₂F* band, a technique similar to that described by Marowsky and co-workers [18] was adopted. A major difference between the two approaches is, as shown in Fig. 1, that for the experimental setup described here, two cells are placed inside an optical cavity. The right cell holds an Ar/5 percent N₂ mixture which,

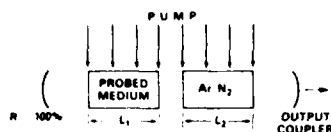


Fig. 1. Simplified schematic diagram of the laser intracavity technique used to measure absorption in electron-beam pumped Ne, Kr, and F_2 gas mixtures. The existence or absence of gain in the "probed medium" was deduced by observing the Ar-N₂ laser output at 357.7 nm with and without the desired gas mixture in the "probed" (auxiliary) cell. The response of the system to absorption in the probed gases was calibrated by first blocking the access of the e-beam to the auxiliary cell and then recording the Ar-N₂ laser output for various pressures of F_2 or Cl_2 in the cell (see text).

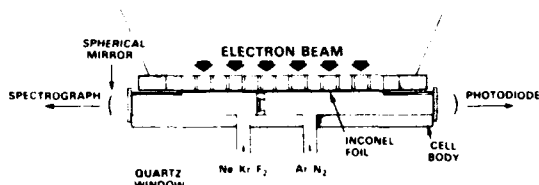


Fig. 2. Layout of the intracavity absorption (or gain) measurement apparatus. The cell body (shaded) was machined from stainless steel. A 10 mm dia. quartz window separated the Ar-N₂ laser compartment from another section containing the Ne, Kr, and F_2 gas mixture. A titanium foil (not shown) was welded to the slotted foil support plate to maintain the vacuum integrity of the e-beam diode.

when excited by an intense e-beam, produces oscillation on the 357.7 nm line of the N_2 ($C \rightarrow B$) band. The other cell contains the medium to be probed for gain (or loss). With a vacuum in the "probed" cell, then the Ar-N₂ laser is operated at, or just above, threshold. At this point, the laser is very sensitive to small changes in the gain of the system. After filling the second cell with the desired gas mixture, a resulting enhancement or decline in the Ar-N₂ laser output power, due to the gain or loss of the excited gas in the "probed" cell, will be observed. Two cells were found to be necessary because, in general, the collisional kinetics of the probed medium will interfere with the operation of the Ar-N₂ laser if both gas mixtures are included in the same cell.

A cross-sectional view of the e-beam cell used in these experiments is shown in Fig. 2. A Suprasil quartz window of ~ 1 cm diameter divided the cell into two vacuum tight sections of 9.5 and 13 cm in length and 1.5 cm diameter. (The lengths of each section that were excited by the e-beam were 5.8 and 9.2 cm, respectively.) The two exterior quartz windows were 2.5 cm in diameter and were sealed to the cell body using rubber gaskets. All tubing connecting the cell with the gas handling system was made of either stainless steel or Teflon. The purity of the gases used and the cell passivation technique were the same as described above for the fluorescence experiments.

As before, the 450 keV electron beam entered the two cells by passing through a foil support plate, a 25 μ m thick Ti foil (not shown in Fig. 2) and a 37.5 μ m thick Inconel 718 foil. The laser cavity was formed by two dielectric-coated mirrors of 5 m radius of curvature that were separated by ~ 30 cm. Both mirrors were highly reflecting ($R > 99$ percent) over the wavelength range 350–410 nm and transmitted ~ 0.5 percent at 358 nm.

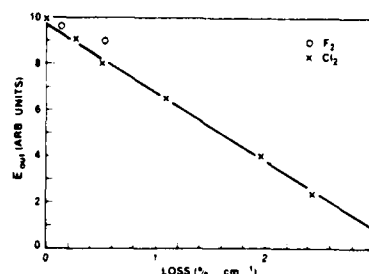


Fig. 3. Absorption calibration of the laser intracavity experiment using the known absorption of F_2 and Cl_2 in the near UV. The Ar-N₂ laser output energy was measured for $P_{F_2} < 100$ torr and $1.1 < P_{Cl_2} < 12$ torr.

The output of the Ar-N₂ laser probe at 357.7 nm was monitored either by a 1 m spectrograph (in first order) and Polaroid Type 57 film or by a photodiode and bandpass and/or neutral density filters. Emission spectra were obtained by scanning the photographic negatives with a Joyce-Loebl microdensitometer.

C. Absorption Calibration Using F_2 and Cl_2

In order to obtain quantitative absorption/gain data, it was necessary to accurately calibrate the system of Fig. 2. This was accomplished in the following way. Into the longer e-beam cell was admitted a 3000 torr Ar, 150 torr N_2 gas mixture while the shorter compartment was kept at vacuum. Firing the electron gun produced lasing on the (0, 1) transition of the N_2 ($C \rightarrow B$) band at 357.7 nm. A known pressure of F_2 or Cl_2 was then admitted to the short cell and a brass plate of 0.83 mm thickness was taped over the e-beam aperture of this cell to prevent excitation of the F_2 or Cl_2 . The e-beam was again fired (a fresh Ar-N₂ fill was used for each shot) and the observed decrease in the Ar-N₂ laser energy output was recorded. Since the absorption cross sections for both F_2 [19] and Cl_2 [20] in the near UV are well known, the dependence of the relative Ar-N₂ 358 nm laser output energy on the amount of loss in the second cell could then be determined. The result of this calibration procedure is shown in Fig. 3 where the Ar-N₂ laser energy is given in arbitrary units. The solid line in the figure represents the linear least squares fit of the Cl_2 data. It was difficult to extend the F_2 data beyond ~ 0.5 percent \cdot cm⁻¹ due to the large fluorine pressures required [19] and, for this reason, most of the data shown is due to Cl_2 . The solid line of Fig. 3 can be represented by the relationship: percent loss = $-0.34 (E_{out} - 9.75)$. This equation was used to determine the magnitude of the absorption of e-beam pumped Ne, Kr, and F_2 gas mixtures and the results will be presented in Section IV.

III. COMPUTER MODEL OF ELECTRON-BEAM EXCITED Ne/Kr/ F_2 GAS MIXTURES

A. Computational Technique

A comprehensive computer model has been developed to predict the transient densities of various species in an e-beam excited mixture of Ne, Xe, and F_2 . This model employs calculational methods described in previous models of e-beam pumped and e-beam sustained KrF, XeF, and XeCl rare gas-

halide lasers [21]–[23]. A Runge-Kutta-Treanor algorithm [24] integrates the spatially homogeneous, time-dependent rate equations which describe the temporal behavior of the species of interest. The required rate equations are generated internally by the computer code from a symbolically specified chemical reaction list. This method reduces coding errors and allows easy modification of rate constants and processes. The present model keeps track of the effect of 58 reactions on the time evolution of the population of 26 species from *e*-beam ionization and excitation of the rare gases to Kr₂F* formation, quenching, and radiation. A variety of diagnostics are printed out as a function of time to provide insight into important processes and energy flow.

B. Relevant Processes and Rate Constants

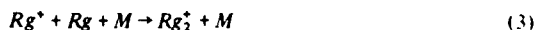
Since extensive kinetics investigations and computer modeling have been carried out in support of the development of *e*-beam pumped and *e*-beam sustained KrF lasers (using Ar diluent) and XeF lasers (primarily using Ne diluent), many of the rate constants for important processes involving transient species in *e*-beam excited Ne/Kr/F₂ mixtures are already known. Thus, few assumptions were required in order to model the formation and decay of Kr₂F* in Ne diluent at room temperature. Therefore, most of the rate constants to be presented below were measured at room temperature (≈ 300 K) although a few reactions have also been studied at reduced temperatures. In order to predict the transient densities of various excited species in cooled (200 K) Ne, Kr, and F₂ gas mixtures, rate constants that have been measured or calculated for 200 K have been incorporated into the model. Otherwise, the room temperature rate constants were used.

1) *Electron-Beam Excitation and Ionization*: The intense, 450 keV electron-beam pump is treated by the model simply as a source term for the production of ions, electrons, and metastables from ground state Ne and Kr rare-gas atoms. The ion production rate, $R_{i,Rg}$, is given by

$$R_{i,Rg} = F_e \cdot N_{Rg} \cdot S_{Rg} \cdot M_{Rg} \cdot W_{Rg}^{-1} \quad (2)$$

where F_e is the incident electron flux, N_{Rg} is the ground state density of the rare gas, S_{Rg} is the stopping power of the rare gas for high energy electrons (typical units: eV · cm² · gm⁻¹), M_{Rg} is the mass of the rare-gas atom, and W_{Rg} is the deposited electron energy required to produce an ion-electron pair. The W values used in this model are 36.4 eV for Ne and 24.05 eV for Kr. In the present model, the stopping powers tabulated by Berger and Seltzer [25], multiplied by a factor of 2.5 to account for electron scattering, were used. This factor was determined by comparing ion production rates obtained from a detailed electron transport computer code [26], [27] with rates derived using the values given by Berger and Seltzer. The metastable production rate was estimated to be 0.29 times the ion production rate for both Ne and Kr. From (2), it is clear that the ion and metastable formation rates for a given rare gas are proportional to its partial pressure in the gas mixture. Direct electronic excitation of F₂ by the *e*-beam and the ionization and excitation of Kr by low energy (less than the Ne metastable energy) secondary electrons have been neglected.

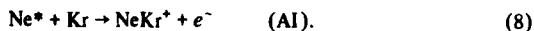
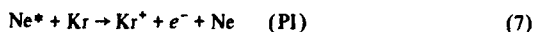
2) *Homonuclear Rare-Gas Reactions*: The energy channeled into rare-gas ions and metastables cascades down a complex chain to eventually produce Kr₂F*. For each rare gas *Rg*, the initial steps in this cascade process can be represented by



where *Rg* represents either Ne or Kr, and *M* represents any third body. In the high-pressure mixtures studied here, reaction (3) proceeds rapidly. The rate constants for this process were taken to be 4.6×10^{-32} cm⁶ · s⁻¹ [28] and 6.1×10^{-32} cm⁶ · s⁻¹ [29] for *Rg* = Ne and *Rg* = Kr, respectively. The rate constants are assumed to be the same regardless of the third body *M*. This same assumption is made for all the other three-body reactions discussed here. Polyatomic ion complexes such as Ne₃⁺, Ne₄⁺, Kr₃⁺, etc., while possibly abundant at the high pressure considered here, are ignored in the model which is equivalent to assuming that these complex ions contribute to the KrF* and Kr₂F* formation chains in the same way that their respective dimer ions do.

The dissociative recombination rate coefficients used for reaction (4) were $3.5 \cdot 10^{-8}$ cm³ · s⁻¹ for Ne₂⁺ [30] and $2.2 \cdot 10^{-7}$ cm³ · s⁻¹ for Kr₂⁺ [31], assuming an electron temperature of 1 eV. The rare-gas excimer formation rates [reaction (5)] were recently measured to be much slower for formation of Ne₂^{*} (4.1×10^{-34} cm⁶ · s⁻¹, [32]) than for Kr₂^{*} (5.4×10^{-32} cm⁶ · s⁻¹ [33]). Although the spontaneous radiative lifetime of Kr₂^{*} [see reaction (6)] has been measured to be 280 ns [13], the lifetime for Ne₂^{*} is unknown and was taken to be 100 ns. However, in the mixtures of interest to the present work, very little Ne₂^{*} is formed because Ne* is rapidly intercepted by Penning and associative ionization reactions with Kr. Thus, the predictions of the model depend weakly on the assumed Ne₂^{*} radiative rate.

3) *Mixed Rare-Gas Reactions*: Two important processes in the formation chain of the rare gas-halides in neon diluent are Penning ionization and associative ionization:



The room temperature rate constants used for these reactions were those reported by Neynaber and Magnuson [34]: 5×10^{-10} cm³ · s⁻¹ for the Penning process (7) and 2.5×10^{-10} cm³ · s⁻¹ for reaction (8). The sum of the two rate constants agrees with the total quenching rate constant of Ne* by Kr published by Brom *et al.* [35].

The complex ion NeKr⁺ subsequently undergoes charge exchange with Kr or dissociative recombination with electrons as follows:



TABLE I
F* AND F₂* QUENCHING RATE CONSTANTS [32]

Reaction	Rate constant ^(a)	Notes
1. F* + Ne → F + Ne	$< 5.0 \times 10^{-15}$	(b)
2. F* + F ₂ → F ₂ * + F	5.1×10^{-10}	(c)
3. F* + 2Ne → F + 2Ne or NeF* + Ne	$< 1.0 \times 10^{-35}$	(b), (d)
4. F ₂ * + Ne → 2F + Ne	$< 1.0 \times 10^{-13}$	(b)
5. F ₂ * + F ₂ → 2F + F ₂	3.5×10^{-10}	(c)
6. F ₂ * + 2Ne → 2F + 2Ne	$< 1.0 \times 10^{-33}$	(b)
7. F ₂ * → 2F + hν (158 nm)	$\tau = 41$ ns	

(a) Units: cm³ sec⁻¹ for two-body reactions, cm⁶ sec⁻¹ for three-body reactions

(b) One half the upper limit is used as the rate constant for computational purposes

(c) The products (not specified in reference [32]) are chosen here somewhat arbitrarily. This assumption is inconsequential to the predicted formation of KrF* and Kr₂F*, since it represents interception regardless of the branching ratio chosen.

(d) The branching ratio for production of NeF* is arbitrarily assumed to be 50%.

Cross sections for reactions (9) and (10) have been measured [36] at 330 K. Rate constants calculated from these published cross sections are 1.3×10^{-9} cm³ · s⁻¹ and 4.6×10^{-11} cm³ · s⁻¹ for reactions (9) and (10), respectively. The rate constant for reaction (11) was estimated to be of the same order of magnitude as that for the analogous reaction (4). A value of 1.7×10^{-7} cm³ · s⁻¹ was used in the present model.

4) *Fluorine Atoms and Molecules*: Again assuming the electron temperature to be ~1 eV, then the dissociative attachment reaction



proceeds with a rate constant of $5 \cdot 10^{-9}$ cm³ · s⁻¹ [37]. This rate constant varies slowly over the electron temperature range 0.1–1 eV.

Electronically excited fluorine atoms (F*) and molecules (F₂*) are formed in *e*-beam excited, neon diluted gas mixtures by the chain



Quenching rates for F* and F₂* have been recently measured by Huestis and co-workers [32]. Their results, along with some minor assumptions invoked to apply these rates to the present model, are listed in Table I.

For the intense pump used in these experiments, it appears that at low F₂ partial pressures, a fraction of the initial F₂ is depleted and a large concentration of F atoms is present in the gas mixture both during the *e*-beam pump pulse and the "after-glow." (The recombination of F atoms to F₂ molecules is assumed to be negligible on a 100 ns time scale.) Thus, it is important to consider quenching reactions involving F atoms. Since very little experimental quenching data on atomic fluorine exist, it has been assumed that rate constants for reactions involving F are the same as those for the analogous reactions involving F₂. For example, the collisional process



is assumed to proceed with a rate constant of 3.5×10^{-10} cm³ · s⁻¹, the same as that for reaction 5 in Table I.

The energy of the lowest lying electronic excited state of atomic fluorine is insufficient to Penning ionize Kr. Thus, the interaction of F* with Kr may be expected to produce a high lying excited state of Kr which will rapidly cascade down to one of the Kr metastable levels, designated here as Kr*. The process



was assumed to occur with a rate constant of $1 \cdot 10^{-12}$ cm³ · s⁻¹ in analogy with other quenching reactions of atomic metastables by ground state rare-gas atoms (see, for example, [38a]). The predictions of the model are weakly dependent on the rate constant for reaction (14) although this is the only process in the model that links energy flow from the NeF* and F* channel with the formation of KrF* and Kr₂F*.

5) *NeF* Formation and Predissociation*: The rate constant for quenching of Ne* by F₂ has been measured to be 5.3×10^{-10} cm³ · s⁻¹ by Huestis *et al.* [32]. In this model the branching ratio for the formation of NeF* is assumed to be unity. That is,



By analogy, it is also assumed that



proceeds with the same rate constant. Effective two-body rate constants of 3×10^{-6} cm³ · s⁻¹ [39] and 3.3×10^{-6} cm³ · s⁻¹ [40], respectively, have been computed for the reactions

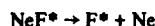


and



for a background pressure of 5 amagats Ne. These rate constants vary slowly with Ne pressure and are similar to those for krypton diluent and so, for simplicity, the above rate constants were used for reactions (17) and (18) for all the gas mixtures modeled.

Predissociation into F* is assumed to dominate the collisional loss processes for NeF* and thus the mechanism



(assuming a predissociation lifetime of 0.5 ns [41]) is the only NeF* loss process considered by the model.

6) *KrF* and Kr₂F* Formation, Quenching, and Radiation*: The krypton fluoride exciplex and its formation and quenching rates, in particular, have been the subject of numerous investigations in the development of the KrF laser [4], [11], [15], [42]–[44]. The processes considered and rate constants used in the present model are summarized in Table II. The rate constant for process (13) is one of the few for which its temperature dependence has been calculated [15]. So, in modeling Ne/Kr/F₂ gas mixtures at low temperature, Shui's results were extrapolated to 200 K.

TABLE II
FORMATION AND QUENCHING OF KrF*

Reactants	Products	Rate constant ^(a)	Reference	Notes
1 Kr* + F ₂ → KrF* + F		7.2 × 10 ⁻¹⁰	38b	
2 Kr ₂ * + F ₂ → KrF* + Kr + F		2.1 × 10 ⁻¹⁰	13	(b)
3 Kr ₂ * + F → KrF* + Kr		2.1 × 10 ⁻¹⁰	Analogy with 2	(c)
4 Kr* + F* → KrF*		3.0 × 10 ⁻⁶	42	(d)
5 Kr ₂ * + F* → KrF* + Kr		2.8 × 10 ⁻⁶	42	(d)
6 NeKr* + F* → KrF* + Ne		3.0 × 10 ⁻⁶	Analogy	(d,e)
7 KrF* + Ne → Products		1.6 × 10 ⁻¹²	43	(f)
8 KrF* + Kr → Products		8.6 × 10 ⁻¹²	44	(f)
9 KrF* + F ₂ → Products		4.8 × 10 ⁻¹⁰	44	(f)
10 KrF* + F → Products		4.8 × 10 ⁻¹⁰	Analogy with 9	(c,f)
11 KrF* + 2Ne → Products		1.0 × 10 ⁻³²	43	(f,g)
12 KrF* + Kr + F + hν (249 nm)		τ = 6.8 ns	44	
13 KrF* + 2Kr → Kr ₂ F* + Kr		9.7 × 10 ⁻³¹	44	(h)
14 KrF* + Kr + Ne → Kr ₂ F* + Ne		9.7 × 10 ⁻³¹	Analogy w/ 13	(h,i)

(a) Units: cm³ sec⁻¹ for two-body reactions; cm⁶ sec⁻¹ for three-body reactions

(b) Unit branching into KrF* is most likely (see reference 6).

(c) F atoms are assumed here to quench the excited species at the same rate as does F₂.

(d) These are effective two-body rate constants for a Ne diluent background density of 5 atm. They vary slowly with Ne and Kr density and so were assumed to be constant for all the gas mixtures modeled.

(e) The rate constant for reaction 6 is estimated by analogy from reactions 4 and 5.

(f) For the purposes of the present model, "Products" are assumed to be ground state atoms.

(g) One-half the upper limit is used as the rate constant for computational purposes.

(h) Reference 6 predicted and reference 11 showed experimentally that this three-body quenching of KrF* will likely form Kr₂F*.

(i) The three-body rate constant is assumed to be the same regardless of the identity of the third body.

The two-body quenching rate constants and radiative lifetime recently measured for Kr₂F* by Quigley and Hughes [13] are used in the model. The rate constants are $<2 \times 10^{-14} \text{ cm}^3 \cdot \text{s}^{-1}$ for Kr and $4.3 \times 10^{-10} \text{ cm}^3 \cdot \text{s}^{-1}$ for F₂ and the Kr₂F* lifetime is 181 ns. This experimental lifetime is in reasonable agreement with the theoretical value of 133 ns determined by Wadt and Hay [6]. If Ne is assumed to quench Kr₂F* (in two-body collisions) as fast as Kr, then even at high Ne pressures (e.g., 4000 torr), rare-gas deactivation of Kr₂F* contributes negligibly to the total quenching. Once again, it is assumed that the quenching rate constant of Kr₂F* by F atoms is the same as that for F₂ molecules. Formation of Kr₂F* is presumed to occur primarily through three-body destruction of KrF* (reactions 13 and 14 in Table II).

In order for the model to reproduce the experimentally observed dependence of the peak Kr₂F* fluorescence intensity on the partial pressure of Kr ($p_{\text{Kr}} = 0\text{--}1500 \text{ torr}$; see Fig. 4) it was necessary to postulate a three-body quenching process for Kr₂F*. The best agreement between the computer predictions

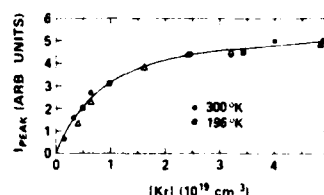


Fig. 4. Variation of the peak intensity of the Kr₂F* 410 nm band with Kr density at room and dry ice temperature. The open triangles (Δ) represent the predictions of the computer model described in Section III, assuming $T = 300 \text{ K}$. Although not shown, the time-integrated Kr₂F* fluorescence was found to exhibit the same dependence on [Kr].

and the experimental results was obtained when the rate constant for the collisional reaction



where M is either Ne or Kr, was taken to be $2.5 \times 10^{-32} \text{ cm}^6 \cdot \text{s}^{-1}$. (The products of reaction (19) are either ground state Kr and F atoms or, possibly, a Kr₃F* molecule and M .) The overall shape of the predicted Kr₂F* fluorescence versus [Kr] curve proved to be quite sensitive to this assumed three-body rate constant. A variation of ~ 15 percent in the rate constant was sufficient to force the predicted curve to fall well outside the scatter of the experimental data. Deactivation of Kr₂F* by electrons in superelastic collisions was estimated and found to be unimportant.

IV. Kr₂F* FLUORESCENCE, QUENCHING, AND ABSORPTION

In this section the results of several fluorescence and absorption measurements will be reported, compared with model predictions, and discussed. Specifically, Kr₂F* spontaneous emission at 300 and 196 K will be compared and the fluorescence efficiency of the Kr₂F* violet continuum, relative to the N₂ ($C \rightarrow B$) UV band, will be given. Secondly, the measurement of the rate constants for quenching of Kr₂F* ($4^2\Gamma$) by F₂ at 196 and 300 K will be described. Finally, the results of Kr₂F* gain/absorption studies at 358 nm will be reported and evaluated.

A. Kr₂F* Spontaneous Emission and Fluorescence Efficiency

Several experiments were conducted to optimize the Kr₂F* fluorescence at 196 and 300 K. For these experiments, the diverter switch on the electron-beam generator was adjusted so that the excitation pulse was of 12–14 ns duration. Also, for the low temperature studies, the e -beam was not fired until at least 5 min after the Ne/Kr/F₂ gas mixture was admitted to its cell (see Fig. 2) to allow the gas temperature to equilibrate with that of the cell walls. Longer delays were found to have a negligible effect on the spontaneous emission signal. In observing the axial Kr₂F* emission with a photodiode, the 410 nm band was isolated from background KrF* and Ne* spontaneous emission with a blue bandpass filter ($T_{\text{max}} = 63$ percent at $\lambda_0 = 390 \text{ nm}$, $\Delta\lambda = 88 \text{ nm}$).

Fig. 4 shows the dependence of the peak Kr₂F* fluorescence on Kr density in Ne/Kr/F₂ gas mixtures at 196 and 300 K. Similar results were obtained by plotting the time-integrated

Kr_2F^* spontaneous emission versus $[\text{Kr}]$. The solid line in Fig. 4 is simply a smooth curve drawn through the data.

Maximum emission was observed when the sum of the neon and krypton pressures was kept constant at 4000 torr and the fluorine partial pressure was 3 torr. For Kr densities up to $5 \cdot 10^{19} \text{ cm}^{-3}$, the peak and time-integrated fluorescence of Kr_2F^* vary negligibly between 196 and 300 K. Since the various gas densities are ~ 50 percent higher for the 196 K data, plotting the peak fluorescence versus Kr pressure would show the peak spontaneous emission at a given Kr pressure to be higher than room temperature. The predictions of the computer code, which were normalized to the data at $[\text{Kr}] = 1.6 \cdot 10^{19} \text{ cm}^{-3}$, are also shown in Fig. 4 for $T = 300 \text{ K}$ and krypton pressures ranging from 100 to 1500 torr. As was mentioned in Section III, the good fit between the code and experiment was obtained by adjusting only one rate constant, that for process (19). Note that the Kr_2F^* emission increases slowly for Kr densities in excess of 10^{19} cm^{-3} .

The fluorescence efficiency of Kr_2F^* , relative to the N_2 ($C \rightarrow B$) band, was determined by filling the e -beam fluorescence cell with either 3800 torr Ne/200 torr Kr/3 torr F_2 ($T = 196 \text{ K}$) or 3000 torr Ar/150 torr N_2 ($T = 300 \text{ K}$) gas mixtures, exciting the gases with the electron beam and viewing the resulting emissions with a photodiode. Since the same cell was used for both gas mixtures and the photodiode's position was fixed, the only corrections to the integrated fluorescence that were required were due to 1) the relative electron energy absorbed by the two different gas mixtures and 2) the spectral characteristics of the photodiode and blue bandpass filter. The e -beam energy deposited in the gas was estimated using the NRL TEP code described previously [26], [45]. Using this approach, the fluorescence efficiency, η (\equiv integrated fluorescence normalized to the deposited electron-beam energy), for the Kr_2F^* continuum was found to be 2.8 times that for the N_2 ($C \rightarrow B$) band [46]. Also, $\eta_{\text{Kr}_2\text{F}^*}$ did not change when p_{Kr} was increased (at 196 K) from 200 to 500 torr, suggesting that the rise in Kr_2F^* fluorescence (Fig. 4) over this pressure range is primarily due to increased e -beam deposition in the gas mixture.

B. Quenching of Kr_2F^* by F_2

For all of the gas mixtures studied, the time decay of the Kr_2F^* fluorescence (observed 50–100 ns after the termination of the pumping pulse) was found to be described by a single exponential over several time constants. Fig. 5 shows the linear variation of the exponential decay frequency τ^{-1} with $[\text{F}_2]$ for Ne, Kr, and F_2 gas mixtures where the partial pressures of Ne and Kr are fixed. The departure of both the 196 and 300 K data from linearity for $[\text{F}_2] \geq 1.5 \cdot 10^{17} \text{ cm}^{-3}$ presumably occurs since, for these fluorine densities, the fluorescence decay rate is becoming comparable to the three-body formation rate for Kr_2F^* which is $k_f[\text{Kr}]^2 \sim 6\text{--}9 \cdot 10^7 \text{ s}^{-1}$ at 196 K [15].

Also shown in Fig. 5 is the prediction of the computer model for the dependence of the Kr_2F^* population decay rate on $[\text{F}_2]$ for $T = 300 \text{ K}$. Although the Kr_2F^* fluorescence decay is likely to be influenced by several kinetic processes, if F_2 quenching is assumed to be dominant, then the rate constants

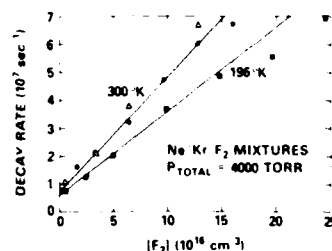


Fig. 5. Dependence of the Kr_2F^* fluorescence exponential decay constant τ^{-1} on $[\text{F}_2]$ for $T = 196$ and 300 K . The solid lines indicate the least squares fitting of the data points for $[\text{F}_2] \leq 1.5 \cdot 10^{17} \text{ cm}^{-3}$ (see text). Again, the open triangles represent the predictions of the computer kinetics code for $T = 300 \text{ K}$.

for quenching of Kr_2F^* by F_2 at 196 and 300 K can be determined. The solid lines shown in Fig. 5 represent the least squares fit of the data (for $\text{F}_2 \lesssim 1.5 \cdot 10^{16} \text{ cm}^{-3}$) to the equation

$$\tau^{-1} = \left\{ \tau_r^{-1} + \sum_i k_i [Q_i] + \sum_j k'_j [Q_j]^2 \right\} + k_{\text{F}_2} [\text{F}_2] \quad (20)$$

where τ^{-1} is the exponential decay rate of the Kr_2F^* fluorescence, τ_r is the Kr_2F^* spontaneous radiative lifetime, $[]$ represents particle densities, k_{F_2} is the two-body Kr_2F^* quenching rate constant for F_2 , and the k_i and k'_j are the two- or three-body rate constants, respectively, for quenching of Kr_2F^* by the background gases Q (neon or krypton). Since p_{Kr} and p_{Ne} are constant in Fig. 5 and only the fluorine pressure is varied, then the term in brackets in (20) is a constant. Also, the slopes of the least squares lines in Fig. 5 yield the rate constants for quenching of Kr_2F^* by F_2 as $(4.1 \pm 0.5) \cdot 10^{-10} \text{ cm}^3 \cdot \text{s}^{-1}$ (300 K) and $3.0 \pm 0.5 \cdot 10^{-10} \text{ cm}^3 \cdot \text{s}^{-1}$ (196 K). The least squares line for the computer generated predictions in Fig. 5 has a slope of $4.4 \cdot 10^{-10} \text{ cm}^3 \cdot \text{s}^{-1}$ which is within 10 percent of the experimentally observed value.

The room temperature rate constant determined here is in excellent agreement with the $(4.3 \pm 0.4) \cdot 10^{-10} \text{ cm}^3 \cdot \text{s}^{-1}$ value reported by Quigley and Hughes [13]. Also, cooling of Ne, Kr, and F_2 gas mixtures apparently results in slower quenching of the Kr_2F^* exciplex by F_2 .

C. Absorption at 358 nm

The superimposed spontaneous emission spectra of Kr_2F^* and the $C \rightarrow B$ band of N_2 are shown in Fig. 6(a) where the various N_2 ($C \rightarrow B$) vibrational transitions are denoted by (v', v'') . The peak of the Kr_2F^* continuum lies at $\lambda \sim 410 \text{ nm}$ and the bandwidth is $\Delta\lambda \sim 43 \text{ nm}$. The spectra were recorded with 3000 torr Ar/150 torr N_2 (at 300 K) in the long (9 cm) cell section (see Fig. 2) and with 3500 torr Ne/500 torr Kr/3 torr F_2 (196 K) in the shorter section. Also, the arrow shown in Fig. 6(a) indicates the 441.6 nm wavelength at which HOHM previously reported absorption [12].

Since the (0, 3) transition of the N_2 ($C \rightarrow B$) band roughly coincides in wavelength with the peak of the Kr_2F^* fluorescence, several attempts were made to achieve lasing on this line using the double compartment e -beam cell of Fig. 2. This effort was unsuccessful and although stimulated emission at

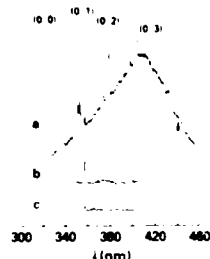


Fig. 6. Densitometer tracings of the Kr₂F* and N₂ (C → B) spectra observed in these experiments. (a) Spontaneous emission from 3000 torr Ar and 150 torr N₂ in the long *c*-beam cell and 3500 torr Ne, 500 torr Kr, and 3 torr F₂ in the other. (b) Ar-N₂ 358 nm laser line strength for 3000 torr Ar and 150 torr N₂ in the long cell and 3950 torr Ne, 50 torr Kr, and 3 torr F₂ in the shorter compartment (the cavity mirrors are described in the text). (c) Ar-N₂ laser output for the same Ar-N₂ gas mixture as (b) but with 3800 torr Ne, 200 torr Kr and 3 torr F₂ in the second compartment. Calibration of the spectra was accomplished using a Hg discharge lamp. The spectrograph resolution for (a), (b), and (c) was ~0.3 nm and all of the Kr₂F* spectra were recorded with the Ne/Kr/F₂ section of the *c*-beam cell at 196 K. The vertical axis for all three traces is linear in optical density.

380.5 nm [(0, 2) transition] could be obtained by filling both compartments with an Ar-N₂ mixture, only on the (0, 1) line at 358 nm could lasing be reliably obtained using only the longer section of the cell.

Fig. 6(b) is a densitometer tracing of the Ar-N₂ 358 nm laser line obtained by placing dielectric mirrors (described in Section II) around the two compartment cell. In this case, the long section contained a 3000 torr Ar, 150 torr N₂ mixture while the shorter compartment held a 3950 torr Ne, 50 torr Kr, and 3 torr F₂ mixture at 196 K. Increasing the partial pressure of krypton in the Ne/Kr/F₂ mixture to 200 torr seriously degraded, rather than enhanced, the Ar-N₂ laser output as shown in Fig. 6(c). In taking the data of Fig. 6, dry ice was packed *only* around the Kr₂F* cell, since the output power of the Ar-N₂ laser is known [48] to decrease dramatically at low temperatures.

Using the calibration procedure outlined in Section II-C, the magnitude of the absorption at 358 nm was measured for various Ne, Kr, and F₂ gas mixtures. (The absorption was measured by normalizing the Ar-N₂ output energy obtained with the desired Ne/Kr/F₂ mixture to that obtained with the Kr₂F* cell evacuated. Fig. 3 was then invoked.) This absorption was found to vary only slightly for Ne/F₂ gas mixtures but increased dramatically when Kr was added. Fig. 7 shows the dependence of the absorption on the partial pressure of krypton where the sum of the Ne and Kr pressures was kept constant at 4000 torr. The solid line in the figure is the linear least squares fit to the data points and obeys the relationship: net loss (percent · cm⁻¹) = 0.83 + 7.36 · 10⁻³ · *p*_{Kr}, where *p*_{Kr} is expressed in torr. Error bars are also shown for data points at each end of the graph to indicate the estimated error per data point, which is largely due to uncertainty of the slope of the calibration line in Fig. 3. Generally, the error per data point gradually increased with the loss.

One drawback of the absorption technique used here (as compared to using, say, an external dye laser probe) is that the gas medium under study can be probed only during the Ar-N₂

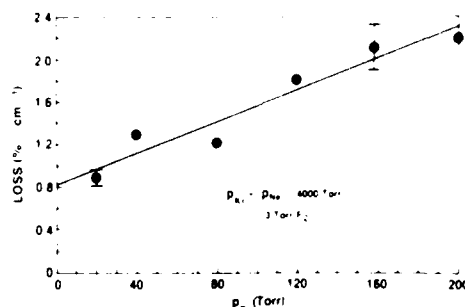


Fig. 7. The linear variation of the absorption of *e*-beam excited Ne, Kr, and F₂ mixtures (at 358 nm) with Kr pressure. The sum of the Kr and Ne pressures was held constant at 4000 torr and all the measurements were conducted at 196 K. The solid line is the linear least squares fit of the data points and its zero pressure intercept is 0.83 percent · cm⁻¹. The absorption was determined by normalizing the laser energy output obtained with a certain Ne/Kr/F₂ mixture to that obtained with the cell evacuated. The two error bars shown are representative of all of the data taken. Generally, due to the uncertainty in the calibration curve of Fig. 3, the estimated error in the data increased with the Kr pressure (i.e., higher loss).

laser pulse. For these experiments, although the *c*-beam pulse was approximately rectangular with a full width of 50 ns, Ar-N₂ lasing occurred only during the last ~10 ns of the pump pulse. This was due to the near threshold operation of the laser which, in turn, was dictated by the short (~9 cm) gain length of the Ar-N₂ laser. As a result, the absorption measurements deal only with the last 10 ns of the pump pulse. Also, the data given (Fig. 7) have been time integrated over that 10 ns interval. This presents no problems because the population densities of the excited species of interest (Kr₂F*, Kr₂F*, etc.) were not expected (based on fluorescence waveforms and computer predictions) to vary appreciably during the 10 ns interval. Both of these limitations, probe pulse length and time resolution, may be rectified by using an Ar-N₂ laser cell with a longer gain length.

D. Discussion

Since the absorption shown in Fig. 7 is roughly linear with the Kr pressure, then excited species whose population densities vary linearly with *p*_{Kr} are potential absorbers. Computer code predictions of the densities of the KrF*, Kr₂F*, Kr₂F*, and Kr₂F* molecules for 0 ≤ *p*_{Kr} ≤ 200 torr are shown in Fig. 8. Although seven other excited species were also studied, the four shown in the figure were expected to be most likely responsible for the 358 nm absorption. Also, the population densities shown in Fig. 8 are those existing 45 ns after the initiation of the *e*-beam current pulse, since the Kr dependence was found to change only slightly with time for 40 ≤ *t* ≤ 50 ns (*t* = 0 represents the beginning of the *e*-beam pulse). Of the species examined by the model, only Kr₂F* and Kr₂F* exhibited a linear dependence on Kr pressure.

Assuming both Kr₂F* and Kr₂F* absorb at 358 nm, the photoabsorption cross section of Kr₂F* can then be estimated. The absorption cross section of Kr₂F* in the visible and near UV has been extensively studied, both theoretically [16], [49] and experimentally [50]–[54]. Wadt and co-workers [16], [55] have calculated the Kr₂F* absorption cross section at 358 nm

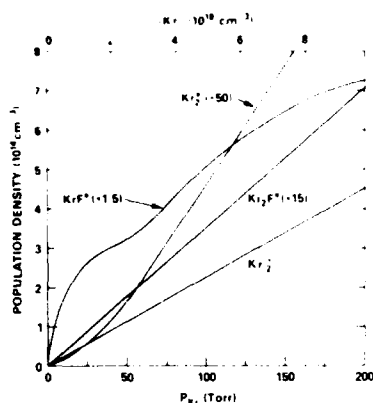


Fig. 8. Computer predictions of the krypton pressure dependence of the population density of various molecules in electron-beam excited Ne, Kr, and F_2 gas mixtures. While each molecule shown is a potential absorber at 358 nm, only the Kr_2^+ and Kr_2F^* populations grow linearly with p_{Kr} over the range 0–200 torr. The scale factor in parentheses for the various molecules indicates the factor by which the ordinate must be multiplied to obtain the correct particle density. The populations shown are those existing 45 ns after the initiation of the e-beam current pulse (although the Kr pressure dependence changes only slightly as a function of time). The calculations were performed for $T = 196$ K.

and 200 K to be $26.2 \cdot 10^{-18} \text{ cm}^2$, which is in excellent agreement with Lee and Smith's value [52] of $(24.8 \pm 1.9) \cdot 10^{-18} \text{ cm}^2$ (measured at 357 and 351 nm) and Vanderhoff's cross section [50] of $23.8 \cdot 10^{-18} \text{ cm}^2$ which was also measured for photon energies of ~ 3.5 eV. However, both of the experimental values were measured at or near room temperature and so the theoretical cross section was incorporated into the calculations to follow.

The absorption data shown in Fig. 7 represent only the net absorption of the Ne, Kr, and F_2 gas mixtures and do not account for the gain of the Kr_2F^* band presumed to be present at 358 nm. Assuming $\tau_{Kr_2F^*}$ to be between 133 and 181 ns and taking $\Delta\lambda$ to be in the range of 40–60 nm, then $\sigma_{se} = (5.1 \pm 1.6) \cdot 10^{-18} \text{ cm}^2$ for the 410 nm band. Therefore, the total absorption suffered by the Ar- N_2 probe laser in traversing the Ne/Kr/ F_2 cell is

$$\alpha_{\text{total}} (\text{cm}^{-1}) = |\text{Gain}| + |\text{Measured Loss}| = \sigma_{se} [Kr_2F^*] + 8.3 \cdot 10^{-3} + 7.4 \cdot 10^{-5} p_{Kr} \quad (21)$$

where p_{Kr} is again expressed in torr. Absorption due to the excited Ne- F_2 background gases, which is the second term ($p_{Kr} = 0$ intercept of Fig. 7) on the right-hand side of (21), will be discussed later. Considering only Kr_2^+ and Kr_2F^* absorption for the moment, for a given Kr pressure,

$$\text{Measured Loss} = Kr_2F^* \text{ and } Kr_2^+ \text{ Loss} - Kr_2F^* \text{ Gain} \quad (22)$$

From Fig. 8, $[Kr_2F^*] \approx 5.3 \cdot 10^{13} \text{ cm}^{-3} \cdot (\text{torr Kr})^{-1}$ and $[Kr_2^+] \approx 2.2 \cdot 10^{12} \text{ cm}^{-3} \cdot (\text{torr Kr})^{-1}$ for p_{Ne} and p_{F_2} approximately fixed. Therefore, $\sigma_{se} [Kr_2F^*] = 2.7 \cdot 10^{-2}$ percent/torr Kr and $\sigma_{Kr_2^+} [Kr_2^+] = 5.8 \cdot 10^{-3}$ percent/torr Kr. Also, recall that the net loss due to Kr-containing excited species (solid line of Fig. 7) is given by $7.4 \cdot 10^{-3}$ percent/torr Kr. Despite its large photoabsorption cross section, then, Kr_2^+ is

not the major source of the observed loss, accounting for only ~ 17 percent of the total absorption ($3.4 \cdot 10^{-2}$ percent/torr Kr) due to krypton-containing excited molecules in 3800 torr Ne $p_{Kr} = 3$ torr F_2 gas mixtures. Now, if Kr_2^+ is assumed to be the only absorber responsible for the observed loss, then the Kr_2^+ photoabsorption cross section is calculated to be $1.6 \cdot 10^{-16} \text{ cm}^2$ which is considerably larger than the experimentally measured cross sections mentioned above.

The remaining absorption ($2.9 \cdot 10^{-2}$ percent/torr Kr) divided by $[Kr_2F^*]$ gives the photoabsorption cross section of Kr_2F^* at 200 K as $5.4 \cdot 10^{-18} \text{ cm}^2$ which is approximately a factor of five lower than that for Kr_2^+ at the same wavelength and temperature. (Actually, $5.4 \cdot 10^{-18} \text{ cm}^2$ must be viewed as an upper limit for $\sigma_{Kr_2F^*}$ since the gain of the Kr_2F^* band at 358 nm will probably be lower than the band's peak value.)

The low Kr_2F^* photoabsorption cross section inferred from these experiments is contrary to theoretical predictions [6] which suggest that $\sigma_{Kr_2^+} \approx \sigma_{Kr_2F^*}$. This prediction resulted from the weak perturbation of Kr_2^+ by F^- that has been calculated for Kr_2F^* ($Kr_2^+F^-$). Although the computed Kr_2F^* and Kr_2^+ densities used earlier to calculate $\sigma_{Kr_2F^*}$ are approximate, they are nonetheless expected to be accurate to within a factor of two. Consequently, at 358 nm, $\sigma_{Kr_2F^*}/\sigma_{Kr_2^+}$ appears to be significantly less than 80 percent.

Hunter *et al.* [12] were able to eliminate Kr_2F^* as a possible absorber at 441.6 nm based on the temporal behavior of the absorption. The wavelength dependence of the Kr_2F^* absorption cross section [6] also suggests that this triatomic molecule may be an insignificant absorber for $\lambda \geq 400$ nm. However, the $1.5 \cdot 10^{-3} \text{ cm}^{-1}$ absorption reported in [12] for Ar, Kr, and F_2 gas mixtures ($p_{\text{total}} \approx 1600$ torr) is consistent with Ar_2^+ or Kr_2^+ absorption.

As mentioned previously, the zero Kr pressure intercept of the solid line in Fig. 7 ($0.83 \text{ percent} \cdot \text{cm}^{-1}$) is the 358 nm absorption due to excited 4000 torr Ne, 3 torr F_2 gas mixtures. Both Ne_2^+ and F^- are possible absorbers at this wavelength [56] (absorption by ground state F_2 molecules is negligible), but the low F^- densities predicted by the kinetics code for these mixtures suggest that this negative ion contributes negligibly to the observed absorption. (Also, Mandl's results [57] show that the F^- photodetachment cross section is rapidly falling for $\lambda > 350$ nm.) Therefore, taking $[Ne_2^+]$ to be $1 \cdot 10^{16} \text{ cm}^{-3}$ (code prediction for the time-average Ne_2^+ density from $t = 40$ –50 ns), then $\sigma_{Ne_2^+} = 8.1 \cdot 10^{-19} \text{ cm}^2$. This compares with Lee and Smith's experimental value [52] of $19.3 \cdot 10^{-19} \text{ cm}^2$ ($T \sim 300$ K) and Wadt, Cartwright, and Cohen's [16] theoretical prediction of $5 \cdot 10^{-19} \text{ cm}^2$ at 200 K. Table III summarizes the photoabsorption cross sections that are significant at 358 nm.

The strong nonlinearity of the Kr_2^+ population for $0 \leq p_{Kr} \leq 50$ torr (shown in Fig. 8) suggests that the Kr_2^+ excimer contributes insignificantly to the 358 nm absorption observed in these experiments. Although it appears that studies of the electronic structure of Kr_2^+ have not yet been published, detailed Xe_2^+ potential curve calculations have been performed recently by Ermiler and co-workers [58]. Their results indicate that Xe_2^+ absorption [from low-lying ungerade states associated with the $Xe^* (^3P_2, ^3P_1) + Xe (^1S)$ asymptote to

TABLE III
SUMMARY OF THE ABSORPTION CROSS SECTIONS OF Kr₂F* AND Ne₂F*
AT $\lambda \approx 358$ nm

Species	σ , cm ²	Reference
Kr ₂ F*	1.4×10^{-18}	This work
Ne ₂ F*	5.4×10^{-18}	This work
Ne ₂ F*	8.1×10^{-19}	Woods, Cartwright and Cohen ^a
Ne ₂ F*	1.1×10^{-17}	Lee and Smith ^b
Ne ₂ F*	1.1×10^{-17}	Woods, Cartwright and Cohen ^a
Ne ₂ F*	1.1×10^{-17}	Lee and Smith ^b
Ne ₂ F*	1.1×10^{-17}	Vanderhoff ^c

^a Values where noted, all of the cross-sections given were computed or measured at $T = 196^\circ\text{K}$.

^b Effective kinetic temperature = 166°K .

^c Effective kinetic temperature = 300°K .

^d Refs. 16 and 54.

^e Ref. 52.

^f Ref. 50.

gerade levels connected to the Xe* (³P₀, ¹P₁) + Xe(¹S) limit) should be similar to that for the Xe₂⁺ ion. A similar situation may hold for Kr₂⁺ and Kr₂⁺.

If Kr₂⁺ is indeed absorbing strongly in the 350 nm range, then an upper limit for $\sigma_{\text{Kr}_2^+}$ may also be calculated from the data already presented. The [Kr₂⁺] curve shown in Fig. 8 can be roughly approximated by the line [Kr₂⁺] = $2.6 \cdot 10^{14}$ cm⁻³ (torr Kr)⁻¹. After subtracting the contribution of Kr₂⁺ from the overall absorption, the remaining absorption for ~ 4000 torr Ne/p_{Kr}/3 torr F₂ gas mixtures is $2.9 \cdot 10^{-2}$ percent/torr Kr. Dividing this value by the Kr₂⁺ slope above yields ($\sigma_{\text{Kr}_2^+}$)_{max} $\sim 1.1 \cdot 10^{-18}$ cm².

V. CONCLUSIONS

A simple laser intracavity technique has been used to probe for gain on the violet continuum of Kr₂F*. Although intense fluorescence from Kr₂F* and reduced quenching of the triatomic molecule by F₂ occurs at low temperature (e.g., 196°K), strong absorption has been observed at 358 nm. This absorption, which appears to be due to Kr₂F*, Kr₂⁺, and Ne₂⁺, suggests that it is unlikely that an efficient Kr₂F* laser is attainable in e-beam excited Ne, Kr, and F₂ gas mixtures, even for wavelengths closer to the 410 nm band center.

By calibrating the absorption system with F₂ and Cl₂, the Ne₂⁺ and Kr₂F* absorption cross sections at 358 nm and 196 K have been estimated to be $8.1 \cdot 10^{-19}$ cm² and $5.4 \cdot 10^{-18}$ cm², respectively. The Kr₂F* photoabsorption cross section is ~ 20 percent of that for Kr₂⁺ at the same wavelength ($2.6 \cdot 10^{-17}$ cm², 300 K).

Potentially extremely sensitive and not requiring an external dye laser, the intracavity technique described in this paper is applicable to a wide range of potential laser systems. The only criterion that must be satisfied is that a known e-beam excited laser line must lie in the wavelength range of interest for the probed gas mixture.

Finally, rate constants for the quenching of Kr₂F* by F₂ have been determined for $T = 196$ and 300 K and the room

temperature result is in excellent agreement with a previously reported value.

ACKNOWLEDGMENT

The authors are grateful to D. Fipp for excellent technical advice and assistance during these experiments. Our thanks are also extended to Drs. R. W. Waynant, R. Burnham, J. Reintjes, and W. R. Wadt for many excellent suggestions and discussions.

REFERENCES

- [1] D. C. Lorents, R. M. Hill, D. L. Huestis, M. V. McCusker, and H. H. Nakano, "Spectroscopy and kinetics of the 248 and 414 nm bands from electron beam pumped argon-krypton-fluorine mixtures," presented at the Third Summer Colloquium on Electron Transition Lasers, Snowmass-in-Aspen, CO, Sept. 1976; published in *Electronic Transition Lasers II*, L. F. Wilson, S. N. Suchard, and J. I. Steinfeld, Eds. Cambridge, MA: MIT Press, pp. 30-34, 1977.
- [2] D. C. Lorents, D. L. Huestis, M. V. McCusker, H. H. Nakano, and R. M. Hill, "Optical emissions of triatomic rare gas halides," *J. Chem. Phys.*, vol. 68, pp. 4657-4661, 1978.
- [3] N. G. Basov, V. A. Danilychev, V. A. Dolgikh, O. M. Kerimov, V. S. Lebedev, and A. G. Molchanov, "New excimer emission bands of noble-gas halides," *Pis'ma Zh. Eksp. Teor. Fiz.*, vol. 26, p. 20, 1977; also in *JETP Lett.*, vol. 26, pp. 16-20, 1977.
- [4] J. A. Mangano, J. H. Jacob, M. Rokni, and A. Hawryluk, "Three-body quenching of KrF* by Ar and broad-band emission at 415 nm," *Appl. Phys. Lett.*, vol. 31, pp. 26-28, 1977.
- [5] M. Krauss, "The electronic structure of rare gas halide excimers," *J. Chem. Phys.*, vol. 67, pp. 1712-1719, 1977; see also [4].
- [6] W. R. Wadt and P. J. Hay, "Electronic states of Ar₂F* and Kr₂F*," *J. Chem. Phys.*, vol. 68, pp. 3850-3863, 1978.
- [7] D. L. Huestis and N. E. Schlatter, "Diatomics-in-molecules potential surfaces for the triatomic rare gas halides: Rg₂X," *J. Chem. Phys.*, vol. 69, pp. 3100-3107, 1978.
- [8] W. R. Wadt and P. J. Hay, "The low-lying electronic states of Ar₂F*," *Appl. Phys. Lett.*, vol. 30, pp. 573-575, 1977.
- [9] H. H. Michels, R. H. Hobbs, and L. A. Wright, "The electronic structure of ArF and Ar₂F*," *Chem. Phys. Lett.*, vol. 48, pp. 158-161, 1977.
- [10] C. F. Bender and H. F. Schaeffer III, "Ionic excited states of Ne₂F*," *Chem. Phys. Lett.*, vol. 53, pp. 27-30, 1978.
- [11] M. Rokni, J. H. Jacob, and J. A. Mangano, "Dominant formation and quenching processes in e-beam pumped ArF* and KrF* lasers," *Phys. Rev. A*, vol. 16, pp. 2216-2224, 1977.
- [12] R. O. Hunter, J. Oldenettel, C. Howton, and M. V. McCusker, "Gain measurements at 4416 Å on ArXeF* and Kr₂F*," *J. Appl. Phys.*, vol. 49, pp. 549-552, 1978.
- [13] G. P. Quigley and W. M. Hughes, "Lifetime and quenching rate constants for Kr₂F* and Kr₂⁺," *Appl. Phys. Lett.*, vol. 32, pp. 649-651, 1978.
- [14] B. Fointaine and B. Forestier, "Ultraviolet laser emissions and fluorescence enhancements in an e-beam excited low temperature and high density supersonic flow," presented at the 31st Ann. Gaseous Electron. Conf., Buffalo, NY, 1978.
- [15] V. H. Shui, "Temperature dependence of recombination rate constants for KrF* + R + R → RKrF* + R (R = Ar, Kr)," *Appl. Phys. Lett.*, vol. 34, pp. 203, 204, 1979.
- [16] W. R. Wadt, D. C. Cartwright, and J. S. Cohen, "Theoretical absorption spectra for Ne₂⁺, Ar₂⁺, Kr₂⁺ and Xe₂⁺ in the near ultraviolet," *Appl. Phys. Lett.*, vol. 31, pp. 672-674, 1977.
- [17] J. G. Eden and S. K. Searles, "Observation of stimulated emission in KrCl," *Appl. Phys. Lett.*, vol. 29, pp. 350-352, 1976.
- [18] G. Marowsky, R. Cordray, F. K. Tittel, W. L. Wilson, and C. B. Collins, "Intense laser emission from electron-beam-pumped ternary mixtures of Ar, N₂ and POPOP vapor," *Appl. Phys. Lett.*, vol. 33, pp. 59-61, 1978.
- [19] R. K. Steunenberg and R. C. Vogel, "The absorption spectrum of fluorine," *J. Amer. Chem. Soc.*, vol. 78, pp. 901, 902, 1956.
- [20] D. J. Seery and D. Britton, "The continuous absorption spectra of chlorine, bromine, bromine chloride, iodine chloride and iodine bromide," *J. Phys. Chem.*, vol. 68, pp. 2263-2266, 1964.
- [21] T. H. Johnson, L. J. Palumbo, and A. M. Hunter, "Kinetics simu-

- lation of high power gas lasers," *IEEE J. Quantum Electron.*, vol. QE-15, pp. 289-301, May 1979.
- [22] T. G. Finn, L. J. Palumbo, and L. F. Champagne, "A kinetics scheme for the XeF laser," *Appl. Phys. Lett.*, vol. 33, pp. 148-151, 1978.
 - [23] L. J. Palumbo, T. G. Finn, and L. F. Champagne, "Energy flow kinetics in a xenon-chloride laser," presented at the 31st Gaseous Electron. Conf., Buffalo, NY, Oct. 17-20, 1978, Paper BA-4.
 - [24] C. E. Treanor, "A method for the numerical integration of coupled first-order differential equations with greatly different time constants," *Math. Comput.*, vol. 20, pp. 39-45, 1966; also in "A method for the numerical integration of coupled first-order differential equations with greatly different time constants," Cornell Aeronaut. Lab., Inc., Buffalo, NY, CAL Rep. AG-1729-A-4, 1964.
 - [25] M. J. Berger and S. M. Seltzer, "Tables of energy losses and ranges of electrons and positrons," Nat. Aeronaut. and Space Administration, Washington, DC, Rep. NASA SP-3012, 1964.
 - [26] DARPA-NRL Laser Program, Semiann. Tech. Rep., pp. 111-129, Apr. 1978.
 - [27] D. B. Brown and R. E. Ogilvie, "An electron transport model for the prediction of x-ray production and electron backscattering in electron microanalysis," *J. Appl. Phys.*, vol. 37, pp. 4429-4433, 1966.
 - [28] O. J. Orient, "Mobility of mass-identified ions in neon and reaction rate coefficient for $\text{Ne}^+ + 2\text{Ne} \rightarrow \text{Ne}_2^+ + \text{Ne}$," *Chem. Phys. Lett.*, vol. 23, pp. 579-581, 1973.
 - [29] C. L. Chen, "Atomic processes in helium-krypton and helium-xenon mixtures," *Phys. Rev.*, vol. 131, pp. 2550-2555, 1963.
 - [30] L. Frommhold, M. A. Biondi, and F. J. Mehr, "Electron temperature dependence of electron-ion recombination in neon," *Phys. Rev.*, vol. 165, pp. 44-52, 1968; also in J. Philbrick, F. J. Mehr, and M. A. Biondi, "Electron temperature dependence of recombination of Ne_2^+ ions with electrons," *Phys. Rev.*, vol. 181, pp. 271-274, 1969.
 - [31] Y.-J. Shiu and M. A. Biondi, "Dissociative recombination in krypton: Dependence of the total rate coefficient and excited-state production on electron temperature," *Phys. Rev. A*, vol. 16, pp. 1817-1820, 1977.
 - [32] D. L. Huestis, R. M. Hill, H. H. Nakano, and D. C. Lorents, "Quenching of Ne^* , F^* , and F_2^+ in $\text{Ne}/\text{Xe}/\text{NF}_3$ and $\text{Ne}/\text{Xe}/\text{F}_2$ mixtures," *J. Chem. Phys.*, vol. 69, pp. 5133-5139, 1978.
 - [33] R. T. Ku, J. T. Verderyn, B. E. Cherrington, and J. G. Eden, "Decay of krypton Is_2 and Is_3 excited species in the late afterglow," *Phys. Rev. A*, vol. 8, pp. 3123-3130, 1973 and references cited therein.
 - [34] R. H. Neynaber and G. D. Magnuson, "Penning and associative ionization in the metastable neon-krypton system," *Phys. Rev. A*, vol. 14, pp. 961-964, 1976.
 - [35] J. M. Brom, Jr., J. H. Kolts, and D. W. Setser, "Quenching rate constants for $\text{Ne} (^3\text{P}_2)$ metastable atoms at room temperature," *Chem. Phys. Lett.*, vol. 55, pp. 44-48, 1978.
 - [36] H. L. Kramer, J. A. Herce, and E. E. Muschlitz, Jr., "Formation and collisional dissociation of heteronuclear rare-gas associative ions," *J. Chem. Phys.*, vol. 56, pp. 4166-4170, 1972.
 - [37] R. J. Hall, "Dissociative attachment and vibrational excitation of F_2 by slow electrons," *J. Chem. Phys.*, vol. 68, pp. 1803-1807, 1978.
 - [38] a) L. G. Piper, D. W. Setser, and M. A. A. Clyne, "Electronic energy transfer from metastable argon atoms to krypton atoms," *J. Chem. Phys.*, vol. 63, pp. 5018-5028, 1975. b) J. E. Velazco, J. H. Kolts, and D. W. Setser, "Quenching rate constants for metastable argon, krypton, and xenon atoms by fluorine containing molecules and branching ratios for XeF^+ and KrF^+ formation," *J. Chem. Phys.*, vol. 65, pp. 3468-3480, 1976.
 - [39] M. R. Flannery and T. P. Yang, "Ionic recombination of rare-gas atomic ions X^+ with F^- in a dense-gas X ," *Appl. Phys. Lett.*, vol. 32, pp. 327-329, 1978.
 - [40] "Ionic recombination of rare-gas molecular ions X_2^+ with F^- in a dense gas X ," *Appl. Phys. Lett.*, vol. 32, pp. 356-357, 1978.
 - [41] D. L. Huestis, R. M. Hill, D. J. Eckstrom, M. V. McCusker, D. C. Lorents, H. H. Nakano, B. F. Perry, J. A. Margevicius, and N. F. Schlotter, "New electronic-transition laser systems," Stanford Res. Inst. Int., Menlo Park, CA, SRI Rep. MP 78-07, May 1978.
 - [42] M. R. Flannery and T. P. Yang, "Ionic recombination of Kr^+ and Kr_2^+ with F^- in dense buffer rare gases," *Appl. Phys. Lett.*, vol. 33, pp. 574-576, 1978.
 - [43] J. G. Eden, R. W. Waynant, S. K. Searles, and R. Burnham, "KrF (B) quenching by He, Ne, and NF_3 ," *J. Appl. Phys.*, vol. 49, pp. 5368-5372, 1978.
 - [44] "New quenching rates applicable to the KrF laser," *Appl. Phys. Lett.*, vol. 32, pp. 733-735, 1978.
 - [45] S. K. Searles and G. A. Hart, "Yields of $\text{N}_2(\text{C})$ from $\text{Ar}^+ + \text{N}_2$ and XeBr^+ from $\text{Xe}^+ + \text{Br}_2$," *Appl. Phys. Lett.*, vol. 28, pp. 384-386, 1976.
 - [46] The fluorescence efficiency for the $\text{N}_2 (\text{C} \rightarrow \text{B})$ band in e-beam pumped $\text{Ar}-\text{N}_2$ gas mixtures has been measured to be 17.6 percent/ P where P is the argon pressure in atmospheres. For the Ar/N_2 mixtures given, $\eta_{\text{Ar}-\text{N}_2} \geq 4.4$ percent; see [41].
 - [47] V. H. Shui, "Calculation of recombination rate constants for $\text{KrF}^+ + \text{R} + \text{R} \rightarrow \text{RKrF}^+ + \text{R}$ ($\text{R} = \text{Ar}, \text{Kr}$)," *Appl. Phys. Lett.*, vol. 31, pp. 50-52, 1977.
 - [48] A. N. Brunin, V. A. Danilychev, V. A. Dolgikh, O. M. Kerimov, and A. N. Lobanov, "Kinetic model of an $\text{Ar} + \text{N}_2$ ultraviolet laser," *Sov. J. Quantum Electron.*, vol. 6, pp. 1275-1279, 1976.
 - [49] W. R. Wadt, "The electronic states of Ar_2^+ , Kr_2^+ , Xe_2^+ . I. Potential curves with and without spin-orbit coupling," *J. Chem. Phys.*, vol. 68, pp. 402-414, 1978.
 - [50] J. A. Vanderhoff, "Photodissociation cross sections for Ar_2^+ , Kr_2^+ , and Xe_2^+ at 3.0 and 3.5 eV," *J. Chem. Phys.*, vol. 68, pp. 3311-3313, 1978.
 - [51] L. C. Lee, G. P. Smith, T. M. Miller, and P. C. Cosby, "Photodissociation cross sections of Ar_2^+ , Kr_2^+ and Xe_2^+ from 6200 to 8600 Å," *Phys. Rev. A*, vol. 17, pp. 2005-2011, 1978.
 - [52] L. C. Lee and G. P. Smith, "Photodissociation cross sections of Ne_2^+ , Ar_2^+ , Kr_2^+ and Xe_2^+ from 3500 to 5400 Å," to be published.
 - [53] T. H. Miller, J. H. Ling, R. P. Saxon, and J. T. Moseley, "Absolute total cross sections for the photodissociation of Ar_2^+ , Kr_2^+ , Xe_2^+ , KrN_2^+ and KrN^+ from 565 to 695 nm," *Phys. Rev. A*, vol. 13, pp. 2171-2177, 1976.
 - [54] R. Abouaf, B. A. Huber, P. C. Cosby, R. P. Saxon, and J. T. Moseley, "Photofragment spectroscopy and potential curves of Kr_2^+ ," *J. Chem. Phys.*, vol. 68, pp. 2406-2410, 1978.
 - [55] W. R. Wadt, private communication.
 - [56] M. Rokni, J. A. Mangano, J. H. Jacob, and J. C. Hsia, "Rare gas fluoride lasers," *IEEE J. Quantum Electron.*, vol. QE-14, pp. 464-481, July 1978.
 - [57] A. Mandl, "Electron photodetachment cross section of the negative ion of fluorine," *Phys. Rev. A*, vol. 3, pp. 251-255, 1971.
 - [58] W. C. Ermler, Y. S. Lee, K. S. Pitzer, and N. W. Winter, "Ab initio effective core potentials including relativistic effects. II. Potential energy curves for Xe_2 , Xe_2^+ and Xe_2^- ," *J. Chem. Phys.*, vol. 69, pp. 976-983, 1978.

A Discharge Pumped Laser on the C→A Transition of XeF

Direct electrical excitation of laser oscillation centered at 490 nm has been obtained on the C→A transition of XeF in mixtures of He, Xe, and NF₃ pumped by a self-sustained discharge. Laser output appears to have been limited by the short time available for the buildup of oscillation in the transient discharge.

A discharge pumped laser on the $C \rightarrow A$ transition of XeF

R. Burnham

Naval Research Laboratory, Washington, D.C. 20375

(Received 1 March 1979; accepted for publication 10 April 1979)

Direct electrical excitation of laser oscillation centered at 490 nm has been obtained on the $C \rightarrow A$ transition of XeF in mixtures of He, Xe, and NF₃ pumped by a self-sustained discharge. Laser output appears to have been limited by the short time available for the buildup of oscillation in the transient discharge.

PACS numbers: 42.55.Hq, 42.60.By, 52.80. — s

The prospect of obtaining stimulated emission on the $C \rightarrow A$ transition of XeF has tantalized many laser physicists for several years. The large bandwidth (~ 100 nm) and center wavelength at ~ 470 nm offer the prospect of a tunable higher-power gas laser operating over a large region of the visible spectrum. Attempts to obtain oscillation on the $C \rightarrow A$ transition with electron-beam excitation have been frustrated by the existence of transient optical absorption. This absorption, which appears throughout the visible and ultraviolet in e-beam-pumped systems, is thought to be associated with excited rare-gas dimers or dimer ions. Recently, this absorption problem has been circumvented through photolytic pumping of XeF₂ to produce laser oscillation on the XeF $C \rightarrow A$ transition.¹ Another approach to the excitation of the $C \rightarrow A$ laser is direct discharge pumping. Reported here is the first demonstration of an electrically pumped laser on the XeF $C \rightarrow A$ transition. The laser was excited in a self-sustained transverse electric discharge. The results of this demonstration indicate that the power extracted on the $C \rightarrow A$ transition was limited by the short time (~ 75 nsec) available for the buildup of stimulated emission. In addition, strong absorption observed throughout the laser spectral region from atomic lines originating on the first excited states of Xe may further limit the efficiency of operation of the XeF $C \rightarrow A$ laser excited in a discharge-pumped system.

Laser emission centered near 490 nm was obtained over a bandwidth of approximately 30 nm from gas mixtures consisting of He, Xe, and NF₃, excited in a uv-preionized transverse electric discharge.² The discharge had an active length of 50 cm and a cross section of 2×0.5 cm, into which up to 10 J of electrical energy could be deposited in ~ 75 nsec. The optical cavity was formed by two 3-m radius-of-curvature dielectric-coated mirrors with transmission of 0.1% between 450 and 510 nm, mounted within the discharge cavity. The mirrors were also AR coated at 350 nm in order to suppress oscillation on the XeF $B \rightarrow X$ transitions at 351 and 353 nm.

Measurements of the laser output with a calibrated photodiode located 3 m from the discharge showed that the laser energy was of the order of $0.1 \mu\text{J}$ in a pulse of 175-nsec duration. The laser was therefore operating very near threshold. However, the low divergence (~ 1 mrad) and spectral narrowing of the output indicated that laser oscillation had actually been achieved. Stimulated emission was obtained initially from gas mixtures consisting of 0.3% Xe, 0.1% NF₃, and He at a total pressure of 1000 Torr. The output from the laser was subsequently found to increase

with helium pressure up to 2300 Torr (the maximum operating pressure of the laser cell). The optimum concentrations of Xe and NF₃ were found to remain constant at 3 and 1 Torr, respectively, independent of the total gas pressure. At the higher pressures the output coupling of the optical cavity was increased to 5% with an increase in laser output to $3 \mu\text{J}$ in a 125-nsec pulse.

The shape of the $C \rightarrow A$ laser pulse (with the high- Q optical cavity) is shown in Fig. 1. The spike at the beginning of the pulse arises from superfluorescence on the XeF $B \rightarrow X$ transition at 351 nm. This spike marks the peak of the 75-nsec fluorescence pulse from the XeF B and C states. The $C \rightarrow A$ laser pulse may be seen to build up during this spontaneous emission pulse, and then to decay exponentially with a time constant defined by the Q of the optical cavity (~ 75 nsec). This rather long decay time indicates that the optical absorption in the laser medium following the termination of the pumping pulse does not exceed $0.04\% \text{ cm}^{-1}$.

The spectrum of the $C \rightarrow A$ laser is shown in Fig. 2. Laser emission occurs between 450 and 510 nm. Interspersed throughout the emission band are numerous absorption lines. Many of these lines have been assigned to transitions which terminate on the $1s$ (Paschen notation) states of Xe and the $1s\ 2s$ and $1s\ 2p$ states of He. These states in Xe are precursors to the formation of the excited states of XeF and are significantly populated in the discharge. The two absorption lines of shortest wavelength (at 462.4 and 467.1 nm) appear to be responsible for the reduced laser output near 470 nm, and for the apparent shift in the center of the laser spectrum to the red of the fluorescence maximum at about 470 nm. In addition to the rare-gas absorption lines, a number of other lines which have not been identified but which may arise from molecular species also contribute to the reduction of the laser output.

Optical gain on the $C \rightarrow A$ transition was measured under conditions similar to those under which laser oscillation was obtained using a cw argon-ion laser as a probe. These measurements yielded a peak gain coefficient of 0.01 cm^{-1} at

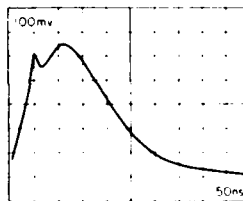


FIG. 1. XeF $C \rightarrow A$ laser pulse shape. The spike at the beginning results from XeF $B \rightarrow X$ superfluorescence which arises near the peak of the spontaneous emission pulse. Sweep speed = 50 nsec/div.

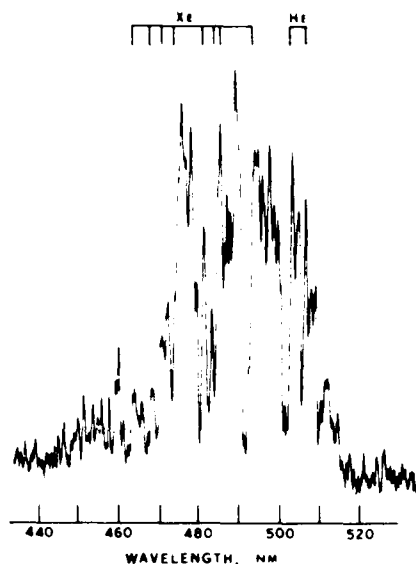


FIG. 2. Spectrum of the XeF $C \rightarrow A$ laser. Absorption lines assigned to atomic transitions in Xe and He are labeled.

476 and 488 nm and about one-half this gain at 515 nm. The integrated gain available for the buildup of oscillation over the 75-nsec optical pulse is given by

$$\alpha_m \Delta \tau = 22.5,$$

where α_m is the peak small-signal gain coefficient. This integrated gain is very close to the recognized threshold gain of 30 required for the buildup of oscillation from spontaneous noise. The observation of weak laser emission is therefore consistent with the measured gain and short time available for laser buildup.

In conjunction with the gain measurements, the spontaneous emission intensity on both the $C \rightarrow A$ and $B \rightarrow X$ transitions was also measured. These intensity measurements were made using the photodiode used to measure the laser output power. Absolute fluorescence intensities were inferred from the known sensitivity of the photodiode and the measured solid angle subtended by the photodiode which viewed the axial emission from the discharge. These measurements yielded a peak fluorescence power density of 5 kW cm^{-2} on the $C \rightarrow A$ transition and roughly five to ten times this power

density on the $B \rightarrow X$ transition. Peak populations of 10^{17} cm^{-3} in both the XeF C and B states were calculated from the fluorescence intensity using the measured radiative lifetimes of the B and C states (15 and 90 nsec, respectively). These calculations suggest that the populations of the B and C states are strongly mixed by electrons in the discharge since the C state has been found to lie roughly 0.1 eV below the B state.⁴ This mixing is not unexpected since measurements indicate peak electron densities of 10^{17} cm^{-3} and maximum electron temperatures of $\sim 10 \text{ eV}$ in the discharge.

The peak small-signal gain on the $C \rightarrow A$ transition may also be calculated from the measured fluorescence. The cross section for stimulated emission at the center of the $C \rightarrow A$ band is found from the measured bandwidth and radiative lifetime to be about $1 \times 10^{-17} \text{ cm}^2$. The small-signal gain ($\sigma_{CA} N_C$) is therefore about 0.01 cm^{-1} , in agreement with the measured gain.

Finally, the measured fluorescence on the $C \rightarrow A$ and $B \rightarrow X$ transitions gives a fluorescence efficiency of about 2%, based upon the electrical energy stored in the laser discharge capacitors. Thus, if this fluorescence power could be extracted in the $C \rightarrow A$ laser pulse, one could expect laser energies of up to 200 mJ. However, if the B and C states are strongly coupled, efficient optical extraction will require an intracavity flux of $\sim 10 \text{ MW cm}^{-2}$. In the laser experiments described above, the maximum intracavity flux reached was only 600 W. Extraction was therefore limited to a small fraction of the available energy. If the length of the discharge pumping pulse can be increased somewhat while maintaining a high pump power density ($\sim 10^8 \text{ W cm}^{-2}$), then efficient optical extraction may be possible. The ultimate efficiency for extraction of the laser energy will depend, in addition, upon the magnitude of nonsaturable optical loss in the laser medium. If this loss can be reduced to a small fraction of the small-signal gain on the $C \rightarrow A$ transition, then efficient operation of the $C \rightarrow A$ laser may be possible in both discharge and optically pumped systems.

⁴W. K. Bischel, H. H. Nakano, D. J. Eckstrom, R. M. Hill, D. L. Huestis, and D. C. Lorents *Appl. Phys. Lett.* (to be published).

⁵R. Burnham and N. Djieu, *Appl. Phys. Lett.* **29**, 707 (1976).

⁶R. W. Waynant and J. G. Eden, *IEEE J. Quantum Electron.* **QE-15**, 61 (1979).

⁷R. M. Hill, P. L. Trevor, D. L. Huestis, and D. C. Lorents, *Appl. Phys. Lett.* **34**, 137 (1979).